Low Thrust Transfers Between Periodic Orbits in the
Earth-Moon Circular Restricted Three-Body Problem

by

Rohan Patel

B.S., Aerospace Engineering, California State Polytechnic University,

Pomona, 2020

A thesis submitted to the

Faculty of the Graduate School of the

University of Colorado in partial fulfillment

of the requirements for the degree of

Master of Science

Department of Aerospace Engineering Sciences

2023

Committee Members:

Dr. Natasha Bosanac, Chair

Dr. Kathryn Davis

Dr. Marcus Holzinger

Patel, Rohan (M.S., Aerospace Engineering Sciences)

Low Thrust Transfers Between Periodic Orbits in the Earth-Moon Circular Restricted Three-Body

    Problem

Thesis directed by Prof. Dr. Natasha Bosanac

With growing interest in cislunar exploration, the importance of trajectory design in this environment has become prevalent. The Circular Restricted Three Body Problem (CR3BP) offers a useful dynamical model to incorporate the gravitational influence from the Earth and Moon in this regime. Several fundamental solutions exist in this model that are beneficial for trajectory design. One type of motion is periodic orbits that are repeating with respect to the motion of the Earth and Moon about the system barycenter. A wide variety of stable and unstable periodic orbits have been identified around equilibrium points and both celestial bodies. Transfers between periodic orbits can help facilitate cislunar exploration objectives for human spaceflight, space domain awareness, and science missions. Thus, this thesis focuses on designing transfers for low thrust spacecraft between periodic orbits in the Earth-Moon CR3BP.

Insights of the dynamics are leveraged along with strategies to form initial guess transfer paths between two periodic orbits. Shooting schemes are employed to produce continuous transfers for each initial guess, and continuation is used compute potentially many transfers of interest. Finally, direct optimization is used to compute locally fuel-optimal transfers. The process of identifying potential initial guess paths, recovering a continuous solution, and ultimately an optimal trajectory is shown to be an effective method to find transfers between periodic orbits. Example cases are demonstrated between subsets of the L_1 and L_2 halo periodic orbit family and a near rectilinear halo orbit (NRHO) to a distant retrograde orbit (DRO) in the Earth-Moon system.

Dedication

I would like to dedicate this thesis to my family, friends, and mentors who have supported me throughout. I am in debt to all of you and can't thank you enough for being there for me every step of the way.

Acknowledgements

I've been very fortunate to be surrounded by encouraging and supportive people throughout my academic career. My parents have unconditionally supported all my educational endeavours and I could not have come this far in the journey of learning without their sacrifice. At Cal Poly Pomona, the guidance and inspiration from Dr. Navid Nakhjiri, Dr. Gregory Lantoine, and Dr. Try Lam have led me to this point. I also have to thank my mentors Dr. Sonia Hernandez and Dr. Jeffrey Stuart for the internship opportunities they've given me at JPL. Their time, help, and exposing me to the world of mission design are the reasons I want to continue learning about trajectory design and to pursue a career in astrodynamics. Thank you Burton and Josh for always being there to bounce ideas off of and to talk nitty-gritty astrodynamics. It's always been a pleasure grabbing beers, playing games, and sharing this passion with you guys. I am appreciative of Dr. Kathryn Davis and Dr. Marcus Holzinger for serving as members on my thesis committee and Dr. Thomas Smith for insightful conversations about initial guess design. And finally, thank you Dr. Natasha Bosanac for being my advisor. Your guidance, patience, and encouragement throughout this process has been second to none. Your passion for teaching the circular restricted three-body problem is the reason I was inspired to pursue this research.

Contents

Chapter

Tables

Table

Figures

Figure

Chapter 1

Introduction

Lunar bound missions began in the same year Sputnik launched the Space Age. The Luna and Pioneer programs trail blazed humanity's presence in cislunar space[34], and since then a myriad of missions have been conducted to better understand the Earth-Moon neighborhood. The Apollo missions marked a cornerstone in lunar exploration, and since then a globally renewed interest has been reignited. NASA and other space agencies in the Artemis accords[1] have joined forces to usher in a new era of space exploration - one which includes an increased presence on and around the Moon. To facilitate this development and make missions more effective and affordable, advancements have been achieved in designing low energy trajectories that exploit the gravitational force of multiple celestial bodies[34].

A common multi-body dynamics model for developing trajectories is the circular restricted three-body model. Solutions from this non-integrable system have been exploited by mission designers to facilitate low propellant cost trajectories compared to the conventional two-body model. Examples of legacy low energy missions include ISEE-3, Genesis, the original ARTEMIS, ACE, WIND, WMAP, and SOHO[47]. Plans for future Artemis missions and the Deep Space Gateway (DSG)[9] include low energy trajectories to and in the vicinity of the Moon. Since the successes of NASA's SERT-1 and Deep Space 1[2, 40], low thrust propulsion has seen technological improvements and interest for space missions. Low thrust propulsion systems, such as gridded-ion and hall effect thrusters, offer considerably higher efficiencies over conventional chemical thrusters, but have significantly lower thrust outputs. By design, these thrusters can operate for months on end[2] and

overtime can accumulate a large amount of ΔV to accommodate trajectory requirements. Examples of deep space missions with low thrust propulsion include Hayabusa[24], Bepi-Colombo[22], Dawn[44], and Psyche[45] and the technology has being applied to Earth-orbiting spacecraft as well. This propulsion type is suitable for all types of spacecraft from cubesats up to spacecraft in excess of 50 metric tons[28].

The benefits of combining low energy and low thrust propulsion for trajectory design can increase spacecraft payload and satisfy complex mission requirements. Science, communications relays, and space domain awareness[53, 10] are examples of missions that can utilize low energy trajectories. Specifically, repeating orbits such as periodic or quasi-periodic orbits are of interest as their motion is bounded within a chaotic system. These solutions exist to varying degrees going from a simplified dynamical model to the full-ephemeris model. Transferring between these orbits is an important aspect in trajectory design as it helps facilitate mission objectives.

1.1   The Restricted Problem

The study of gravitational dynamics between three-bodies has been of interest for hundreds of years dating back to Newton in the Principia. Advancements in the understanding of this problem can be attributed to Euler, Lagrange, Jacobi, Hill, Poincaré, Birkhoff and many others[46]. The three-body problem is inherently a chaotic system meaning analytical solutions are not admitted and there is a considerable sensitivity to the initial guess. However, with simplifying assumptions which formulate the restricted problem, the model can shed light into dynamical structures that are beneficial for spaceflight applications. The Circular Restricted Three-Body Problem (CR3BP) is an example of a simplified model that is an autonomous dynamical system containing particular solutions[23]. The CR3BP uses a synodic frame that aligns one of the axis along the celestial bodies and the system's barycenter[46]. Another axis is perpendicular to the orbit plane of the bodies, and the final frame completes the right-hand triad. The CR3BP admits particular solutions such as equilibrium points, periodic and quasi-periodic trajectories, and invariant manifolds. Equilibrium points, also referred to as Lagrange or libration points, appear to be motionless in the CR3BP.

Repeating orbits which are periodic or quasi-periodic, originally found by Poincaré[46], can be found around these points, and have been of interest to mission designers based on their stability, location, and geometry.

1.2   Survey of Transfer Design in the CR3BP

Transfers in the CR3BP have been of interest to astrodynamicists to facilitate current and future mission design objectives. Creating these transfers require path planning techniques to form initial guess trajectories. These paths can then be corrected to form continuous solutions and ultimately optimized to reduce the propellant required or time of flight. Initial path generation in the CR3BP stems from dynamical systems theory to systematically explore possible types of solutions[19]. Leveraging such structures have been the focus of research into transfer design. Gómez et al. in [14] introduce the concept of utilizing invariant manifolds for transfers, and Barden in [3] applies this concept to generate transfers between halo periodic orbits in the Sun-Earth system. Gómez et al. in [16] and Barden, Howell, and Lo in [19] apply invariant manifolds and heteroclinic connections to design transfers between Lagrange point orbits in the Sun-Earth and Earth-Moon systems. These heteroclinic connections offer low cost trajectories as the natural motion can transfer the spacecraft from one periodic orbit to another. Parker, Davis, and Born in [35] explore leveraging invariant manifolds and constructing periodic orbit chains to form impulsive transfers between Lagrange point periodic orbits. Their work explores single-maneuver transfers from a departing periodic orbit to a heteroclinic connection to the arrival periodic orbit. Vaquero and Howell in [48] utilize an orbit chain method to planar and spatial resonant periodic orbits to find Lagrange point tour transfers in the Earth-Moon system. Restrepo and Russell in [41, 42] explore patching periodic orbits in the CR3BP, similar to patching conic arcs in the two-body problem, to build transfer mechanisms. This systematic strategy is beneficial in prototyping many guess paths from pre-computed solutions. Pritchett, Zimovan, and Howell in [37] demonstrate multi-link orbit chaining to form initial guesses for transfers. They utilize collocation based optimization techniques to recover fuel-optimal transfers between several Lagrange point orbits.

1.3   Thesis Overview

This research focuses on designing low thrust transfers between periodic orbits in the Earth-Moon system. The relevant dynamics and numerical methods are covered. Then methods for transfer design followed by examples are presented. A summary of each chapter is provided below:

- Chapter 2: This chapter derives the equations of motion for the CR3BP and introduces a convenient non-dimensionalization setup for characterizing the system. Additionally, thrust-enabled equations of motion are derived for trajectory segments with spacecraft control.

- Chapter 3: Certain numerical methods are essential for analysis in the CR3BP. This section begins by introducing the state transition matrix which is a useful linearization of the dynamics. The single and multiple shooting schemes are formulated in this chapter which serve as the basis for the corrections process to recover continuous trajectories.

- Chapter 4: Now that the system dynamics and relevant numerical methods are established, we can begin exploring particular solutions that exist in the CR3BP. The Jacobi constant of motion, equilibrium points, and periodic orbits are introduced. Specifically, the generation of planar, spatial, and resonant periodic orbits in the Earth-Moon system are shown. Finally, invariant manifolds, which are a unique property of the unstable periodic orbits are discussed, which are essential in the transfer design process.

- Chapter 5: This chapter outlines the transfer design process which is the focus of this thesis. Leveraging invariant manifolds, orbit chaining, corrections, continuation, and optimization are discussed here to design low thrust transfers between periodic orbits.

- Chapter 6: Examples of incorporating initial path generation techniques, corrections, continuation, and optimization are disused in this chapter. The first example explores generating sets of feasible transfers between subsets of the L_1 northern to L_2 southern halo periodic orbit families. Point case optimizations and continuation are used to update the

family and reduce the propellant cost for all feasible solutions. The next example is the NRHO to DRO transfer design problem which investigates two different initial guess paths and two spacecraft models to compare post-optimized results for varying initial guesses.

- Chapter 7: The final chapter summarizes the techniques for constructing low thrust transfers in the CR3BP. Additionally, recommendations for follow-on work are proposed.

Chapter 2

Circular Restricted Three Body Problem

The three body problem analyzes the motion of a massless particle under the gravitational influence of two massive bodies - the primary and secondary. This dynamical model approximates common operational environments for spacecraft missions within the Earth-Moon system. Additionally, unique low fuel cost trajectory opportunities is explored in this model compared to the traditional two-body problem. In this chapter, the governing equations of motion of this dynamical system are derived for the particle assumed to be a spacecraft, first for natural motion and then with low thrust. Unique properties of this system that are useful in trajectory design are explored in Chapter 4 after an overview of required numerical methods which is presented in Chapter 3.

2.1 Equations of Motion

To derive the equations of motion of the system, we begin with a by analyzing a general case with dimensional quantities. Then simplifying assumptions and nondimensionalization will help reduce the complexity of the model. Finally, the equations of motion are written in a frame that rotates with the primary and secondary body[46].

Consider the motion of three bodies as shown in Figure 2.1. The inertial frame is defined by axes $\hat{X}$, $\hat{Y}$, $\hat{Z}$, with origin O. State quantities with dimensions are denoted by a tilde and capital letters indicate the elements are in an inertial frame. Each body is assumed to be a point-mass and their positions are denoted by $\vec{R}$ followed by the corresponding subscript. The complete state
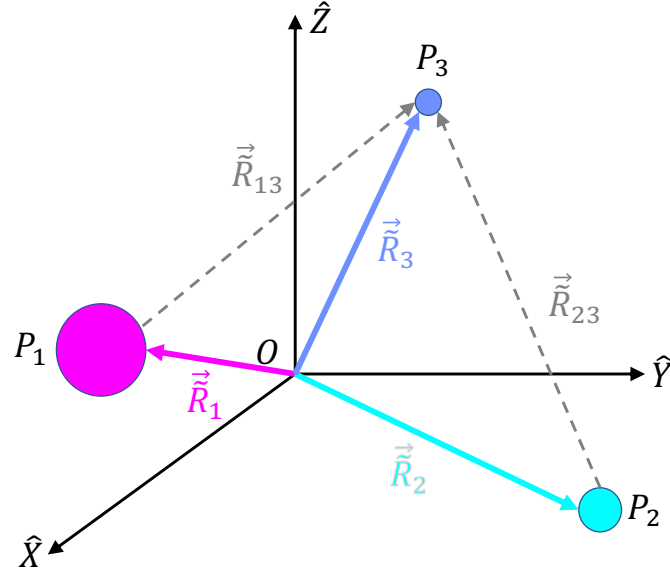
Figure 2.1: Motion of a primary (P1), secondary (P2), and third body (P3) as represented in the inertial frame.

vector of body i is given by:

$$\vec{\tilde{X}}_i = [\tilde{X}_i, \quad \tilde{Y}_i, \quad \tilde{Z}_i, \quad \dot{\tilde{X}}_i, \quad \dot{\tilde{Y}}_i, \quad \dot{\tilde{Z}}_i]^T \tag{2.1}$$

for i=1,2,3. Additionally, relative position vectors, denoted by $\vec{\tilde{R}}_{ij}$ in Figure 2.1 are grey dashed arrows. The first number in the subscript indicates the originating body and the second is the target body. The governing equations of motion of the third body written in the inertial frame using Newton's Law of Gravitation as:

$$\ddot{\vec{\tilde{R}}}_3 = -\frac{\tilde{G}\tilde{M}_1}{\tilde{R}_{13}^3}\vec{\tilde{R}}_{13} - \frac{\tilde{G}\tilde{M}_2}{\tilde{R}_{23}^3}\vec{\tilde{R}}_{23} \tag{2.2}$$

where $\tilde{G}$ is the gravitational constant, $\tilde{R}_{13}$ and $\tilde{R}_{23}$ are vector norms, and $\tilde{M}$ is the mass of each body.

Applying assumptions to the dynamical model can help simplify the problem and uncover useful insights[46]. First, the mass of the third body P_3 is considered to be negligible and won't have gravitational influence on the motion of the primary or secondary. The celestial body with

the greatest mass is P_1 and is referred to as the primary. Subsequently, the secondary is the celestial body with the smaller mass. The masses of the primary and secondary are uniform and unchanging, and so their motion about the barycenter is modeled with the two-body problem. Further, the system's time dependency is removed if we assume the primary and secondary follow circular orbits about the barycenter and relate the spacecraft's motion to the motion of the celestial bodies. These assumptions form the basis of the circular restricted three body problem (CR3BP).

A normalization scheme is useful to improve the condition of the system parameters. The dimensional quantities for mass, time, and length often have different magnitudes which can result in challenges applying numerical methods. Therefore, mass, length, and time characteristic quantities of the system are used to normalize the equations of motion. Note that in the following derivation system parameters and state elements without a tilde indicate non-dimensional quantities. Let's begin by defining the system characteristic mass m^* as $\tilde{M}_1 + \tilde{M}_2$. The primary and secondary follow two-body circular orbits and so motion produces a constant semi-major axis. This can be used to non-dimensionalize length l^* and time t^* given the orbit period equation. The following quantities represent the characteristic mass, length, and time[23].

$$m^* = \tilde{M}_1 + \tilde{M}_2 \qquad l^* = \tilde{R}_1 + \tilde{R}_2 \qquad t^* = \left(\frac{(l^*)^3}{\tilde{G}m^*}\right)^{1/2} \qquad (2.3)$$

Converting between dimensional and nondimensional quantities is performed using the following relationships:

$$m = \frac{\tilde{M}}{m^*} \qquad l = \frac{\tilde{L}}{l^*} \qquad t = \frac{\tilde{T}}{t^*} \qquad (2.4)$$

where $\tilde{M}$, $\tilde{L}$, and $\tilde{T}$ are dimensional mass, length, and time quantities whereas m, l, and t are the associated nondimensional quantities. This formulation is convenient as the nondimensional gravitational constant G simply becomes 1 when the proceeding quantities are substituted. This nondimensionalization results in definition of the mass ratio μ as:

$$\mu = \frac{\tilde{M}_2}{m^*} \qquad (2.5)$$

The Earth-Moon system's mass parameter is on the order of 10^{-2} and for context, the Earth-Sun

system is 10^{-6}. Table 2.1 summarizes the nondimensional constants for the Earth-Moon system calculated from constants in [23].

Earth-Moon System Nondimensional Constants		
m^*	(kg)	$6.047175616 \times 10^{24}$
l^*	(km)	384400
t^*	(sec)	375190.261951844
μ	-	0.0121505842695422

Table 2.1: Earth-Moon System Nondimensional Constants

Using the characteristic quantities, we can relate the dimensional accelerations in the equations of motion to nondimensional quantities in the inertial frame. The X-component's dimensional acceleration is related to the non-dimensional quantity by:

$$\ddot{\tilde{X}}_3 = \frac{d}{d\tau}\left(\frac{d\tilde{X}_3}{d\tau}\right) = \frac{l^*}{(t^*)^2}\frac{d^2 X_3}{dt^2} \tag{2.6}$$

Eq.(2.2) is decomposed into its individual components from the vector equation. For example, the X-component becomes:

$$\ddot{\tilde{X}}_3 = -\frac{\tilde{G}\tilde{M}_1}{\tilde{R}_{13}^3}(\tilde{X}_3 - \tilde{X}_1) - \frac{\tilde{G}\tilde{M}_2}{\tilde{R}_{23}^3}(\tilde{X}_3 - \tilde{X}_2) \tag{2.7}$$

Equating the terms from Eq.(2.6) with the components of Eq.(2.7) and simplifying yields:

$$\ddot{X}_3 = -\frac{(1-\mu)(X_3 - X_1)}{R_{13}^2} - \frac{\mu(X_3 - X_2)}{R_{23}^2} \tag{2.8}$$

This process is repeated for the Y and Z-components and a vector function for the non-dimensional equations of motion with respect to a non-rotating inertial frame is written as:

$$\ddot{\vec{R}}_3 = -\frac{(1-\mu)(\vec{R}_3 - \vec{R}_1)}{R_{13}^2} - \frac{\mu(\vec{R}_3 - \vec{R}_2)}{R_{23}^2} \tag{2.9}$$

This expression is time dependent and thus the dynamical system is non-autonomous. The state components of the primary and secondary vary with respect to time as they orbit the system barycenter. This time dependency is eliminated if we incorporate this motion into the frame that the equations of motion are with respect to. Because the celestial bodies are in circular two-body orbits, the semi-major axis and period are constant. We can define a new rotating frame that is
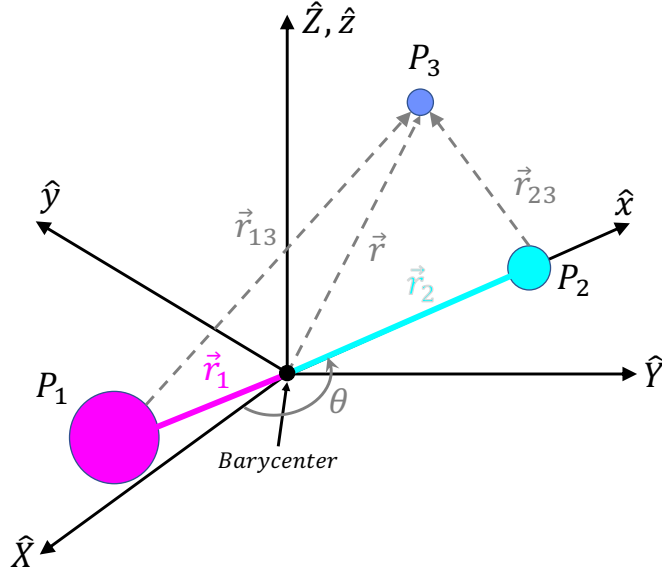
Figure 2.2: Location of a primary (P_1), secondary (P_2), and third body (P_3) represented in the inertial and rotating frame.

defined by the path of the primary and secondary as well as the orbit angular momentum[46]. Figure 2.2 consists of the inertial frame defined by axes $\hat{X}$, $\hat{Y}$, and $\hat{Z}$ and originated at the barycenter O. Note that because this frame is arbitrary, we can position it such that the X and Y-axes are in the plane defined by the celestial bodies' orbit. The diagram also includes a rotating frame defined by the axes $\hat{x}$, $\hat{y}$, and $\hat{z}$. The $\hat{x}$-axis is aligned with the semi-major axis of the celestial bodies where the positive direction is towards the secondary. The $\hat{z}$-axis is in the orbit angular momentum direction. The $\hat{y}$-axis completes the right-hand triad. This frame is rotating about the $\hat{z}$-axis with a period equal to that of primary and secondary. The angular velocity corresponding to angle θ is then defined by the mean motion of the system n times the time. From the diagram, $\vec{r}_1$ and $\vec{r}_2$ expressed in the inertial frame is:

$$\vec{R}_1(t) = [-\mu \cos(t), \quad -\mu \sin(t), \quad 0]^T$$
$$\vec{R}_2(t) = [(1-\mu)\cos(t), \quad (1-\mu)\sin(t), \quad 0]^T$$

(2.10)

where $\vec{R}_i(t) = [X_i(t), Y_i(t), Z_i(t)]^T$ for $i = 1, 2$. Plugging these quantities into the equations of

motion and separating the equations into each component yields:

$$\ddot{X}_3 = -\frac{(1-\mu)(X_3 + \mu\cos(t))}{R_{13}^3} - \frac{\mu(X_3 - (1-\mu)\cos(t))}{R_{23}^3}$$

$$\ddot{Y}_3 = -\frac{(1-\mu)(Y_3 + \mu\sin(t))}{R_{13}^3} - \frac{\mu(Y_3 - (1-\mu)\sin(t))}{R_{23}^3} \qquad (2.11)$$

$$\ddot{Z}_3 = -\frac{(1-\mu)Z_3}{R_{13}^3} - \frac{\mu Z_3}{R_{23}^3}$$

These equations are then reformulated with respect to the rotating frame to remove the time dependency. The following rotation matrix transforms the inertial coordinates (X, Y, Z) to rotating (x, y, z):

$$\begin{bmatrix} x \\ y \\ z \end{bmatrix} = \begin{bmatrix} \cos(t) & \sin(t) & 0 \\ -\sin(t) & \cos(t) & 0 \\ 0 & 0 & 1 \end{bmatrix} \begin{bmatrix} X \\ Y \\ Z \end{bmatrix} \qquad (2.12)$$

The coordinates for $\vec{r}_1$ and $\vec{r}_2$ in the rotating frame become:

$$\vec{r}_1 = [-\mu, \quad 0, \quad 0]^T$$

$$\vec{r}_2 = [1-\mu, \quad 0, \quad 0]^T \qquad (2.13)$$

The positions of the primary and secondary are independent of time in the rotating frame. We can now write the expression for an arbitrary vector in this frame, signified by the lower case unit vectors, with:

$$\vec{r} = x\hat{x} + y\hat{y} + z\hat{z} \qquad (2.14)$$

Using the transport theorem, the velocity vector in the rotating frame is related to the inertial frame derivative as:

$$\frac{^I d\vec{r}}{dt} = \frac{^R d\vec{r}}{dt} + {}^I\vec{\omega}^R \times \vec{r} \qquad (2.15)$$

where $\frac{^R d\vec{r}}{dt}$ is the derivative of the vector in the rotating frame. The angular velocity of the rotating frame with respect to the inertial frame is encoded through the ${}^I\vec{\omega}^R$ term. Note that because the $\hat{X}$-$\hat{Y}$ plane and the $\hat{x}$-$\hat{y}$ plane are co-planar, the angular velocity has a single component in the $+\hat{z}$ axis:

$$^I\vec{\omega}^R = n\hat{z} = 1\hat{z} \qquad (2.16)$$

The magnitude of the angular velocity is 1 due to the non-dimensional time definition. This effectively eliminates the time dependency of the equations of motion. Expanding the terms from Eq.(2.15) and rearranging yields the following expression:

$$\frac{^I d\vec{r}}{dt} = (\dot{x} - y)\hat{x} + (\dot{y} + x)\hat{y} + \dot{z}\hat{z} \tag{2.17}$$

To calculate the acceleration, the transport theorem is applied to Eq.(2.17):

$$\frac{^I d\vec{v}}{dt} = \frac{^R d\vec{v}}{dt} +^I \vec{\omega}^R \times \vec{v}$$

$$\frac{^I d\vec{v}}{dt} = (\ddot{x} - 2\dot{y} - x)\hat{x} + (\ddot{y} + 2\dot{x} - y)\hat{y} + \ddot{z}\hat{z} \tag{2.18}$$

Vector equations Eq.(2.18) and Eq.(2.9) are equated and applying the definitions from Eq.(2.13) which yields the non-dimensional circular restricted three body equations of motion as shown in state-space form[46]:

$$\dot{\vec{X}}(t) = \begin{bmatrix} \dot{x} \\ \dot{y} \\ \dot{z} \\ \ddot{x} \\ \ddot{y} \\ \ddot{z} \end{bmatrix} = \begin{bmatrix} \dot{x} \\ \dot{y} \\ \dot{z} \\ 2\dot{y} + x - \frac{(1-\mu)(x+\mu)}{r_1^3} - \frac{\mu(x-1+\mu)}{r_2^3} \\ -2\dot{x} + y - \frac{(1-\mu)y}{r_1^3} - \frac{\mu y}{r_2^3} \\ -\frac{(1-\mu)z}{r_1^3} - \frac{\mu z}{r_2^3} \end{bmatrix} \tag{2.19}$$

where $r_1 = \sqrt{(x+\mu)^2 + y^2 + z^2}$ and $r_2 = \sqrt{(x-1+\mu)^2 + y^2 + z^2}$.

The equations of motion depend on the gravitational forces from the celestial bodies of the system. A potential function that incorporates this information and the rotation of the rotating frame is used to form a pseudo-potential function U^*. The acceleration quantities from Eq.(2.19) is expressed using the pseudo-potential function's partial derivatives as[23]:

$$\frac{\partial U^*}{\partial x} = \ddot{x} - 2\dot{y}$$

$$\frac{\partial U^*}{\partial y} = \ddot{y} + 2\dot{x} \tag{2.20}$$

$$\frac{\partial U^*}{\partial z} = \ddot{z}$$

The pseudo-potential function that satisfies the preceding partial derivatives is:

$$U^* = \frac{1}{2}(x^2 + y^2) + \frac{1-\mu}{r_1} + \frac{\mu}{r_2} \tag{2.21}$$

where the first term is due to frame rotation and the second and third terms are due to the gravitational influence of the primary and secondary bodies. This equation is beneficial when presenting the system's constant of motion and dynamical insights.

2.2   Thrust-Enabled Equations of Motion

The existing equations of motion is modified to incorporate thrusting from the spacecraft. Additionally, the mass change due to thrusting is included in the dynamical model. At a particular instant in time the dimensional acceleration vector $\vec{\tilde{A}}$ due to thrusting is defined by:

$$\vec{\tilde{A}} = \frac{\vec{\tilde{T}}}{\tilde{M}} \tag{2.22}$$

where $\vec{\tilde{T}}$ is the dimensional thrust vector and $\tilde{M}$ is the dimensional mass at that instant. We can use this expression to find the appropriate conversion from dimensional to nondimensional acceleration to augment the equations of motion in Eq.(2.19). For this research, we will restrict the low-thrust engine's performance to: on at full thrust capability, or off with no thrust or mass decrement. We can define a constant term α applied to each component of acceleration such that the dimensional quantities of thrust and mass are converted. Because the engine is always on or off, a unit vector $\vec{u}$ is used to define the acceleration direction, and α is used to define the acceleration magnitude. The acceleration due to spacecraft thrusting is then defined as[4, 13]:

$$\vec{a} = \frac{\alpha}{m}\vec{u} \qquad \alpha = \frac{t^{*2}}{l^* \times 10^3} \frac{\tilde{T}_{max}}{\tilde{M}_i} \tag{2.23}$$

where $\tilde{T}_{max}$ is the maximum thrust output measured in Newtons, and $\tilde{M}_i$ is the initial spacecraft mass in kilograms, and m is the instantaneous nondimensional mass term. This mass term is constantly decreasing during numerical integration with the thrust enabled. At the initial nondimensional time this value is always equal to 1. The nondimensional mass carried through integration

can be thought of as a mass fraction of the initial mass and so post-integration the final value for m times the initial dimensional mass yields the final dimensional mass. This term is decremented through another constant term that converts the dimensional mass flow rate to a nondimensional quantity. Mass flow rate is defined as the thrust divided by the engine's specific impulse ($\tilde{I}_{sp}$) times the gravitational constant $\tilde{g}_0$ which is 9.80665 m/s^2. Converting this expression to the nondimensional quantities yields the mass flow constant (γ) defined as[4]:

$$\gamma = [t^*]\frac{\tilde{T}_{max}}{\tilde{g}_0\tilde{I}_{sp}\tilde{M}_i} \tag{2.24}$$

Finally, the thrust-enabled equations of motion in state-space form are defined as:

$$\dot{\vec{X}}(t) = \begin{bmatrix} \dot{x} \\ \dot{y} \\ \dot{z} \\ \ddot{x} \\ \ddot{y} \\ \ddot{z} \\ \dot{m} \end{bmatrix} = \begin{bmatrix} \dot{x} \\ \dot{y} \\ \dot{z} \\ 2\dot{y} + x - \frac{(1-\mu)(x+\mu)}{r_1^3} - \frac{\mu(x-1+\mu)}{r_2^3} + \left(\frac{\alpha}{m}\right)u_x \\ -2\dot{x} + y - \frac{(1-\mu)y}{r_1^3} - \frac{\mu y}{r_2^3} + \left(\frac{\alpha}{m}\right)u_y \\ -\frac{(1-\mu)z}{r_1^3} - \frac{\mu z}{r_2^3} + \left(\frac{\alpha}{m}\right)u_z \\ -\gamma \end{bmatrix} \tag{2.25}$$

In this research, existing propulsion system values to actual low thrust engines and spacecraft are not considered. However, a survey of current engines capabilities and spacecrafts was conducted to select reasonable values for maximum available thrust, specific impulse, and spacecraft mass. Table 2.2 summarizes the capabilities current and legacy operational spacecraft investigated.

Spacecraft	Approximate Acceleration (m/s^2)
Deep Space 1[40]	1.892×10^{-4}
Dawn[44]	7.473×10^{-5}
BepiColombo[22]	7.178×10^{-5}
Hayabusa[24]	4.706×10^{-5}

Table 2.2: Low-Thrust Spacecraft Accelerations

Chapter 3

Numerical Methods

Numerical methods are critical for analysis in the circular restricted three-body problem because analytical solutions are not admitted. This chapter summarizes the state transition matrix which derived from linearization of the dynamics around a trajectory. Then, correction methods are discussed which minimize segment state discontinuities to find continuous trajectories. This can be applied to compute periodic orbits or end-to-end transfers. The next part of the chapter covers methods of continuation to to generate sets of solutions from an initial continuous trajectory.

3.1   State Transition Matrix

The state transition matrix (STM) is a linear mapping from an initial variation relative to a reference trajectory to a variation at another time[23]. It must be noted that the use of the STM is conditioned on if the linear model sufficiently approximates the true non-linear dynamics of the system in the mapping time. For example, in highly non-linear regions, such as motion close to the primary or secondary in the system, the STM's ability to approximate the state along the trajectory for increasingly large time durations significantly degrades. The specifics of whether the STM reasonably approximates the true dynamics should be evaluated on a case-by-case basis. The STM is valuable to other numerical methods discussed here for trajectory corrections. Let's define $\Phi(t, t_0)$ as the STM. Figure 3.1 illustrates how the STM is used to map variations in the state along a trajectory where $\delta\vec{x}(t_0)$ is the vector of a variation in state at the initial time t_0, and $\delta\vec{x}(t)$ is the resulting variation vector propagated to time t by the STM. Thus, the STM is the partial
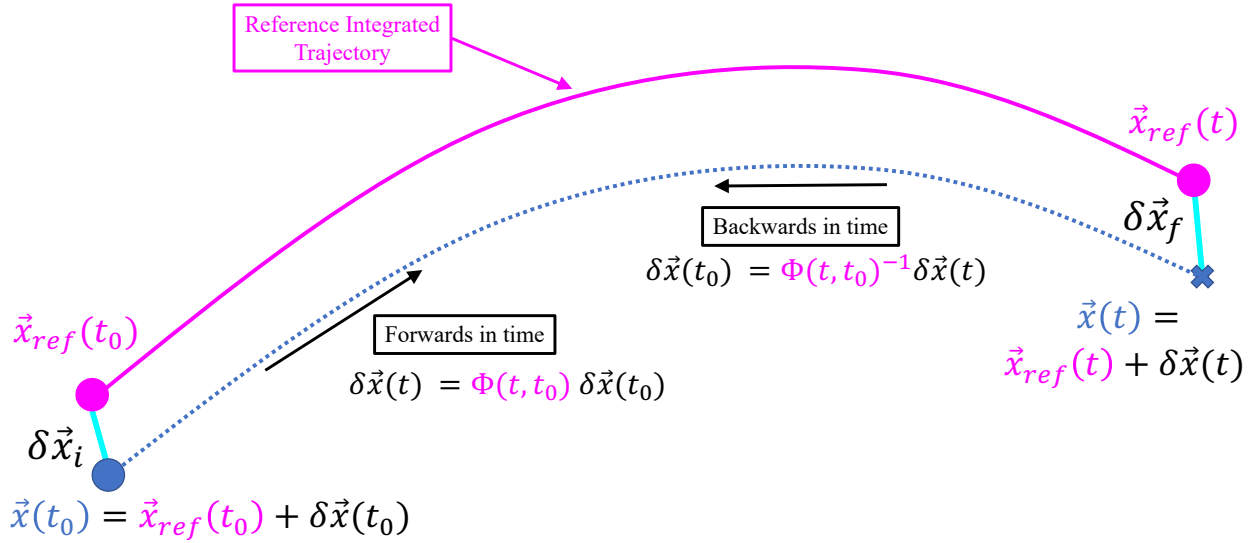
Figure 3.1: Mapping variations using the state transition matrix

derivative of the state at the final time with respect to the state at the initial time as shown below:

$$\Phi(t, t_0) = \frac{\partial \vec{X}(t)}{\partial \vec{X}(t_0)} \tag{3.1}$$

There are several properties of STMs that make them useful in the corrections schemes[4] discussed in the following sub-sections. For periodic orbits, the STM mapped from the initial time to the time exactly one period after is called the monodromy matrix [23]. This is helpful when trying to find periodic orbits in the CR3BP. When the initial and mapping time are identical, the STM is an identity matrix. State transition matrices can be decomposed into a product of multiple intermediate STMs. Finally, to backwards propagate, say from time t to the initial time t_0, the inverse of the STM is used [4].

We can generate the STM at each point along our trajectory during numerical integration. The state-space vectors from Eq.(2.19) and Eq.(2.25) need to be augmented to include the STM terms. Propagating the STM components in the integration for ballistic motion yields a state vector that is of size 42×1 (6 state variables and 36 STM components). Likewise, with thrust and mass

terms, the size is 110×1 (10 state variables and 100 STM components). Initializing a STM is the same as mapping it from the initial time to itself; therefore the pre-integration STM is simply an identity matrix that is the size of the propagated state vector. The state-space equations of motion account for STM propagation as it is the partial derivative of the EOMs with respect to the state vector:

$$\dot{\Phi}(t) = A(t)\Phi(t) \qquad A(t) = \frac{\partial \dot{\vec{X}}(t)}{\partial \vec{X}(t)} \qquad (3.2)$$

Taking the partials analytically yields the following matrix expressions to propagate the STM for natural motion:

$$A(t) = \begin{bmatrix} 0 & 0 & 0 & 1 & 0 & 0 \\ 0 & 0 & 0 & 0 & 1 & 0 \\ 0 & 0 & 0 & 0 & 0 & 1 \\ U_{xx}^* & U_{xy}^* & U_{xz}^* & 0 & 2 & 0 \\ U_{xy}^* & U_{yy}^* & U_{yz}^* & -2 & 0 & 0 \\ U_{xz}^* & U_{yz}^* & U_{zz}^* & 0 & 0 & 0 \end{bmatrix}_{6\times6} \qquad (3.3)$$

and for motion with thrusting:

$$A(t) = \begin{bmatrix} 0 & 0 & 0 & 1 & 0 & 0 & 0 & 0 & 0 & 0 \\ 0 & 0 & 0 & 0 & 1 & 0 & 0 & 0 & 0 & 0 \\ 0 & 0 & 0 & 0 & 0 & 1 & 0 & 0 & 0 & 0 \\ U_{xx}^* & U_{xy}^* & U_{xz}^* & 0 & 2 & 0 & -\frac{\alpha}{m^2}u_x & \frac{\alpha}{m} & 0 & 0 \\ U_{xy}^* & U_{yy}^* & U_{yz}^* & -2 & 0 & 0 & -\frac{\alpha}{m^2}u_y & 0 & \frac{\alpha}{m} & 0 \\ U_{xz}^* & U_{yz}^* & U_{zz}^* & 0 & 0 & 0 & -\frac{\alpha}{m^2}u_z & 0 & 0 & \frac{\alpha}{m} \\ 0 & 0 & 0 & 0 & 0 & 0 & 0 & 0 & 0 & 0 \\ 0 & 0 & 0 & 0 & 0 & 0 & 0 & 0 & 0 & 0 \\ 0 & 0 & 0 & 0 & 0 & 0 & 0 & 0 & 0 & 0 \\ 0 & 0 & 0 & 0 & 0 & 0 & 0 & 0 & 0 & 0 \end{bmatrix}_{10\times10} \qquad (3.4)$$

Components U^* followed by two subscripts indicate the second partial derivatives of the pseudo-

potential function from Eq.(2.21). These second-partial derivatives are shown below:

$$U_{xx}^* = 1 - \frac{1-\mu}{r_1^3} - \frac{\mu}{r_2^3} + \frac{3(1-\mu)(x+\mu)^2}{r_1^5} + \frac{3\mu(x-1+\mu)^2}{r_2^5}$$

$$U_{yy}^* = 1 - \frac{1-\mu}{r_1^3} - \frac{\mu}{r_2^3} + \frac{3y^2(1-\mu)}{r_1^5} + \frac{3\mu y^2}{r_2^5}$$

$$U_{zz}^* = -\frac{1-\mu}{r_1^3} + \frac{3z^2(1-\mu)}{r_1^5} - \frac{\mu}{r_2^3} + \frac{3\mu z^2}{r_2^5}$$

$$U_{xy}^* = U_{yx}^* = \frac{3y(1-\mu)(x+\mu)}{r_1^5} + \frac{3\mu y(x-1+\mu)}{r_2^5} \qquad (3.5)$$

$$U_{xz}^* = U_{zx}^* = \frac{3z(1-\mu)(x+\mu)}{r_1^5} + \frac{3\mu z(x-1+\mu)}{r_2^5}$$

$$U_{yz}^* = U_{zy}^* = \frac{3yz(1-\mu)}{r_1^5} + \frac{3\mu yz}{r_2^5}$$

where $r_1 = \sqrt{(x+\mu)^2 + y^2 + z^2}$ and $r_2 = \sqrt{(x-1+\mu)^2 + y^2 + z^2}$.

3.2   Correction Methods

3.2.1   Single Shooting

The single shooting method solves for the desired initial and terminal states by varying the initial conditions such that the desired terminal conditions are achieved. Figure 3.2 conceptually depicts an example of the single-shooting method applied to the trajectory design problem. An initial state $\vec{x}_i$ propagated by Δt is iterated on such that the TPBVP constraints are satisfied. This criteria is met when the initial and final states lie on the desired initial and terminal conditions to within a specified tolerance. When these conditions are met, the blue arc trajectory is sufficiently close to the true solution indicated as the desired trajectory.

In the context of computing periodic orbits in the CR3BP, the state contains the six spatial elements $\vec{x}$ and an orbit period element T. After propagating the initial state $\vec{x}_i$ by the period, the final state $\vec{x}_f$ must match the initial. Formulation of this method begins by defining a free variable vector $\vec{V}$ as shown:

$$\vec{V}_i = \left[x_i, \ y_i, \ z_i, \ \dot{x}_i, \ \dot{y}_i, \ \dot{z}_i, \ T_i \right]_{7\times1}^T \qquad (3.6)$$

This vector is modified such that our constraints of the TPBVP are satisfied. Let's define the
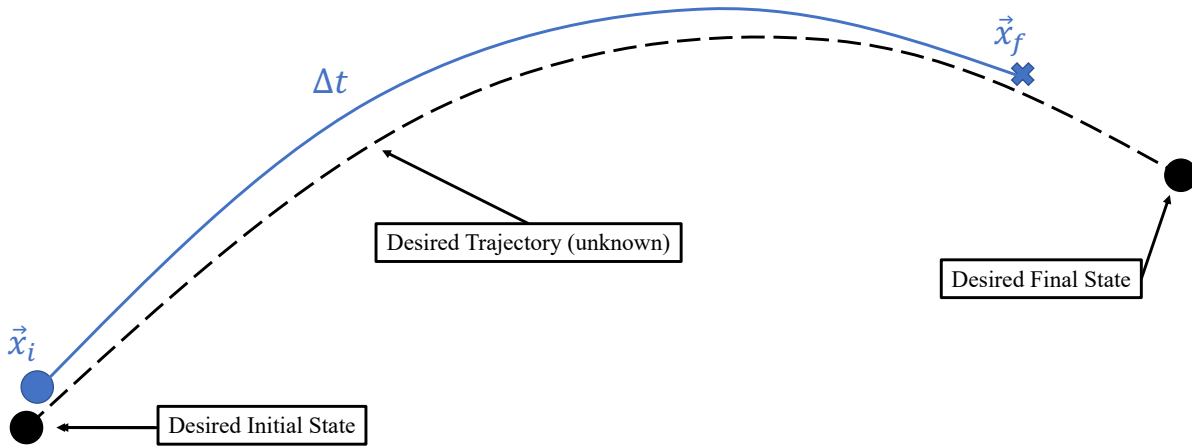
Figure 3.2: Single-shooting method overview

constraints vector as:

$$\vec{F}(\vec{V}) = [\vec{x}(t_i) - \vec{x}(t_f)]_{6\times 1} \tag{3.7}$$

which ensures state continuity to form a periodic orbit. We can employ Newton's root finding method to iterate $\vec{V}$ such that the desired free variable vector $\vec{V}_d$ satisfies the constraint formulation and thus the resulting constraint $\vec{F}(\vec{V}_d)$ is sufficiently close to $\vec{0}$. Assuming that $\vec{V}_i$ is sufficiently close to $\vec{V}_d$, a first-order Taylor series expansion of the constraint formulation around the initial free variable vector is:

$$\vec{F}(\vec{V}_d) = \vec{0} = \vec{F}(\vec{V}_i) + \frac{\partial \vec{F}}{\partial \vec{V}}\bigg|_{\vec{V}_i} \delta\vec{V} + H.O.T.s \tag{3.8}$$

where $\delta\vec{V}$ is the difference between $\vec{V}_d$ and $\vec{V}_i$. With the first-order approximation, we neglect the higher order terms ($H.O.T.s$) but this will require iterating on the free variable vector such that the constraint norm is within a specified tolerance parameter: $|\vec{F}(\vec{V}_i)| < \epsilon$. The Jacobian of the constraints with respect to the free variable vector will be referred to as $D\vec{F}(\vec{V})$. In this case, the Jacobian is expressed analytically using the state transition matrix defined earlier. Assuming this

matrix is invertible, the correction to update $\vec{V}_i$ to $\vec{V}_{i+1}$ becomes:

$$\vec{V}_{i+1} = \vec{V}_i - [D\vec{F}(\vec{V}_i)]^{-1}(\vec{F}(\vec{V}_i)) \tag{3.9}$$

This update equation is applicable only when the number of free variables and the number of constraints are equal. In the periodic orbit problem formulation, this condition isn't met. The minimum norm update, which is a pseudo-inverse method, is used which minimizes the norm of each step and is defined as[4]:

$$\vec{V}_{i+1} = \vec{V}_i - \rho(D\vec{F}(\vec{V}_i)^T[D\vec{F}(\vec{V}_i)D\vec{F}(\vec{V}_i)^T]^{-1}\vec{F}(\vec{V}_i)) \tag{3.10}$$

Additionally, a scaling term ρ is included to the update for algorithm performance. If the initial guess is sufficiently close to the desired solution, the Jacobian is full rank, and the partials and functions are continuous, Newton's method will converge in a quadratic manner. Step-size modulation strategies including the Wolfe conditions [5] can be beneficial to correct solutions in sensitive regions. The single shooting method's ability to converge on a solution is dependent on how accurately the linearization of the dynamics represent the true dynamics of the system. As discussed in the prior sub-section, for long propagations durations where the dynamical model is especially sensitive, the STM begins to inaccurately map the state. This negatively affects the update in Newton's method and thus can lead to divergent behavior. The ability to reset the STM mid-trajectory to shorten the propagation duration is beneficial, and this method is discussed in the next sub-section regarding multiple shooting.

3.2.2   Multiple Shooting

If the single shooting method is insufficient, a multiple shooting scheme is employed. This method is more robust than single shooting as the linearization approximation better approximates the non-linear dynamics along shorter propagation intervals. The implementation of the multiple shooting method discussed here is adapted from [4]. The trajectory is broken into segments and the constraint formulation is dependent on the next segment initial state. Figure 3.3 illustrates
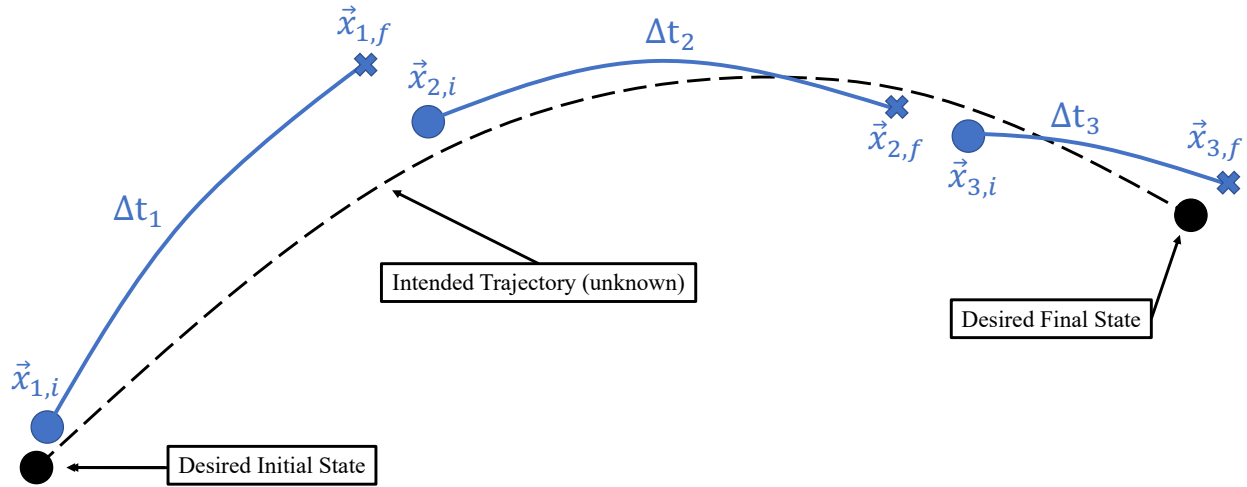
Figure 3.3: Multiple-shooting method overview

the components of a three-segment multiple shooting scheme between fixed initial and terminal states shown as black circles. These states can be either identical for finding periodic orbits, or along two different periodic orbits to find a transfer trajectory. The scheme attempts to patch intermediate arc discontinuities and thereby reducing the constraints norm to within a specified tolerance. To ensure continuity, the constraint function includes all six spatial elements between segments. Formulating the multiple shooting problem is similar to the single shooting scheme.

We begin by forming a free variable vector for each segment along the trajectory. The left-hand expression in Eq.(3.11) shows the free variable vector for a single segment j along the trajectory. The total free variable vector, shown on the right, consists of stacking each arc's free

variable vector.

$$\vec{V}_j = \begin{bmatrix} x_j \\ y_j \\ z_j \\ \dot{x}_j \\ \dot{y}_j \\ \dot{z}_j \\ \Delta t_j \end{bmatrix}_{7 \times 1} \qquad \vec{V} = \begin{bmatrix} \vec{V}_1 \\ \vec{V}_2 \\ \vdots \\ \vec{V}_n \end{bmatrix}_{7n \times 1} \qquad (3.11)$$

The total number of arcs along the trajectory is denoted by n.

Now that the updating variables vector is defined, we can define a set of constraints to model continuity. These are defined by a constraint function vector that ensures that the final state for the current arc j matches the initial state of the next arc $j + 1$. The starting and ending states along the periodic orbit need to be matched as well to ensure the boundary conditions are satisfied. The individual (left) and total (right) constraint vectors are shown in Eq.(3.12):

$$\vec{F}(\vec{V})_j = \begin{bmatrix} x_{j,f} - x_{j+1,i} \\ y_{j,f} - y_{j+1,i} \\ z_{j,f} - z_{j+1,i} \\ \dot{x}_{j,f} - \dot{x}_{j+1,i} \\ \dot{y}_{j,f} - \dot{y}_{j+1,i} \\ \dot{z}_{j,f} - \dot{z}_{j+1,i} \end{bmatrix}_{6 \times 1} \qquad \vec{F}(\vec{V}) = \begin{bmatrix} \vec{F}(\vec{V})_1 \\ \vec{F}(\vec{V})_2 \\ \vdots \\ \vec{F}(\vec{V})_n \end{bmatrix}_{6n \times 1} \qquad (3.12)$$

For periodic orbits, the final constraint vector $\vec{F}(\vec{V})_n$ is the difference between the final segment's post-propagated state $(\vec{x}_{n,f})$ and the initial state vector $(\vec{x}_{1,i})$. As discussed in the single shooting scheme setup, the same minimum norm update equation Eq.(3.10) is used to iterate on the free

variable vector. For clarity, the Jacobian matrix is shown in it's sub-matrix blocks below:

$$DF(\vec{V}) = \frac{\partial \vec{F}}{\partial \vec{V}} = \begin{bmatrix} \frac{\partial \vec{F}_1}{\partial \vec{V}_1}, \frac{\partial \vec{F}_1}{\partial \vec{V}_2}, \cdots, \frac{\partial \vec{F}_1}{\partial \vec{V}_n} \\ \frac{\partial \vec{F}_2}{\partial \vec{V}_1}, \frac{\partial \vec{F}_2}{\partial \vec{V}_2}, \cdots, \frac{\partial \vec{F}_2}{\partial \vec{V}_n} \\ \vdots \\ \frac{\partial \vec{F}_n}{\partial \vec{V}_1}, \frac{\partial \vec{F}_n}{\partial \vec{V}_2}, \cdots, \frac{\partial \vec{F}_n}{\partial \vec{V}_n} \end{bmatrix} \tag{3.13}$$

The Jacobian matrix is of dimensions: $\text{length}(\vec{F}(\vec{V})) \times \text{length}(\vec{V})$. We can look at a single block matrix within this update term. Eq.(3.14) is the first arc and constraint assuming a full-state continuity.

$$\frac{\partial \vec{F}_1}{\partial \vec{V}_1} = \begin{bmatrix} \frac{\partial (\vec{x}_{1,f} - \vec{x}_2)}{\partial \vec{x}_1}, \frac{\partial (\vec{x}_{1,f} - \vec{x}_2)}{\partial \Delta t_1} \end{bmatrix}_{6 \times 7} \tag{3.14}$$

The already computed state transition matrix is leveraged to define the partials derivatives of the integrated state $\vec{x}_{1,f}$ with respect to the initial state $\vec{x}_1$. Also, the partials derivatives of the integrated state with respect to time Δt_1 is simply the velocity and acceleration at the final state. With this in mind, we can rewrite Eq.(3.14) and the partial of the first constraint with respect to the second free variable state as:

$$\frac{\partial \vec{F}_1}{\partial \vec{V}_1} = \begin{bmatrix} \Phi_1(\Delta t, 0), \dot{\vec{x}}_{1,f} \end{bmatrix}_{6 \times 7} \qquad \frac{\partial \vec{F}_1}{\partial \vec{V}_2} = \begin{bmatrix} -\mathbb{I}_{6 \times 6}, \mathbb{0}_{6 \times 1} \end{bmatrix}_{6 \times 7} \tag{3.15}$$

This process is repeated for each free variable and constraint in the total $DF(\vec{V})$ matrix.

Figure 3.4 illustrates the multiple shooting method applied to periodic orbit correction. In the trajectory visual, the grey circles represent the initial states for each segment and the grey dashed lines indicate these states propagated by the initial guess time. The colored segments indicate the converged solution which has removed state discontinuities within a specified tolerance. The trajectory orbits a stationary point known as the L_1 Lagrange point, and this is covered in the next section. The right plot shows the norm of the constraint vector after each iteration. We expect quadratic convergence in the solution and this is evident by the log-scale on the y-axis.

Similar to the periodic orbit case demonstrated above, end-to-end transfers is found using coasting and thrusting arcs. Figure 3.5 illustrates the concept of a multiple shooting trajectory with
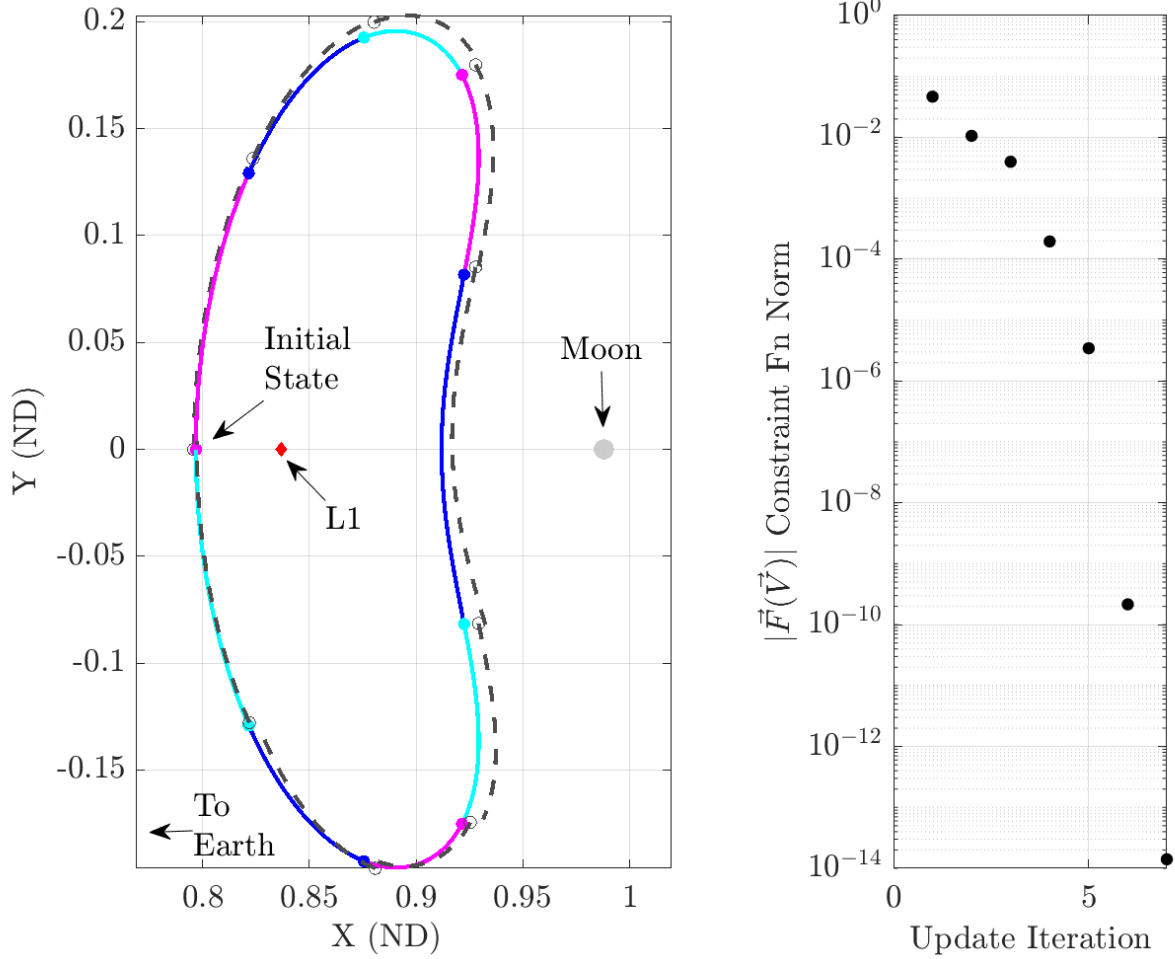
Figure 3.4: Example of multiple shooting applied to correct a L_1 Lyapunov periodic orbit

a single thrusting arc and two subsequent coasting arcs. This diagram differs from the previous one as it demonstrates a corrected solution where the initial and final states along each intermediate arc are overlapping. The thrust-enabled arcs have a modified free variable vector to include the control directions u_x, u_y, u_z, mass m, and a slack variable β[4]. This free variable vector, for an arbitrary segment j, is shown below:

$$\vec{V_j} = \begin{bmatrix} x_j, & y_j, & z_j, & \dot{x}_j, & \dot{y}_j, & \dot{z}_j, & u_{x,j}, & u_{y,j}, & u_{z,j}, & m_j, & \Delta t_j, & \beta_j \end{bmatrix}^T_{12 \times 1} \qquad (3.16)$$

Note that the control vector is held constant in the rotating frame along the arc. Because control and mass are propagated during integration, additional constraints need to be imposed on the arcs
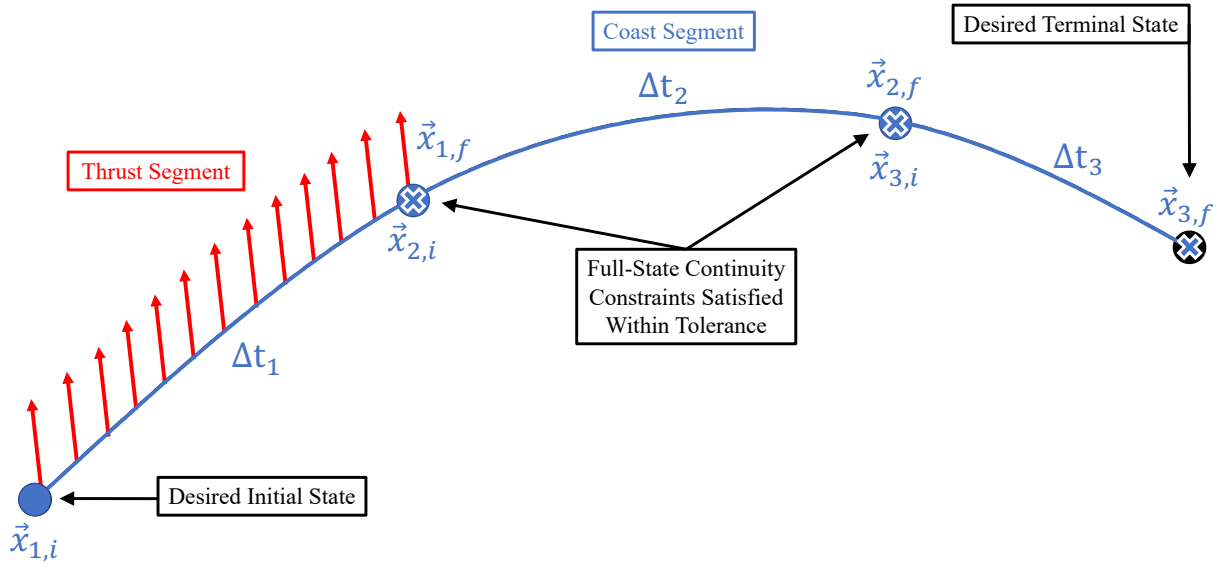
Figure 3.5: Diagram of the multiple-shooting method with thrusting and coasting arcs

to ensure continuity in the solution, and this is seen in the following constraint vector:

$$\vec{F}(\vec{V})_j = \begin{bmatrix} x_{j,f} - x_{j+1,i} \\ y_{j,f} - y_{j+1,i} \\ z_{j,f} - z_{j+1,i} \\ \dot{x}_{j,f} - \dot{x}_{j+1,i} \\ \dot{y}_{j,f} - \dot{y}_{j+1,i} \\ \dot{z}_{j,f} - \dot{z}_{j+1,i} \\ |\vec{u_j}|^2 - 1 \\ m_{j,f} - m_{j+1,i} \\ \Delta t_j - \beta_j^2 \end{bmatrix}_{9\times1} \tag{3.17}$$

In this formulation, the norm of the control vector squared should be equal to 1 to ensure the vector is unit. The mass post-propagation of the current segment $m_{j,f}$ must be equal to the initial mass of the next segment $m_{j+1,i}$. Additionally, a slack variable β is introduced to ensure

that the propagation time is always greater than zero. The Jacobian matrix from Eq.(3.13) is still applicable for the free-variable vector update equation Eq.(3.10). It is important to note that various constraint formulations is imposed on transfer design problems. For example, when designing a transfer between two periodic orbits, the initial and final segment constraints must include the departure and target periodic orbits states. The Jacobian matrix sub-blocks must account for combinations of thrusting and coasting segments.

3.3   Continuation Methods

Continuation methods are valuable in computing a sets of solutions from a single result. For example, this technique is useful in computing periodic orbit families and is used to find sets of transfers. Two well known approaches are the natural parameter and the pseudo-arclength methods. Both methods attempt to traverse the constraint manifold finding particular solutions along this n-dimensional path. Natural parameter continuity is beneficial when physical constraints are desired on the next solution. For example, when computing a set of periodic orbits if the difference in Jacobi constant between each orbit is to remain fixed, this method ensures this constraint is met. For transfers, natural parameter continuation is useful to find sets solutions for varying spacecraft capabilities. It is important to note that the natural parameter method can step too far from the constraint manifold which can result in not being able to find a solution. The pseudo-arclength method attempts to step in the direction of the gradient of solutions to remedy this. This method is beneficial in certain cases of periodic orbit family generation.

3.3.1   Natural Parameter

The natural parameter continuation method involves perturbing a single parameter to form a new initial guess. Then this guess is corrected with modified constraints to enforce the parameter's value. This method relies on an arbitrary step size for the natural parameter, which may need to be reduced to adequately follow the constraints manifold. For periodic orbits, we can modify the constraint vector formulation to enforce the natural parameter value. For example, the following

is the last constraint sub-vector for a multiple shooting correction scheme:

$$\vec{F}(\vec{V})_n = \begin{bmatrix} x_{n,f} - x_{1,i} \\ y_{n,f} - y_{1,i} \\ \vdots \\ \dot{z}_{n,f} - \dot{z}_{1,i} \\ p - (p^* + \Delta p) \end{bmatrix} \tag{3.18}$$

where n is the final segment in the multiple shooting discretization, p is the natural parameter, p^* is the previous solution's value for the natural parameter, and Δp is the step size. The shooting scheme is iterated on until a solution is found with this constraint. Note that with this additional constraint, the number of constraints and free variables are equal and so a single solution is recovered.

3.3.2   Pseudo-Arclength

Instead of relying on a physical quantity as a step for the next solution, the pseudo-arclength method attempts to step in the tangent direction to the solution manifold. Figure 3.6, adapted from [4], demonstrates the difference in the step taken by the pseudo-arclength method Δs versus the natural parameter method Δp along the constraint manifold. From the diagram it is seen that stepping along the constraint manifold's gradient yields a much closer initial guess to the manifold and so the corrections required are smaller. While the step size doesn't exactly yield a solution with a specific natural parameter p_{np}, it is able to take a larger step. The step length can be varied by the Wolfe conditions[5] in order to maximize the step direction. The pseudo-arclength method initial guess free variable vector $\vec{V}$ is formulated by[4]:

$$\vec{V} = \vec{V}^* + \Delta s \hat{n}^* \tag{3.19}$$

where $\vec{V}^*$ is the previous solution's corrected free variable vector, Δs is a scaling term, and $\hat{n}^*$ is the unit nullspace vector of the previous solution's Jacobian matrix $D\vec{F}(\vec{V}^*)$. The nullspace is the basis for vectors tangent to the constraint manifold and so stepping in this direction by an arbitrary scaling term yields the appropriate pseudo-arclength step. A modified constraint is required to limit
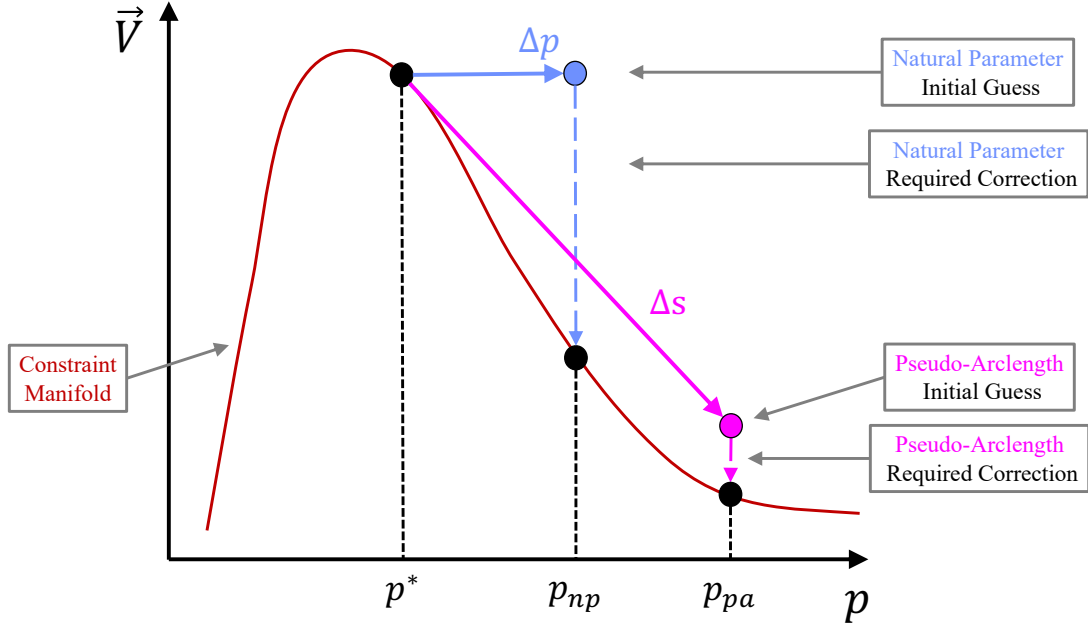
Figure 3.6: Conceptual overview of natural parameter and pseudo-arclength continuation methods

the distance between solutions in the tangent vector space which is formulated as:

$$\vec{H}(\vec{V}) = \begin{bmatrix} \vec{F}(\vec{V}) \\ (\vec{V} - \vec{V}^*)^T \hat{n}^* - \Delta s \end{bmatrix} \tag{3.20}$$

Similar to the shooting scheme correction methods, Newton's method is applied with this modified constraint formulation to converge on a solution. The update equation:

$$\vec{V}_{i+1} = \vec{V}_i - D\vec{H}(\vec{V}_i)^{-1}\vec{H}(\vec{V}_i) \tag{3.21}$$

is used to find a particular solution for $\vec{V}$ where the Jacobian of the constraint is:

$$D\vec{H}(\vec{V}_i) = \frac{\partial \vec{H}(\vec{V}_i)}{\partial \vec{V}_i} = \begin{bmatrix} D\vec{F}(\vec{V}_i) \\ \hat{n}^* \end{bmatrix} \tag{3.22}$$

The method is iterated on until the constraint vector norm is within a specified tolerance parameter. The process is repeated where the computed solution now becomes the $\vec{V}^*$ for the next solution in the family.

<center>

Chapter 4

Particular Solutions

</center>

Despite the CR3BP being an inherently chaotic system, certain structures exist which are beneficial in understanding the dynamics and formulating potential trajectories. This chapter begins by introducing the Jacobi constant which is useful in categorization of trajectories. Next, equilibrium points and their associated stability are assessed. Certain types of repeating orbits, referred to as periodic orbits, are permitted in the CR3BP which are useful for designing missions. Some periodic orbits exhibit naturally departing and arriving structures that are beneficial in low-cost transfer design. Finally, a categorization method from dynamical systems theory is discussed to find good initial guesses for the transfer design problem.

4.1   Constant of Motion

While the CR3BP does not admit sufficient constants of motion for an analytically solution, a conserved quantity pertaining to the system's potential energy is helpful. The Jacobi constant is essential in categorizing families trajectories, validating numerical integration methods, and provides insight into the energy difference between transfer orbits[23]. We begin the derivation of the Jacobi Constant C with the pseudo-potential function from Eq.(2.21) and by recalling the relationship of the pseudo-potential function to the equations of motion from Eq.(2.20). Taking the dot product of the acceleration and velocity vectors and canceling terms yield:

$$\ddot{x}\dot{x} + \ddot{y}\dot{y} + \ddot{z}\dot{z} = \frac{\partial U^*}{\partial x}\dot{x} + \frac{\partial U^*}{\partial y}\dot{y} + \frac{\partial U^*}{\partial z}\dot{z} \qquad (4.1)$$

and because $\frac{\partial U^*}{\partial t} = 0$, the total derivative of the system must be equal to:

$$\frac{dU^*}{dt} = \frac{\partial U^*}{\partial x}\frac{dx}{dt} + \frac{\partial U^*}{\partial y}\frac{dy}{dt} + \frac{\partial U^*}{\partial z}\frac{dz}{dt} \tag{4.2}$$

Therefore, Eq.(4.1) is rewritten as:

$$\ddot{x}\dot{x} + \ddot{y}\dot{y} + \ddot{z}\dot{z} = \frac{dU^*}{dt} \tag{4.3}$$

and with a substitution to the left-hand-side to incorporate the velocity term: $v^2 = \dot{x}^2 + \dot{y}^2 + \dot{z}^2$

we can rewrite this expression as:

$$\frac{1}{2}\frac{d}{dt}v^2 = \frac{dU^*}{dt} \tag{4.4}$$

Integrating the equation above and including the integration constant C yields:

$$v^2 = 2U^* - C \tag{4.5}$$

After substituting known quantities, we are left with the Jacobi Constant defined as [46]:

$$C = (x^2 + y^2) + \frac{2(1-\mu)}{r_1} + \frac{2\mu}{r_2} - (\dot{x}^2 + \dot{y}^2 + \dot{z}^2) \tag{4.6}$$

The Jacobi constant has an inverse relationship with the energy. Knowing the Jacobi constant of a trajectory is beneficial as certain natural motion becomes bounded within accessible regions in the dynamical system.

4.2   Equilibrium Points and Stability

In the CR3BP and in the rotating frame, certain points exist where the relative motion of such point is equal to that of the motion of the primaries. These points are known as Lagrange or Libration points and are denoted by an L followed by a numerical subscript to indicate the exact equilibrium point. Five Lagrange points exist in the CR3BP and their locations is found by employing analytical and numerical methods. Every point is co-planar with the primary and secondary of the system[46], and Lagrange points L_1, L_2, and L_3 are also co-linear along the rotating

frame's x-axis. The Lagrange points of any CR3BP system is found by the following derivation. By definition, in the rotating frame these points appear stationary and so:

$$\dot{x} = \dot{y} = \dot{z} = 0, \qquad \frac{\partial U^*}{\partial x} = \frac{\partial U^*}{\partial y} = \frac{\partial U^*}{\partial z} = 0 \tag{4.7}$$

Every point is co-planar due to the following condition:

$$\frac{\partial U^*}{\partial z} = 0 = -\frac{(1-\mu)z}{r_1^3} - \frac{\mu z}{r_2^3} \tag{4.8}$$

where $z = 0$ to satisfy the equality. Similarly, the co-linear solutions are found by setting $y = 0$ in the following condition:

$$\frac{\partial U^*}{\partial y} = 0 = y - \frac{(1-\mu)y}{r_1^3} - \frac{\mu y}{r_2^3} \tag{4.9}$$

The remaining condition is:

$$\frac{\partial U^*}{\partial x} = 0 = x - \frac{(1-\mu)(x+\mu)}{r_1^3} - \frac{\mu(x-1+\mu)}{r_2^3} \tag{4.10}$$

where $r_1 = \mid x + \mu \mid^3$ and $r_2 = \mid x - 1 + \mu \mid^3$ after setting $y = z = 0$. To satisfy this final condition, three unique solutions for x exist and are located where: $x < -\mu$, $-\mu < x < 1 - \mu$, and $x > 1 - \mu$. Newton's root finding method is useful to find these solutions. The initial guess for the Lagrange point between the primary and secondary, L_1, is simple as it is bounded on either side. If the mass ratio, μ is very small, a good initial guess would be to offset this point closer to the secondary body. The L_2 point, which is on the right side of the secondary would be of roughly similar distance from the secondary as L_1. Finally L_3 is on the far left side of the axis, and a good initial guess would be roughly the opposite distance from the barycenter as the secondary.

The triangular Lagrange points L_4 and L_5 are not co-linear and is found using geometry[32]. Their locations form an equilateral triangle with two sides consisting of the primary and secondary bodies. The third side is in the positive y-direction for L_4 and negative direction for L_5. The distance between the celestial bodies is unity, and so the x-coordinate of both L_4 and L_5 is simply half the distance from the primary to the secondary. The associated x-component is $\frac{1}{2} - \mu$. To find the y-coordinate, we can plug this value into the distance formula from the primary to the Lagrange

point r_{13} and the secondary to the Lagrange point r_{23}. Doing so yields two possible solutions for the y-coordinate: $\pm\frac{\sqrt{3}}{2}$, which correspond to the L_4 and L_5 points.

Figure 4.1 depicts all five Lagrange points in the Earth-Moon CR3BP. Lagrange points L_1, L_2, and L_3 are co-linear with the x-axis and equilateral triangles, shown as grey dashed lines, are formed to the L_4 and L_5 points. Table 4.1 includes each equilibrium points' non-dimensional position and Jacobi constant at zero velocity.
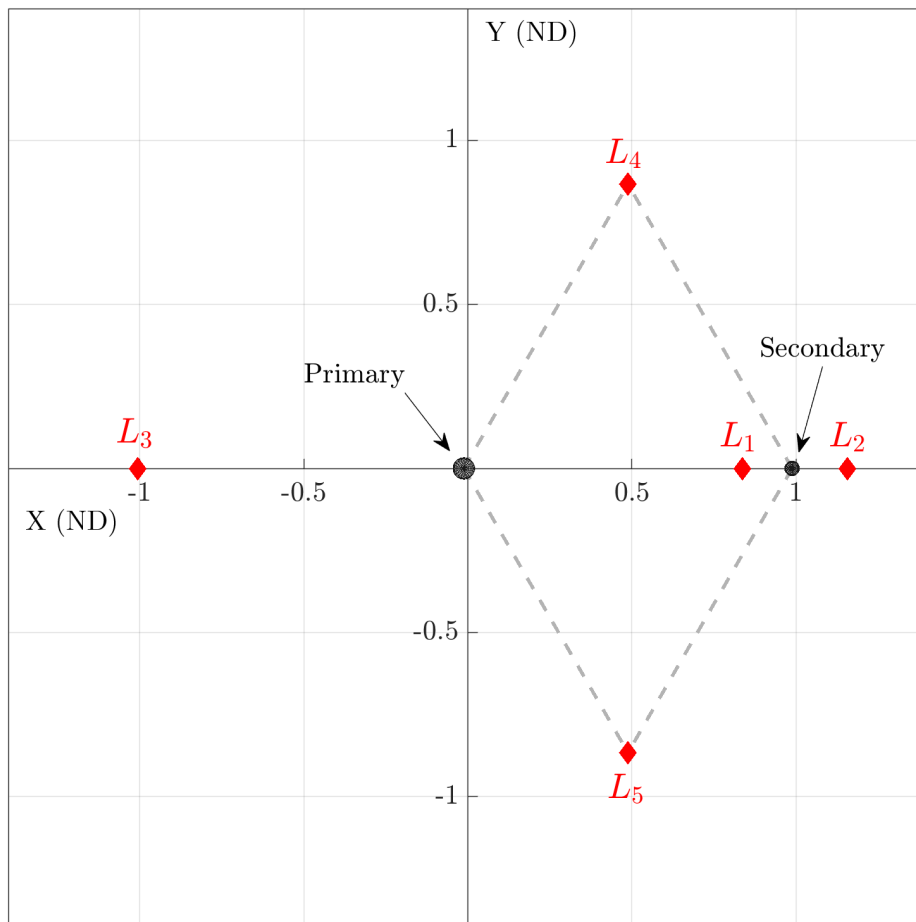
Figure 4.1: Lagrange point locations in the Earth-Moon system

Lagrange Point	x (ND)	y (ND)	z (ND)	C (ND)
L_1	0.836915132366261	0	0	3.18834110539176
L_2	1.15568216029081	0	0	3.17216045039168
L_3	-1.00506264525194	0	0	3.01214714934122
L_4	0.487849415730458	0.866025403784439	0	2.98799705242855
L_5	0.487849415730458	-0.866025403784439	0	2.98799705242855

Table 4.1: Earth-Moon System Lagrange Point Positions and Jacobi Constants

Each Lagrange point has an associated stability criteria which is helpful in determining the dynamical behavior in the vicinity of these points. This criteria is evaluated by linearizing the dynamics about such points and performing a stability analysis of the in-plane and out-of-plane modes[46]. In the system, a total of six eigenvalues exist where four pertain to in-plane modes and two are for out-of-plane modes. Recall the equations of motion for the CR3BP in Eq.(2.20) which are expressed using the pseudo-potential function's partial derivatives. Small perturbations about the equilibrium state, denoted by subscript e, are defined as:

$$\xi = x - x_e$$
$$\eta = y - y_e \qquad (4.11)$$
$$\delta = z - z_e$$

Using the Taylor series expansion and neglecting higher-order-terms, the CR3BP equations of motion are linearized about the equilibrium states $\bar{x}_{eq}$ as:

$$\ddot{\xi} - 2\dot{\eta} = U_{xx}^* \mid_{\bar{x}_{eq}} \xi + U_{xy}^* \mid_{\bar{x}_{eq}} \eta + U_{xz}^* \mid_{\bar{x}_{eq}} \delta$$
$$\ddot{\eta} + 2\dot{\xi} = U_{yx}^* \mid_{\bar{x}_{eq}} \xi + U_{yy}^* \mid_{\bar{x}_{eq}} \eta + U_{yz}^* \mid_{\bar{x}_{eq}} \delta \qquad (4.12)$$
$$\ddot{\delta} = U_{zx}^* \mid_{\bar{x}_{eq}} \xi + U_{zy}^* \mid_{\bar{x}_{eq}} \eta + U_{zz}^* \mid_{\bar{x}_{eq}} \delta$$

where the second-partial derivatives of the pseudo-potential function in the equations above are defined in Eq.(3.5). Note that for every equilibrium point, the z-state component is zero. The

variational equations of motion simplify to:

$$\ddot{\xi} - 2\dot{\eta} = U_{xx}^* \mid_{\bar{x}_{eq}} \xi + U_{xy}^* \mid_{\bar{x}_{eq}} \eta$$

$$\ddot{\eta} + 2\dot{\xi} = U_{yx}^* \mid_{\bar{x}_{eq}} \xi + U_{yy}^* \mid_{\bar{x}_{eq}} \eta \tag{4.13}$$

$$\ddot{\delta} = U_{zz}^* \mid_{\bar{x}_{eq}} \delta$$

The first four eigenvalues are found from the in-plane variational equations. Expressed in matrix form these equations are:

$$\begin{bmatrix} \dot{\xi} \\ \dot{\eta} \\ \ddot{\xi} \\ \ddot{\eta} \end{bmatrix} = \underbrace{\begin{bmatrix} 0 & 0 & 1 & 0 \\ 0 & 0 & 0 & 1 \\ U_{xx}^* \mid_{\bar{x}_{eq}} & U_{xy}^* \mid_{\bar{x}_{eq}} & 0 & 2 \\ U_{yx}^* \mid_{\bar{x}_{eq}} & U_{yy}^* \mid_{\bar{x}_{eq}} & -2 & 0 \end{bmatrix}}_{[A]} \begin{bmatrix} \xi \\ \eta \\ \dot{\xi} \\ \dot{\eta} \end{bmatrix} \tag{4.14}$$

where the dynamics update matrix $[A]$ is similar to the matrix in Eq.(3.3) from the linearization methods of the state transition matrix. The solutions for the in-plane variational equations take the following form[46]:

$$\xi(t) = \sum_{i=1}^{4} A_i e^{\lambda_i t}, \qquad \eta(t) = \sum_{i=1}^{4} B_i e^{\lambda_i t} \tag{4.15}$$

and the eigenvalues λ of the system are found by the characteristic equation:

$$\mid [A] - \lambda[I] \mid = 0 \tag{4.16}$$

Setting $\Lambda = \lambda^2$, four eigenvalues are recovered from the expression above and are:

$$\Lambda = \frac{-4 + U_{xx}^* + U_{yy}^*}{2} \pm \frac{\sqrt{(4 - U_{xx}^* - U_{yy}^*)^2 - 4(U_{xx}^* U_{yy}^* - (U_{xy}^*)^2)}}{2} \tag{4.17}$$

where the second-partial derivatives are evaluated at the respective equilibrium states. The remaining two eigenvalues are found by rearranging the out-of-plane variational equation to yield the following solution:

$$\delta(t) = \sum_{i=1}^{2} D_i e^{\lambda_i t} \tag{4.18}$$

and solving the associated characteristic equation yields the following complex eigen values:

$$\lambda = \pm i \sqrt{\mid U_{zz}^* \mid_{\bar{x}_{eq}} \mid}$$ (4.19)

Stability analysis in the linear system can help provide insight into the stability of these equilibrium points in the nonlinear system. The equilibrium point is unstable in the nonlinear system if any of the eigenvalues have a positive real component. Conversely, asymptotic stability exists if all eigenvalues possess a negative real value. Marginal stability in the linear system is when the real component is equal to zero and the eigenvalues posses imaginary components. In the Earth-Moon system, the co-linear Lagrange points all have unstable eigenvalues in the in-plane modes and thus are inherently unstable points in the system. The linear analysis informs us that motion near the vicinity of these points can naturally approach or depart. L_4 and L_5 have stable and marginally stable modes implying the motion in this region is bounded to a certain degree. These points become unstable for CR3BP dynamical systems with a mass ratio greater than 0.0385208965.

4.3   Periodic Orbits

Orbits that are repeating, as in the initial state is returned to after a period, are of particular interest in the CR3BP due to their predictability in the chaotic system. Such orbits exist around each of the Lagrange points, the celestial bodies, and additional periodic orbits are resonant with respect to the CR3BP system period [12, 46]. For this thesis, periodic orbits are generated and applied to the transfer design problem.

4.3.1   Planar Orbits

Lyapunov periodic orbits are planar and repeating with motion around the co-linear Lagrange points. These solutions can be reasonably approximated using the linearized equations of motion about the equilibrium points in the system. Then, using correction methods the initial guess is computed in the nonlinear dynamical model. We can begin constructing a Lyapunov periodic orbit with the variational equations in Eq.(4.13) where the spatial component is neglected. These

coupled differential equations have particular solutions as shown in Eq.(4.16), and at an initial time of $t = 0$, the particular solution becomes:

$$\lambda_i^2 A_i - 2\lambda_i B_i = U_{xx}^* \mid_{\bar{x}_{eq}} A_i + U_{xy}^* \mid_{\bar{x}_{eq}} B_i$$

$$\lambda_i^2 B_i + 2\lambda_i A_i = U_{yx}^* \mid_{\bar{x}_{eq}} A_i + U_{yy}^* \mid_{\bar{x}_{eq}} B_i$$

(4.20)

for $i = 1, ..., 4$ and $U_{xy}^* \mid_{\bar{x}_{eq}} = U_{yx}^* \mid_{\bar{x}_{eq}} = 0$ evaluated at the co-linear Lagrange points. Let's define the constant α which is equal to:

$$\alpha_i = \frac{(\lambda_i^2 - U_{xx}^* \mid_{\bar{x}_{eq}})}{2\lambda_i}$$

(4.21)

so that a relation between B_i and A_i is established as: $B_i = \alpha_i A_i$. This expression is plugged back into the planar variation equations of motion. From inspection it's seen that $\lambda_1 = -\lambda_2$ and $\lambda_3 = -\lambda_4$. Therefore, $\alpha_1 = -\alpha_2$ and $\alpha_3 = -\alpha_4$. The equations in matrix form with these substitutions become:

$$
\begin{bmatrix} \xi_0 \\ \eta_0 \\ \dot{\xi}_0 \\ \dot{\eta}_0 \end{bmatrix} = \begin{bmatrix} 1 & 1 & 1 & 1 \\ \lambda_1 & -\lambda_1 & \lambda_3 & -\lambda_3 \\ \alpha_1 & -\alpha_1 & \alpha_3 & -\alpha_3 \\ \alpha_1\lambda_1 & \alpha_1\lambda_1 & \alpha_3\lambda_3 & \alpha_3\lambda_3 \end{bmatrix} \begin{bmatrix} A_1 \\ A_2 \\ A_3 \\ A_4 \end{bmatrix}
$$

(4.22)

Constants A_1 to A_4 are solved at the initial time[46]:

$$A_1 = \frac{1}{\lambda_1^2 - \lambda_3^2} \left(-\xi_0\alpha_3\lambda_3 - \dot{\xi}_0\alpha_3\sigma + \eta_0\lambda_3\sigma + \dot{\eta}_0 \right)$$

$$A_2 = \frac{1}{\lambda_1^2 - \lambda_3^2} \left(-\xi_0\alpha_3\lambda_3 + \dot{\xi}_0\alpha_3\sigma - \eta_0\lambda_3\sigma + \dot{\eta}_0 \right)$$

$$A_3 = \frac{1}{\lambda_1^2 - \lambda_3^2} \left(\xi_0\alpha_1\lambda_1 + \dot{\xi}_0\alpha_1\sigma - \eta_0\lambda_1\sigma - \dot{\eta}_0 \right)$$

$$A_4 = \frac{1}{\lambda_1^2 - \lambda_3^2} \left(\xi_0\alpha_1\lambda_1 - \dot{\xi}_0\alpha_1\sigma + \eta_0\lambda_1\sigma - \dot{\eta}_0 \right)$$

(4.23)

where $\sigma = \sqrt{\frac{U_{yy}^* \mid_{\bar{x}_{eq}}}{U_{xx}^* \mid_{\bar{x}_{eq}}}}$. Solutions with the real eigenvalues are omitted as this corresponds to unstable modes. This simplifies equations of motion as $A_1 = A_2 = 0$. The oscillatory modes can now be

excited to find the periodic planar initial state. The linearized equations of motion become:

$$\xi(t) = A_3 e^{\lambda_3 t} + A_4 e^{-\lambda_3 t}$$

$$\eta(t) = \alpha_3 A_3 e^{\lambda_3 t} - \alpha_3 A_4 e^{-\lambda_3 t}$$

$$\dot{\xi}(t) = \lambda_3 A_3 e^{\lambda_3 t} - \lambda_3 A_4 e^{-\lambda_3 t}$$

$$\dot{\eta}(t) = \alpha_3 \lambda_3 A_3 e^{\lambda_3 t} + \alpha_3 \lambda_3 A_4 e^{-\lambda_3 t}$$

(4.24)

At the initial time, for a selected ξ_0 and η_0 the associated velocity components complete the initial state as:

$$\dot{\xi}_0 = \frac{\eta_0 \lambda_3}{\alpha_3} \qquad \dot{\eta}_0 = \lambda_3 \alpha_3 \xi_0$$

(4.25)

For the co-linear Lyapunov solutions, each periodic orbit crosses the x-axis with a zero x-velocity component. Therefore, the solution space is further reduced to only be dependent on ξ_0. The linearized initial guess can now be corrected using either the single or multiple shooting schemes.

A family of Lyapunov periodic orbits are generated using the continuation methods from the previous chapter. Figure 4.2 visualizes a set of L_1 Lyapunov periodic orbits and are colored by each orbit's Jacobi constant. Apart from Lyapunov periodic orbits, other planar cases about the Lagrange points in the CR3BP include short and long period orbits about L_4 and L_5. Additionally, examples of planar periodic families around the secondary celestial body include but are not limited to distant prograde (DPO) and retrograde (DRO) families.

4.3.2   Spatial Orbits

The CR3BP admits various families of spatial periodic orbits about Lagrange points including: halo[18], axial, vertical, butterfly, and dragonfly orbits[43]. For this research, the halo cases about L_1 and L_2 are used. From Doedel et. al. in [12] it is seen that different periodic orbit families is found from each other by studying bifurcation points in the stability. Conversely, methods to approximate halo periodic orbits are given by Richardson[43] which are sufficient initial guesses for the corrections process. For L_1 and L_2, halo periodic orbits can be mirrored about the x/y-plane. This yields distinct northern and southern families of solutions. Figure 4.3 contains a subset of the
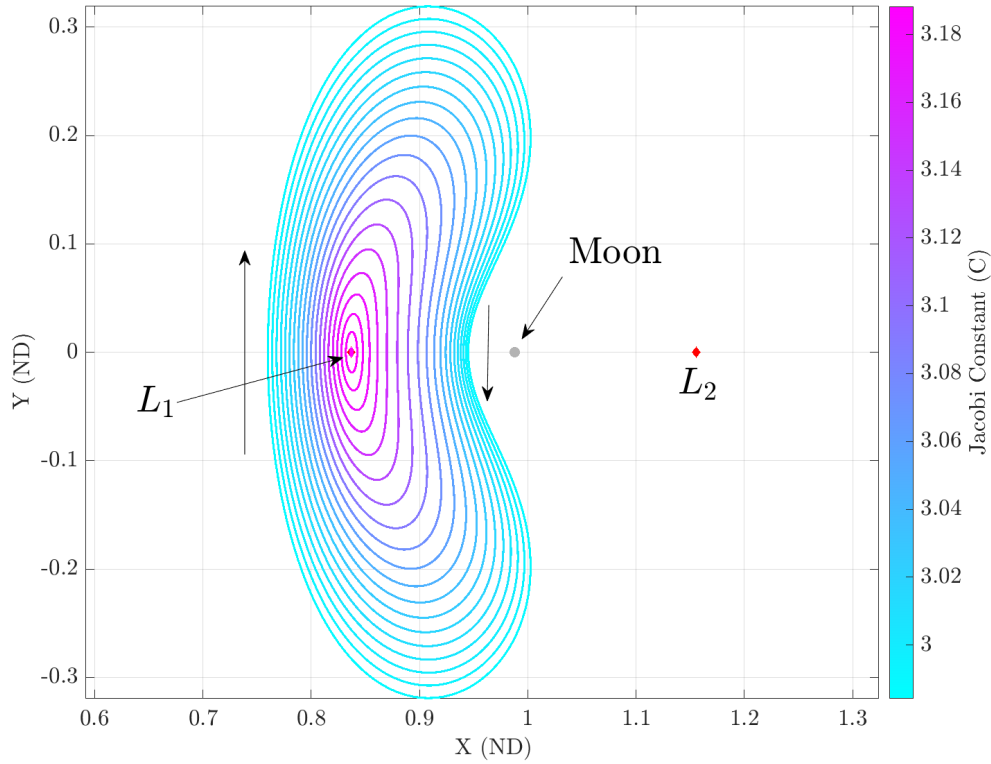
Figure 4.2: L_1 Lyapunov periodic orbit family colored by Jacobi Constant

L_2 southern halo orbits colored by the orbit's Jacobi constant. In the vicinity of the L_2 point, the periodic orbits approach a planar solution which approaches the bifurcation point of the Lyapunov and halo families. Closer to the Moon, the halo family becomes increasingly rectilinear and has close perilunes. These orbits are often referred to as Near Rectilinear Halo Orbits (NRHOs)[18]. Specific orbits in this subset have period resonant ratios with respect to the Moon's orbit and are of particular interest for mission designs.

4.3.3   Resonant Orbits

A resonant relationship exists when the period of the orbit is an integer multiple of another orbit[50]. Conventionally, resonant orbits are denoted by a $n : m$ resonance where n is the tra-
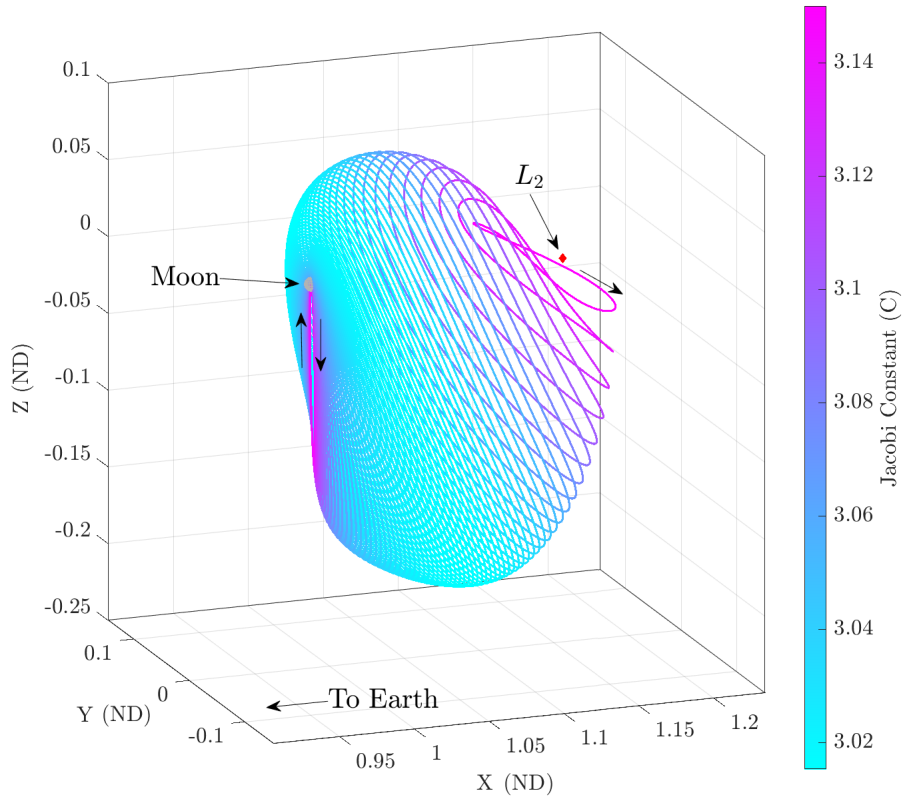
Figure 4.3: L_2 Southern Halo periodic orbit family colored by Jacobi Constant

jectory's integer multiple of the period that equals the system's integer multiple m. For example, a $3:1$ resonance corresponds to when the spacecraft completes three revolutions in the time the system completes a single revolution.

For this investigation, we consider generating planar-periodic orbits that have a resonant relationship with the Earth-Moon CR3BP. We can use insights from the two-body problem, which produces closed-form solutions, to generate initial guess states for resonant orbits in the CR3BP. The solution procedure is as follows: 1) construct the desired $n:m$ resonant orbit in the two-body problem with respect to the orbital motion of the Moon about the Earth-Moon system barycenter, 2) adjust this state for a good initial guess in the CR3BP, 3) utilize corrections schemes to find a resonant solution in the CR3BP, and finally 4) employ continuation methods to find additional

members of the family.

In this thesis, the $1:2$ and $2:3$ resonant planar-periodic orbits are used as an intermediate guess orbit to find a transfer. The $1:2$ family initial guess process is shown here. The associated two-body equations for designing a resonant orbit are:

$$T = 2\pi\sqrt{\frac{a^3}{\mu_{TBP}}}, \qquad v = \sqrt{2\mu_{TBP}(\frac{1}{r} - \frac{1}{2a})} \qquad (4.26)$$

where μ_{TBP} is the two-body gravitational parameter (not to be mistaken with the CR3BP system mass ratio), T is the orbit period, a is the semi-major axis, and r is the radius from the barycenter. Using the l^* of the Earth-Moon as the semi-major axis, yields the lunar circular period, and this is used to find the resonant orbit's period as: $T_r = 2T_{Moon}$. With the two-body orbit period and an arbitrary offset distance r along the x-axis, the two-body initial state is computed. Figure 4.4 visualizes this process for a offset distance $r = 11500 \ km$ from the Moon's semi-major axis. The offset distance is selected as many potential resonant orbits exist. Selecting a value too close to the Lunar circular orbit could yield in increased sensitivities when trying to recover the solution in the CR3BP. Table 4.2 summarizes the initial guess states and orbit periods used to find the first $1:2$ resonant periodic orbit. An intermediate step to adjust the two-body trajectory initial conditions may be required to form a sufficient initial guess for the multiple-shooting scheme in the CR3BP. In this particular case, the orbit period and y-velocity component were modified. A multiple shooting scheme of 25 segments was constructed along the trajectory and after 9 iterations converged on the state from the table. Now that a single resonant periodic orbit has been found, the family of

	Two-Body Trajectory	Adjusted Initial Guess	Recovered Solution
x	0.970083246618106	0.970083246618106	0.977798491207561
y	0	0	0
z	0	0	0
$\dot{x}$	0	0	0
$\dot{y}$	1.18925270508221	1.19425270508221	1.57176545748565
$\dot{z}$	0	0	0
T	12.6434178287077	10.4434178287077	10.4441974060514

Table 4.2: 1:2 Resonant Periodic Orbit Initial Solution. All units are nondimensional
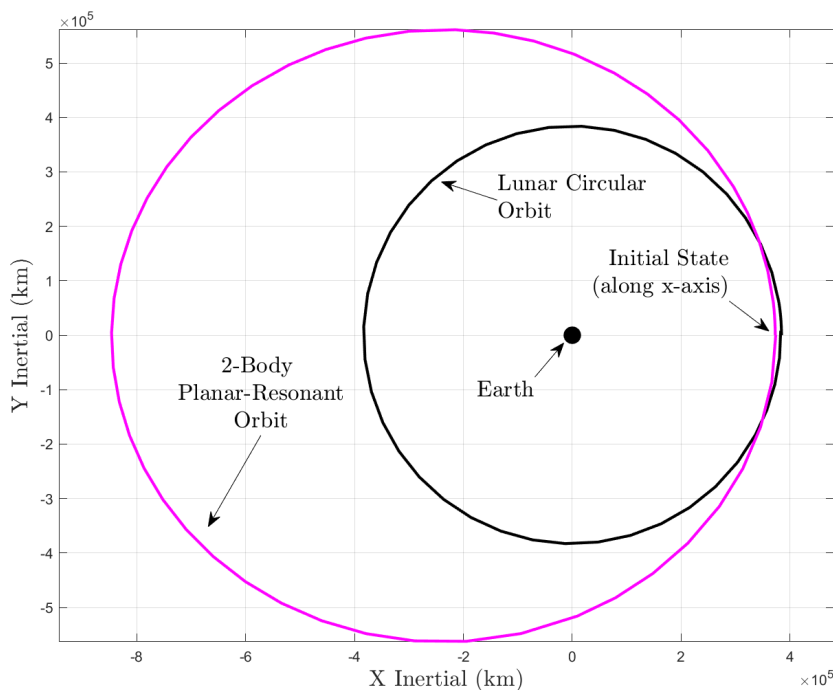
Figure 4.4: Initial 2-Body 1:2 resonant orbit in the inertial frame

solutions is found using either the natural parameter or the pseudo-arc length continuation methods discussed in the previous section. Because the orbits are co-planar with the primaries and cross the x-axis with a zero x-velocity component, the natural parameter continuation scheme was employed by varying the x-coordinate between solutions. Figure 4.5 shows the 1 : 2 resonant periodic orbit family, where the trajectory color indicates the periodic orbit's Jacobi constant. The bottom sub-figure shows the trajectories in the close vicinity of the Moon and their relation to the system's Lagrange points.

4.4   Invariant Manifolds

Sets of trajectories that are unchanging in the dynamical system are said to be invariant, and these particular structures can emanate from periodic orbits and Lagrange points. These manifolds
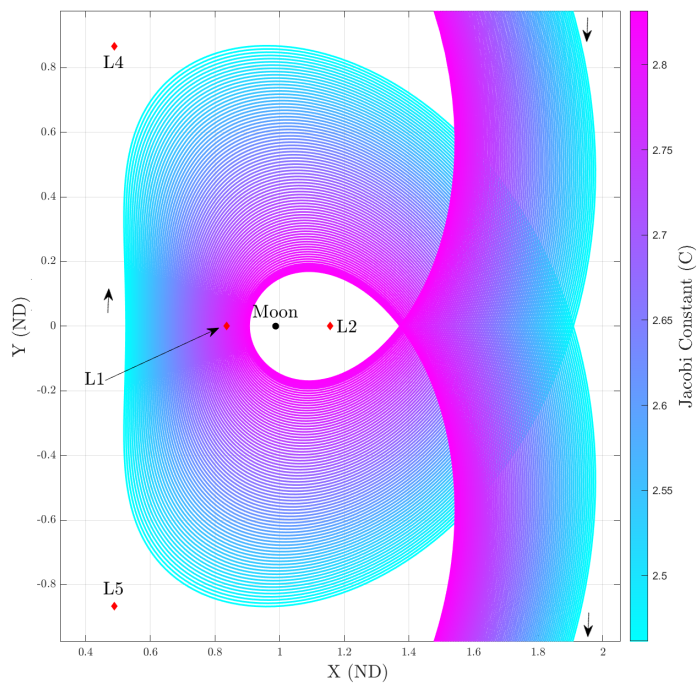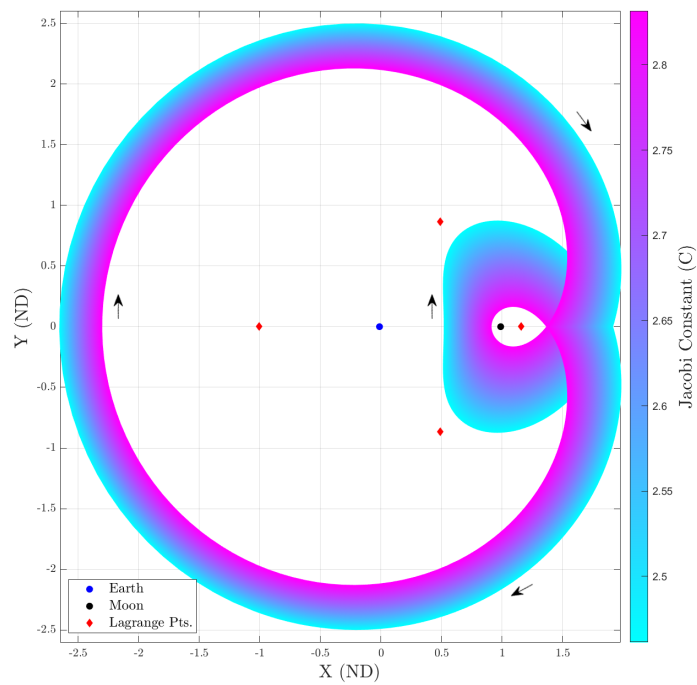
Figure 4.5: 1:2 resonant periodic orbits in the Earth-Moon CR3BP in the rotating frame where the bottom subfigure is a zoomed in view near the Moon

govern natural transport making them useful in the transfer design process[23, 15]. A particle traveling along a manifold is said to asymptotically approach the periodic orbit or Lagrange point in forwards or backwards time. Manifolds are constructed at an unstable state along a periodic orbit $\vec{x}_{PO}$ by perturbing it by the eigenvectors of the monodromy matrix at that particular state. Two stable (left) and unstable (right) manifold initial conditions exist for a given state along a periodic orbit[4]:

$$\vec{x}^S = \vec{x}_{PO} \pm \epsilon \vec{v}^S(\vec{x}_{PO}) \qquad \vec{x}^U = \vec{x}_{PO} \pm \epsilon \vec{v}^U(\vec{x}_{PO}) \tag{4.27}$$

where superscripts S and U correspond to stable and unstable, vector $\vec{v}$ is the associated eigenvector, and ϵ is a scaling constant. The stable manifold state is propagated backwards in time as this manifold approaches the periodic orbit. Conversely, the unstable manifold departs the periodic orbit and so the state is propagated forwards in time. Manifolds for periodic orbits are generated by sampling an arbitrary number of points along the trajectory and generating stable and unstable manifold conditions. If the periodic orbit's monodromy matrix has been computed, it is used to propagate the eigenvectors for these points by:

$$\vec{v}^{S,U}(t) = \Phi(t, t_0) \vec{v}^{S,U}(t_0) \tag{4.28}$$

Figure 4.6 visualizes the manifolds created from 50 points along an example L_1 northern halo periodic orbit. When designing transfers between periodic orbits, it's beneficial to map out the possible trajectories to depart and arrive along manifolds. For example, when transferring between an L_1 northern halo to a L_2 southern halo periodic orbit, a useful first step is to assess the unstable departing geometry of the manifolds to see if close intersections exist with arriving stable manifolds. In some cases, heteroclinic connections may exist where the departing and arriving manifolds are identical, thus offering a theoretically-free transfer between periodic orbits. The full search space is in seven-dimensions, six spatial terms and one integration time term, which can be difficult to properly categorize to find potential initial guess paths.
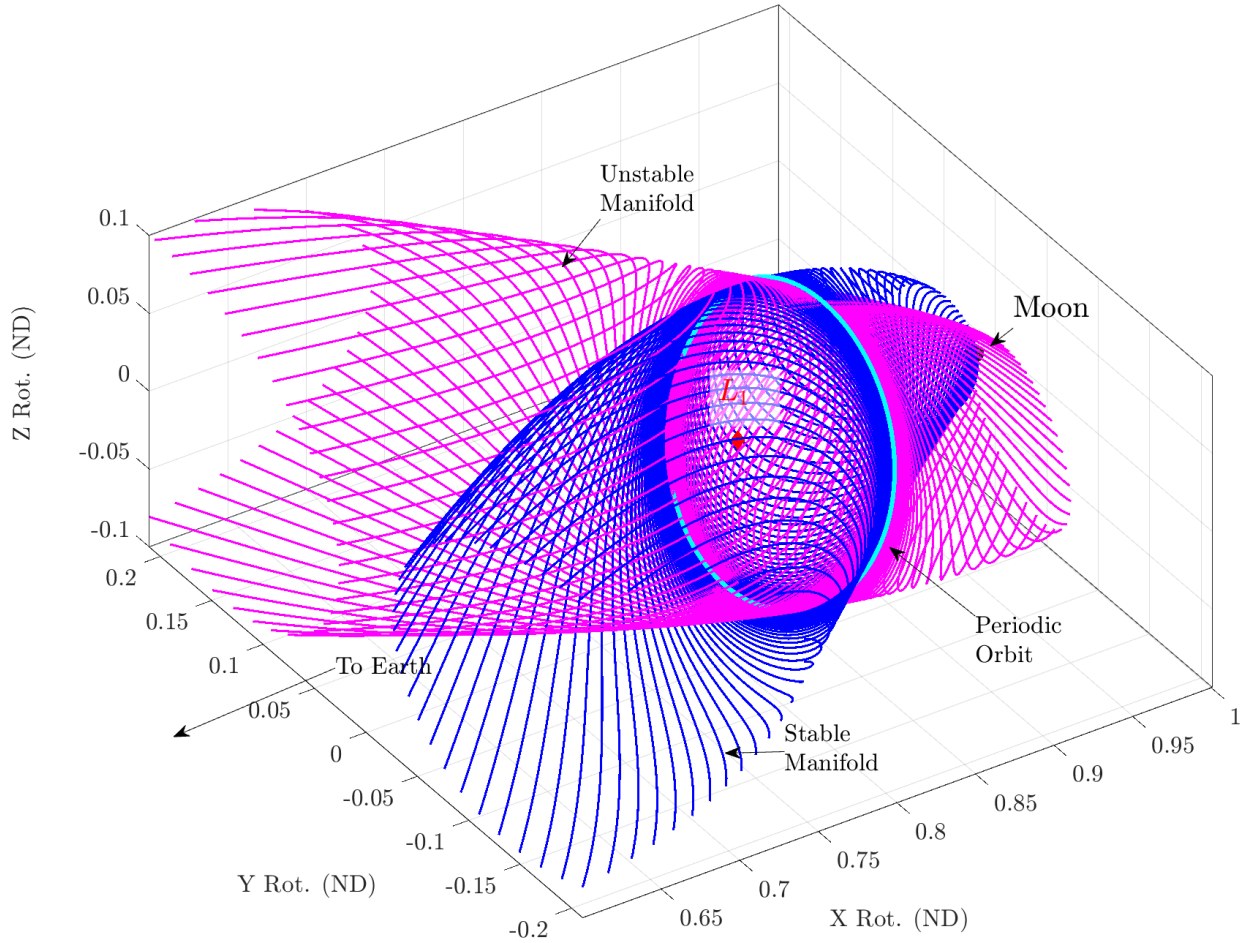
Figure 4.6: Stable and unstable manifolds emanating from a L_1 northern halo periodic orbit

4.5   Poincaré Mapping

A Poincaré map visualizes a reduced number of degrees of freedom of the dynamical system, thus making analysis of particular solutions more intuitive[4, 17, 49]. This is done by creating a surface of section in the phase space, denoted by Σ in Figure 4.7 such that the dynamical system's flow $\phi(\vec{x}_i, t)$ is transverse. Subsequent crossings of this hyperplane are recorded with a numerical superscript indicating the order of crossing. Note that in example figure, crossings of a particular direction are mapped and so the hyperplane is a one-sided map. Poincaré maps offer insights into the flow of the system. For example, if a periodic orbit is mapped, all crossings of the plane occur at exactly the same point. We can assess the stability of the periodic orbit by studying
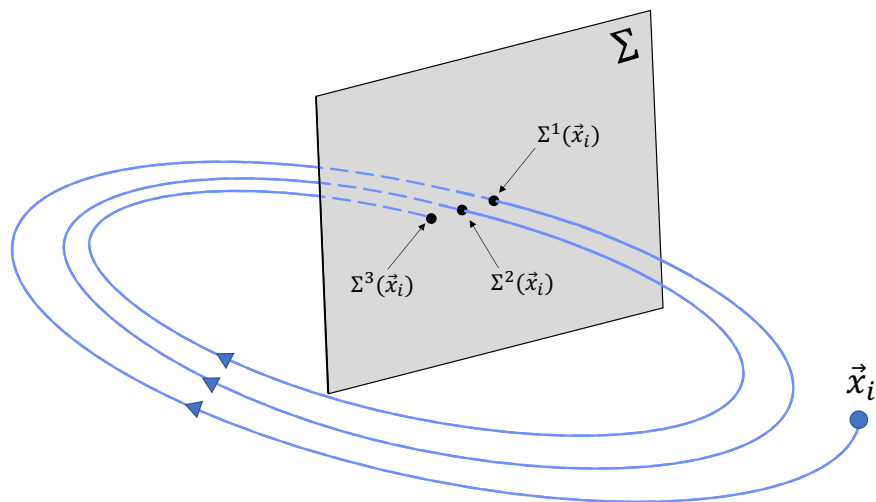
Figure 4.7: Schematic of a Poincaré Section with three transverse crossings from initial state $\vec{x}_i$.

the behavior of perturbed initial conditions about the state mapped onto the same hyperplane. Structures resembling closed curves on the map centered around periodic orbit stationary points are indicative of quasi-periodic behavior on an appropriately constructed map - where the flow is bounded but not necessarily repeating to the same crossings states[4]. Departing or arriving manifolds may also form a curve-like shape on the hyperplane depending on the number of points defining the manifold and the integration time. Plotting departing and arriving manifold crossings on a single Poincaré map is beneficial in finding potential transfers. By finding the closest candidates in the phase space, the required cost to transfer from one periodic orbit to another is significantly reduced and a good initial guess for transfer design is found.

Chapter 5

Transfer Design Process

Differential correction schemes and local optimization routines both require an initial guess for state, time, and control histories such that feasible and optimal solutions are found. The quality of these initial guesses are critical as they directly impact the ability of such methods to recover a solution. This chapter presents methods to utilize known solutions in the CR3BP to form this initial guess before the corrections process. Then methods of continuity are discussed to step feasible initial guesses towards representative transfers of interest. Finally transfers are optimized to save propellant using a variety of methods, and in this research, the direct method of optimization is considered.

5.1 Initial Guess Generation

Generating an initial guess path poses a significant challenge for transfer design. However, certain strategies exist to leverage known solutions in the problem to find potential transfers. We begin by analyzing unstable periodic orbits and their departing and arriving manifolds to form connections. This is dependent on the fact that such connections have sufficiently low state discontinuities such that spacecraft control is utilized to minimize discontinuous path constraints. The assumption that periodic orbit manifolds exist and will approach each other in phase space is inherently limiting and so an additional method of connecting arcs is discussed. It allows for intermediate solutions such as other periodic orbits in the system to form the path connecting the departure and arrival periodic orbits.

5.1.1 Periodic Orbit Departure and Arrival Manifolds

The instability of certain periodic orbit families and their associated invariant manifolds is beneficial in designing potential transfers. Barden, Howell, and Lo in [19] demonstrate the use of invariant manifolds and impulsive maneuvers as potential trajectories departing and arriving Lagrange point orbits. Similarly Gómez, et al. in [16] discuss heteroclinic, zero-cost, connections between the unstable L_1 and L_2 Lagrange points. For unstable departing and arriving periodic orbits, this method is beneficial as it utilizes the natural dynamical motion near the periodic orbits to reduce the maneuver cost.

Given two candidate periodic orbits we begin the process of creating the initial guess transfer by generating the unstable departing manifold and the stable arrival manifold of trajectories. Figure 5.1 depicts manifolds emanating from two halo periodic orbits shown in cyan. A 50 trajectory unstable departing manifold from a L_2 southern orbit is in magenta, and a 50 trajectory stable arriving manifold to the L_1 northern halo orbit is shown in blue. It is evident that visual analysis
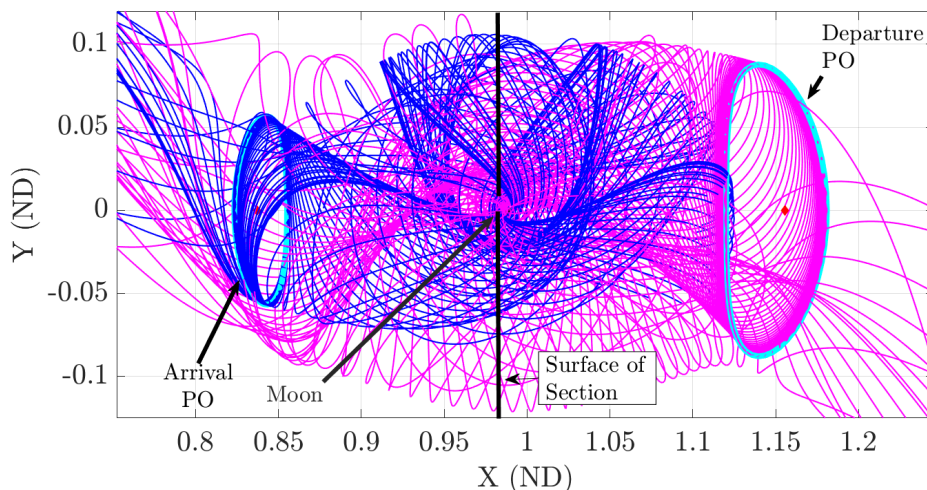
Figure 5.1: L_2 southern halo unstable interior (magenta) and L_1 northern halo stable exterior (blue) manifolds. A Poincaré section at the lunar x-coordinate in the Y/Z-plane can help to find potential transfers.

to find where state discontinuities are minimized is a challenging process. Therefore, we can employ Poincaré maps to reduce the dimensionality of the phase space. In the figure, the solid black line

starting from the lunar x-coordinate is a potential hyperplane of interest, but it is important to note that any section can be taken that yields a convenient analysis point. The left subfigure in Figure 5.2 is a Poincaré map containing each manifold trajectory's y and z-coordinates where the shaded color corresponds to the x velocity component. In the region of interest, both manifolds have minimal discontinuities in their y and z-components. However, note that solutions in this region may not have similar velocity states. Additional Poincaré maps can be generated at the same section but for different variables to understand the phase space of solutions more clearly. From the region of interest, particular departing and arriving manifold trajectories were chosen and they're presented in the right subfigure in Figure 5.2. A potential path with a minimal state
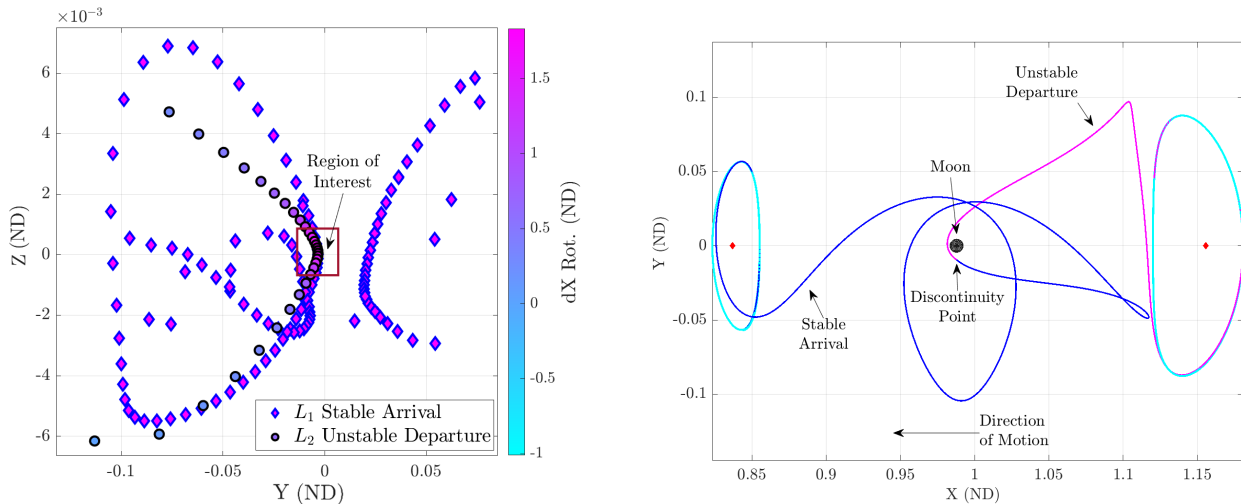
Figure 5.2: Poincaré Map (left) and selected manifolds from region of interest plotted (right).

discontinuity is identified, but a control profile needs to be created to enable corrections methods to recover a fully continuous trajectory. This process is discussed in the corrections subsection of this chapter.

5.1.2 Intermediate Periodic Orbit Arcs

The previous method relies on the assumption that the departing and arriving periodic orbits are unstable with invariant manifolds that have minimized state discontinuities. If this condition cannot be met, an alternative strategy needs to be considered to find potential pathways for the

initial guess. Vaquero and Howell in [47] and [48] leverage resonant periodic orbits to form multi-Lagrange point tour transfers. Pritchett, Zimovan, and Howell in [38] demonstrate this method applied to periodic orbit transfer design. Restrepo and Russell in [41] form a strategy of patched periodic orbits to find suitable transfers by stepping through periodic orbit family solutions. These strategies all leverage existing particular solutions in the CR3BP as intermediate arcs to find potential transfers, and this method is considered in this research.
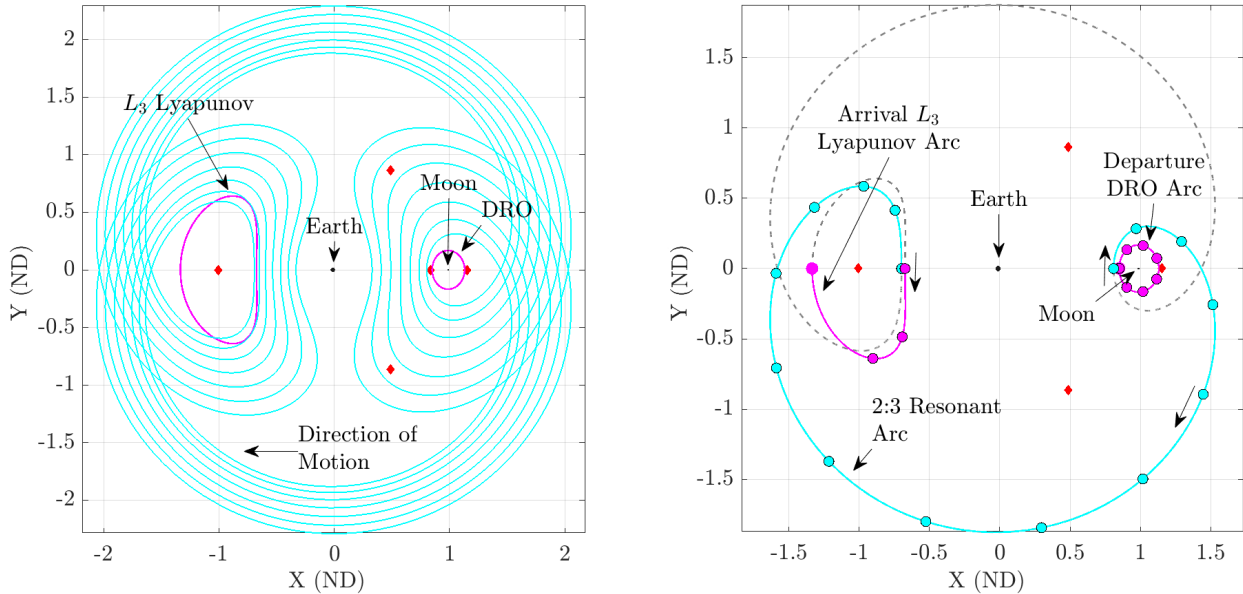
Figure 5.3: Example of a DRO to L_3 Lyapunov transfer using $2 : 3$ resonant periodic orbits. Segments along the initial, final, and any intermediate orbits in the chain is used as initial guess states.

Figure 5.3 demonstrates the use of three arcs to construct an example transfer between a distant retrograde orbit and a L_3 Lyapunov orbit using the intermediate $2 : 3$ resonant periodic orbit family. The left subfigure overlays a set of orbits from the resonant family on top of the initial and final periodic orbits. It is evident that strictly in terms of positional differences, there exists a good candidate resonant periodic orbit that can serve as an intermediate arc for this transfer. A transfer could begin at any state along the DRO and connect to the $2 : 3$ resonant leg. This example includes three-links due to including the departure and arrival periodic orbits themselves as part of the transfer trajectory to improve the guess states. This is shown as scatter points in

magenta and cyan on the right subfigure. The example is one of an arbitrary number of ways to discretize a potential transfer trajectory. In this case, the resonant leg is only used for half of the orbit and is then joined with half of the arrival L_3 Lyapunov orbit. In regards to orbit energy, all three periodic orbits have dissimilar Jacobi constants. The Jacobi constants are 2.96025 for the departure DRO, 2.77439 for the 2 : 3 resonant connecting orbit, and 2.89309 for the arrival L_3 Lyapunov. Variation in the energy can be accommodated for using thrusting segments and this is discussed in the next subsection. For this demonstration, we are able to find a likely transfer by visual inspection of the left subfigure because all orbits in this transfer are planar. For more complex cases with spatial terms, the use of one or multiple Poincaré maps to spot ideal candidate intermediate arcs can be helpful.

Theoretically an infinite number of possibilities for intermediate orbits exist, and an arbitrary number of links can be produced to come up with initial guess paths. While the search for possible paths cannot be done exhaustively, we can inspect other periodic orbit families and their properties to come up with alternate initial guesses.
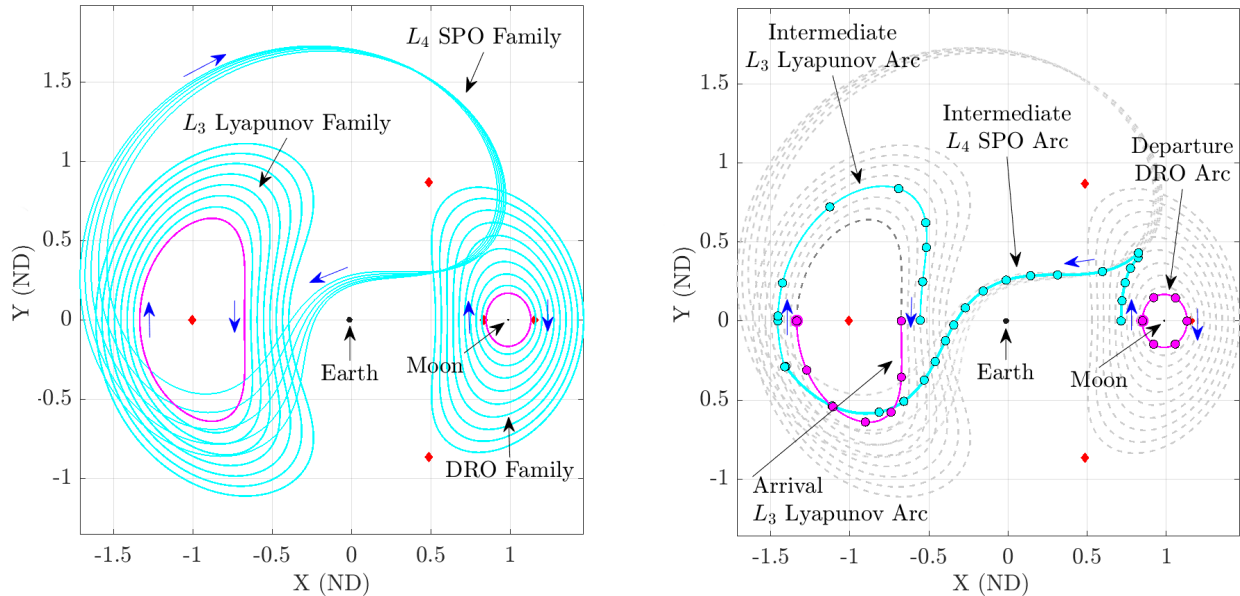
Figure 5.4: Example of a DRO to L_3 Lyapunov transfer using members from the DRO, L_4 SPO, and L_3 Lyapunov periodic orbit families.

For example, the DRO to L_3 Lyapunov transfer could also be solved using a candidate from the L_4 short period (SPO) periodic orbit family[38]. The left subfigure in Figure 5.4 overlays selected members of the DRO, L_4 SPO, and L_3 Lyapunov periodic orbit families in cyan. The magenta orbits are the same initial and terminal periodic orbits from the case in Figure 5.3. The right subfigure in Figure 5.4 demonstrates a potential five intermediate arcs transfer with linear discretization of points along each connecting arc. The initial guess begins along the departure DRO and transfers to a lower Jacobi-constant DRO. Then a connection to the L_4 SPO is intended followed by an intermediate L_3 Lyapunov. Finally the terminal L_3 Lyapunov periodic orbit is queried for states to complete this potential transfer.

5.1.3 Transfer Correction

A feasible transfer is defined as having a continuous trajectory from a starting state to a terminal state along two different periodic orbits. The prior subsections have identified potential paths the spacecraft can take between these orbits, and now discontinuities need to be minimized such that the feasibility condition is met. We begin the process by analyzing where control segments in the trajectory can be included. The initial guess formulation process, discussed by Elliot et al. in [13], sheds some light into strategies for control placement and prioritization of discontinuities. We can utilize the system's dynamical sensitivities our advantage. Take for example a potential transfer that has large energy discontinuities between manifolds, but also has a close perilune. In the vicinity of the celestial body, the sensitivity of the dynamics are increased, and so small changes in the acceleration in this part of the transfer can yield larger changes in energy. This can be exploited to reduce the amount of control effort required by the spacecraft. Conversely, consider a transfer that requires a large plane-change. The reduced sensitivities of the dynamics away from the celestial bodies in the system mean the effect of the spacecraft control in the out-of-plane direction has a greater impact on changing the spacecraft's velocity vector direction. Thus, including thrusting in this direction can potentially change the transfer's inclination for a reduced control effort. In this work, segments for control are placed before and after the intermediate arc

discontinuities. An initial control history is also required for the corrections process. Therefore, we need to initialize some control direction along the transfer. In portions of the initial guess where energy change is required thrusting in or opposite to the velocity direction of the initial guess trajectory is considered. For inclination changes, thrusting in the $\pm Z$-direction is used. In the current problem formulation, the thrust magnitude is assumed to be constant. A unit vector is used to initialize the thrust direction along each control segment to initially satisfy the constraint formulation.
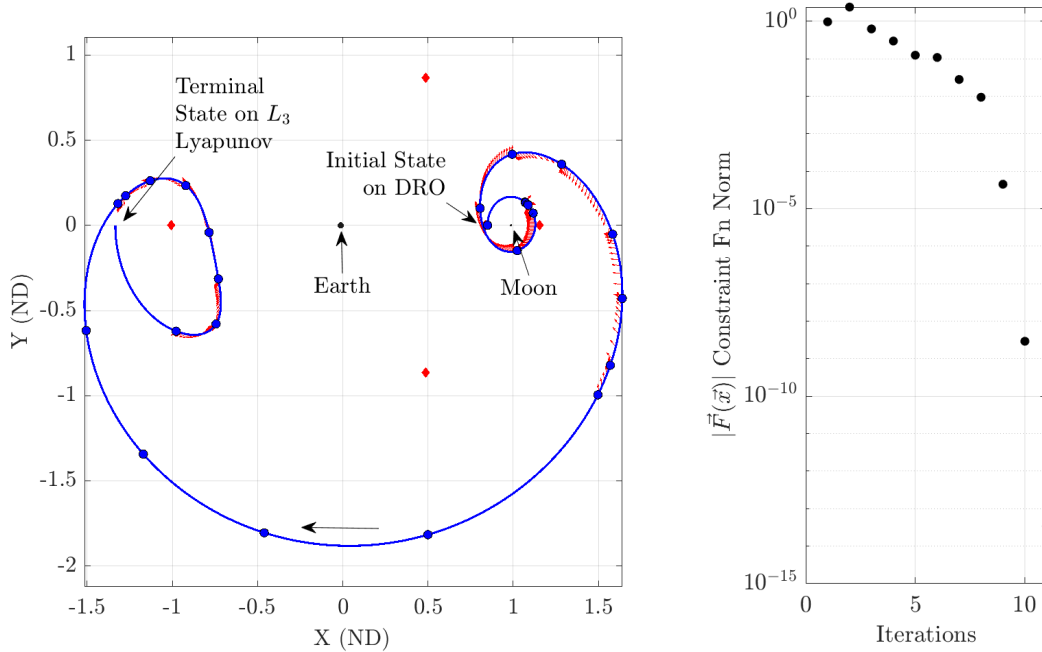
Figure 5.5: Example of a corrected DRO to L_3 Lyapunov transfer initial guess with segments starting states (blue scatter points) and with control (red quivers).

The state and propagation times along each periodic orbit and control vectors for thrusting segments are compiled to form the free-variable vector. This discontinuous path is then corrected using the multiple shooting method. Figure 5.5 demonstrates the transfer corrections process for the example trajectory in Figure 5.3. The constraint function norm versus iterations is shown on the right subfigure. For this example, a spacecraft with an initial mass of 500 kg, maximum thrust of 0.15 N, and an Isp of 2500 s is used. For more complex trajectories, inherently guessing a control

profile can sometimes yield an insufficient initial guess for the iterative Newton's method in the shooting scheme. Reducing the Newton step with the scalar term ρ in Eq.(3.10) can reduce the update magnitude which can increase the likelihood that a possible feasible solution isn't skipped over. Another method to increase the chance of convergence is to reevaluate the discretization of the initial guess arcs. Adding more segments, especially in regions of increased dynamical sensitivity, helps to better approximate the true dynamics with the linearization from the state transition matrix. Adding additional control segments can also help by increasing the acceleration along the trajectory. The ability to find a feasible initial guess is dependent on the path generation process and the discretization of the transfer, and these techniques help to increase the likelihood of recovering solutions for more complicated transfer cases.

5.2   Continuation

We can employ the concept of continuation to explore neighboring solutions with modified constraints or parameters. These quantities include the spacecraft physical parameters or transfers between other periodic orbits in the same families. Spacecraft physical parameters are parametrically searched by varying conditions such as the maximum thrust available, the specific impulse constant, and initial mass. The trajectory's sensitivities to these parameters can then be assessed to find the limitations of a particular transfer initial guess. Figure 5.6 demonstrates spacecraft parameter continuity applied to the DRO to L_3 Lyapunov example cases from Figures 5.3 and Figure 5.4. The spacecraft's thrust available is varied from the initial 0.15 N to 0.05 N by a 0.01 N step using the previously computed transfer as the initial guess for the next trajectory. Blue arcs indicate coasting periods and red arcs indicate when the spacecraft is thrusting. Alternatively, continuation can be applied to walk the initial guess trajectory towards intended mission design parameters. If converging a feasible solution is troublesome, increasing the control acceleration by modifying the spacecraft parameters is beneficial. Once a solution is found, the result can be used to reduce the acceleration back to the intended design parameters through this iterative process.

It should be noted that continuation methods will not always guarantee a solution. The limits
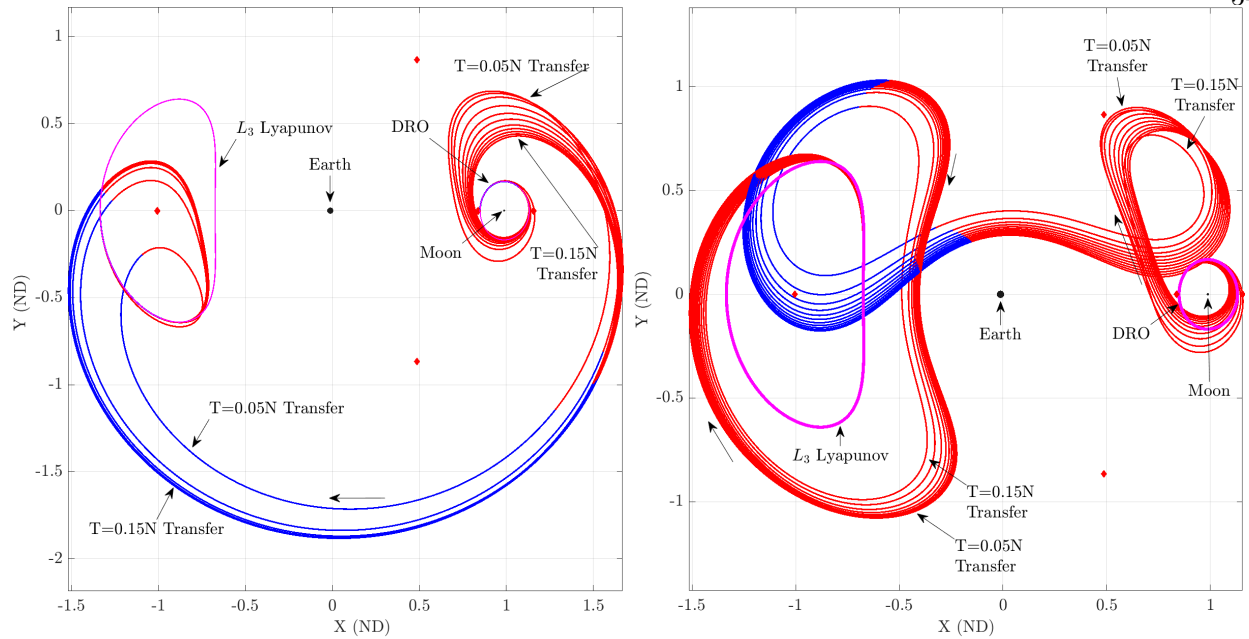
Figure 5.6: Example of solution continuity applied to the DRO to L_3 Lyapunov transfer using both initial guess orbit chain paths. The initial mass and engine Isp are fixed with thrust varied from 0.15N to 0.05N in 0.01N steps.

of the method are discovered when solutions do not converge with smaller continuation step sizes or the update magnitude constant ρ for the corrections process. These parameters are varied in an algorithmic manner to minimum step values before the process is terminated. The continuation algorithm varies the natural parameter by an initial step size. If a solution is not achieved within a specified iteration limit, or there is divergent behavior, then the correction is terminated. The update magnitude is halved and the correction is reattempted. If this does not converge, the natural parameter step is halved and the solution is retried. The algorithm switches between halving the update scalar and parameter step until minimum values for both are reached. Alternatively, step size modulation using the Wolfe conditions mentioned previous can be used here. If either of these processes do not yield a solution, intervention is required to reformulate the initial guess path.

Continuation is also beneficial when finding sets of solutions between periodic orbit families. The initial and terminal states are varied causing a small state discontinuity in the first and last segments along the transfer. The size difference in the previous solution's states and the new

periodic orbit states determine the shooting scheme's ability to recover a solution. This process is done in an iterative manner to generate sets of initial guesses for optimization. It is important to note that the advantage of using solution continuity can also be a limitation under certain circumstances. Consider a scenario applying continuity to a solution to find transfers between two different sets of periodic orbits connected directly by their invariant manifolds. The influence of the first transfer is inherently applied to family of solutions. Suppose a heteroclinic connection exists between one of the pairs of periodic orbits. Theoretically be a minimum control effort solution would be such case. It is not guaranteed that the continuity process would yield such solution as the geometry is evolving from a prior trajectory. However, applying continuity in an automated manner can help to rapidly generate many potential transfer opportunities from a single initial guess construction.

5.3   Trajectory Optimization

The corrections process ensures that a feasible initial guess transfer is achieved. We can take the transfer design process a step further by optimizing the path and control profile such that the minimum amount of propellant is required for the transfer. This in turn increases the payload mass which is beneficial for mission designs. Paths in unpredictable and nonlinear dynamical models can be optimized using Nonlinear Programming (NLP) methods which include indirect and direct problem formulations[31]. Both attempt to optimize some cost function $J(\vec{x})$ subject to equality $\vec{h}(\vec{x}) = \vec{0}$ and inequality $\vec{g}(\vec{x}) \leq \vec{0}$ constraints where $\vec{x}$ is a decision vector.

Indirect methods, also referred to as optimal control, offer a locally optimal solution given a set of extremal conditions[26]. Such methods do not require a discretization of the transfer or an initial guess control. Indirect methods yield continuous trajectories and control profiles. This method reformulates the dynamics such that the optimal control policy's necessary and sufficiency (if available) conditions are incorporated in the system Hamiltonian[26]. The optimal Hamiltonian is one that minimizes the control effort through the propagation. This is found by selecting state and adjoint conditions such that when propagated, the formed two-point boundary value problem

connecting the initial and terminal conditions is satisfied. It is worth noting that this method is inherently more sensitive to the initial guess than direct methods[39]. From [39] the thrust acceleration magnitude of the Hamiltonian is minimized using a "bang-bang" control law that states that the control is always on at full magnitude or off completely. This solution, though difficult to initially converge on, can be achieved by a smoothing function approximating bang-bang control and applying continuation to the desired such control profile[26].

Direct methods evaluate the cost function and a gradient-informed step is taken towards lowering the cost at a particular iteration[31]. The decision vector is varied such that the gradient of the cost with respect to the constraints is zero and non-decreasing in the phase space. This is a necessary condition for optimality which is defined as the Karush-Kuhn-Tucker (KKT) conditions[39]. One such direct method is the interior-point algorithm which is intended to solve non-convex, large decision vector problems using the barrier approach. Sub-problems in each iteration are solved using sequential quadratic programming (SQP) to effectively handle nonlinear constraints. Trust regions are employed for robustness in problem convexity and traversing the constraint gradient[6]. At a high level, the interior-point method approximates the inequality based constrained minimization problem with a series of approximate equality minimization problems. A gradient-step is taken using the trust region method or in some cases a direct Newton step[20]. Derivative information can either be analytically provided if available or computed numerically using finite difference methods. The second-derivative of the constraints with respect to the cost function can also be analytically provided or numerically approximated using the Broyden-Fletcher-Goldfarb-Shanno (BFGS) algorithm[21]. Several nonlinear solver packages are available for direct methods based problems such as: Sparse Nonlinear Optimizer (SNOPT)[36], Interior-Point Optimizer (IPOPT)[54], and FMINCON[21]. This research utilizes the Mathworks MATLAB based FMINCON package, and constrained local optimization using the interior-point method is performed.

The FMINCON solver is initialized by an *optimoptions* MATLAB structure containing properties for the optimization problem setup. The objective and constraint gradients are analytically specified to expedite computation time instead of numerically approximating the Jacobians using

finite difference methods. The Hessian is numerically approximated using the BFGS method. The parallel compute option is enabled which automatically distributes MATLAB processes across multiple cores on the system[21]. Finally, the feasibility and optimality termination conditions are left as their default values of $1e^{-06}$. The feasibility is the maximum constraint violation, where satisfied conditions approach 0 [20]. The optimality criteria is the first-order optimality of the solution which is a measure of the necessary conditions of optimality [6]. The optimization problem is as stated:

$$\min_{\vec{V}}(m_p) \quad \text{s.t.} \quad \vec{F}(\vec{V}) = \vec{\epsilon}, \quad \Delta t_i \geq \Delta t_{min} \tag{5.1}$$

The decision vector passed to the optimization algorithm is the free-variable vector $\vec{V}$ constructed from the feasible initial guess generation process. A constraints function is specified which evaluates the dynamics similarly to the corrections process where $\vec{F}(\vec{V})$ is the nonlinear equality constraints vector and $D\vec{F}(\vec{V})$ is the nonlinear equality constraints gradient. Additionally, nonlinear inequality constraints $\vec{C}(\vec{V})$ and its gradient $D\vec{C}(\vec{V})$ are applied to the problem to restrict the minimum integration time Δt_{min} for each segment i. This condition ensures that segment lengths do not approach zero which can cause instability in the numerical solver. Linear equality or inequality constraints are not considered in this problem setup. The cost $\vec{J}(\vec{V})$ and its gradient $D\vec{J}(\vec{V})$ are specified to FMINCON which sums the total thrust duration along the trajectory and subsequently computes the propellant mass fraction.

For all optimal trajectories generated in this research, the optimizer is allowed to run until the termination feasibility and optimality conditions are satisfied. The computation time is dependent on the size of the decision vector, the initial guess quality, the trajectory's sensitivity, and the computer hardware. Figure 5.7 visualizes optimal trajectories computed for the example case propagated through this chapter. For both cases, the spacecraft has an initial mass of 500 kg, maximum thrust of 0.1 N, and a constant specific impulse of 2500s. The method for optimizing trajectories thus far satisfy the conditions for optimality. However, it is important to note that these trajectories may not represent the true minimum potential cost for the transfer. These
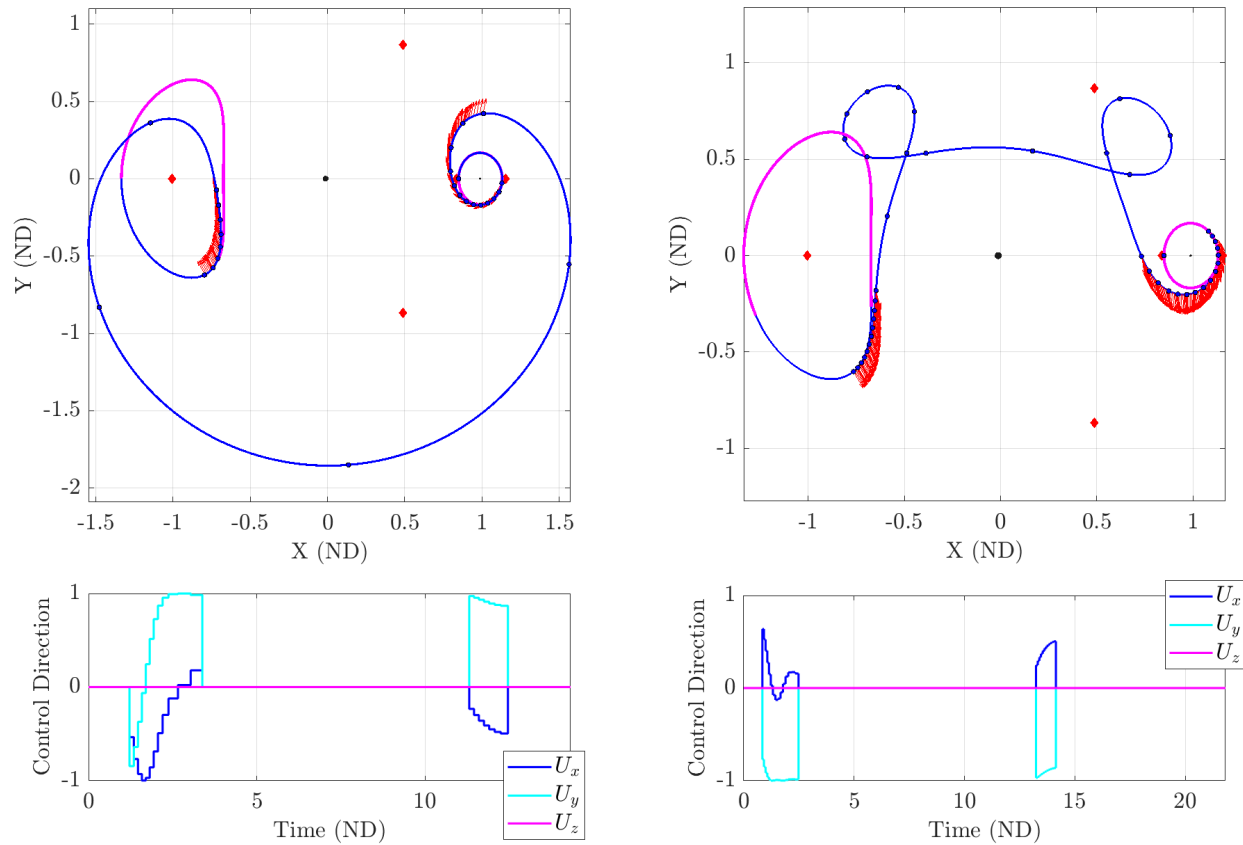
Figure 5.7: Optimized trajectories and control profiles for both initial guesses from the example

solutions are locally optimal solutions by the optimization method, hence why two different initial guess trajectories do not generate the same optimal solution. Davis in [11] discusses considerations of locally optimal solutions such as transfer geometry and time. Theoretically the most optimal solution in terms of minimum propellant expended is when the control effort approaches zero. Consequently this forces the transfer time to approach infinity, and therefore isn't a practical solution for mission designs. Therefore, without explicit constraints on the flight time or initial solution geometry a practical optimal trajectory is difficult to achieve. Additionally, the decision vector size and quality of the initial guess play an important role in the optimizer's ability to recover a solution and the computation time. The trajectory from the left subfigures in Figure 5.7 consists of 26 arc segments and a decision vector size of 291×1. The initial guess solution takes 63.345 days and 12.9781 kg of propellant. The optimal trajectory has a flight time of 62.165 days

and 5.0726 kg of propellant use. The trajectory from the right subfigures have 43 segments and a decision vector of size 465×1. The initial solution's time and cost are 91.078 days and 23.64 kg. The optimized solution is 94.75 days and 3.884 kg of propellant. The former trajectory took 343 seconds to compute whereas the later took 3698 seconds on the same computer system. The optimization flight time and performance will directly vary according to the decision vector size, the descritization of the initial guess path, and how much different the optimal solution is with respect to the initial guess.

Many basins of locally optimal solutions exist in the gradient-space of the problem[29], and as shown from the example transfers created in this chapter, a good initial guess formulation is essential in the low thrust transfer design problem. Additionally, features of the initial guess are to be expected in the post-optimized trajectory due to the locally optimal nature of the recovered solution. In this research, the direct methods is used for its availability of industry standard optimization routines to prototype many locally optimal trajectories in the transfer design problem.

Chapter 6

Applications in the Earth-Moon System

Corrections, continuation, and optimization are applied to compute transfer trajectories between periodic orbits in the Earth-Moon CR3BP. In this chapter, two sets of transfers are presented. The first scenario explores families of trajectories between the L_1 northern halo to the L_2 southern halo periodic orbits using initial guess continuity. The second transfer example is from a L_2 southern NRHO to a DRO which focuses on initial guess generation techniques and comparing different geometries and their associated conditions.

6.1 L_1 Northern to L_2 Southern Halo Transfer

The intent in this first example case is to demonstrate constructing a set of potential transfers between various members in the L_1 and L_2 halo periodic orbit family from a single initial guess. Natural parameter continuation is applied to step through subsets of the families in an automated manner to generate feasible transfers. Then, specific cases are input to the optimization process to minimize spacecraft propellant mass fraction. For this example a spacecraft with an initial mass of 500 kg, maximum thrust of 0.1N, and a constant specific impulse of 2500s is used. A arbitrary subset of 600 trajectories from Jacobi constants 2.998646 to 3.173605 of the L_1 northern family, and 3.027680 to 3.151838 of the L_2 southern family are selected for this transfer problem. Figure 6.1 visualizes these periodic orbits with every 20th pair plotted.
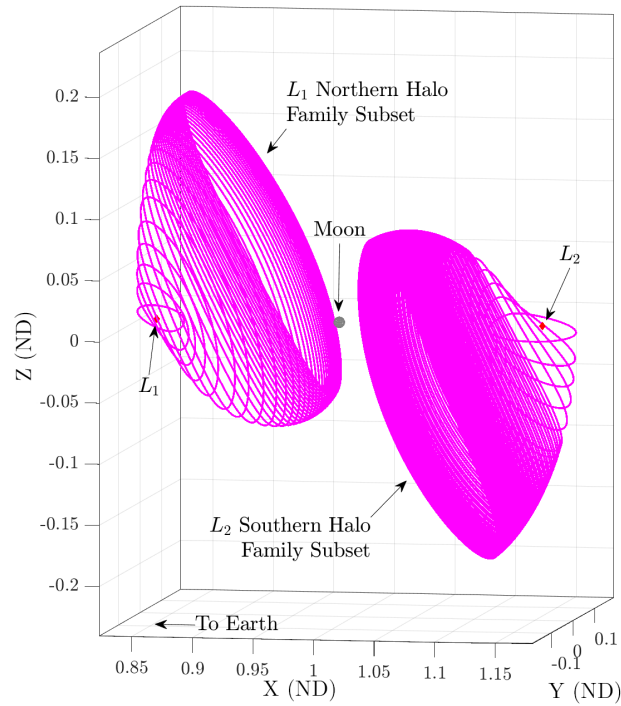
Figure 6.1: L_1 northern and L_2 southern halo periodic orbit family subsets
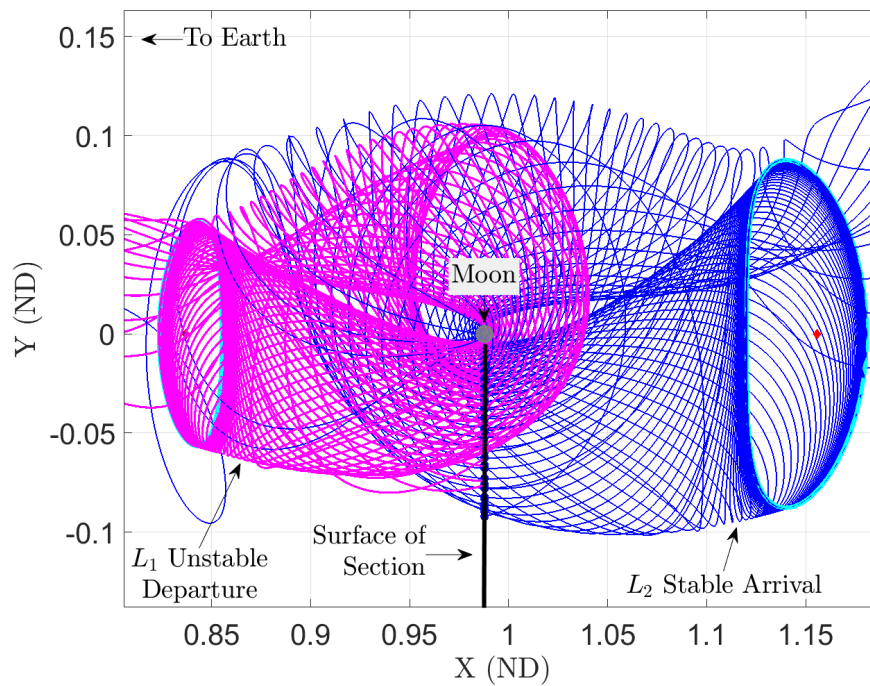
Figure 6.2: L_1 unstable and L_2 stable manifolds for initial L_1 to L_2 halo periodic orbits pair with Jacobi constants 2.998646 and 3.027680

6.1.1 Initial Guess Construction

The transfer design process begins by assessing potential paths the spacecraft can take using the invariant manifolds of the periodic orbits. We will construct a feasible initial guess for the first pair in the set of transfers and then apply continuation. Figure 6.2 visualizes a 50 trajectory manifold for the L_1 halo unstable departure in magenta and the L_2 halo stable arrival manifold in blue. Zero or one-revolutions around the Moon for either of the manifolds is considered, but it should be noted that multiple revolution initial guesses may exhibit better alignment of position and velocity points at the expense of a longer transfer time. A surface of section is considered at the Moon's nondimensional x-component as the manifolds cross this plane to transfer from the L_1 to L_2 vicinity. Note that potentially any surface of section could be selected as long as the hyperplane is transverse to the flow. The selected surface of section will have an influence on the initial guess generated. For this transfer, the lunar x-component was selected. Better alignment of trajectories were noticed for negative y-component crossings, and thus the surface of section was reduced to this region only. Integration of each trajectory is terminated at the surface of section, and trajectories that depart the lunar vicinity are terminated at a fixed time condition and are not considered.

The top subfigure in Figure 6.3 is the Poincaré map generated at the surface of section shown in Figure 6.2. Magenta points indicate the L_1 unstable departure manifold and blue points are the L_2 stable arrival manifold. The position components are shown as scatter points and the states' velocity vectors are drawn as quivers originating from these points. Note that out-of-plane velocities exist in this solution as the transfer is spatial. Also, velocity vector directions do not correspond to the position axes of the plot. The arrow lengths are are proportional to the velocity magnitude. The first pass at the surface of section is noted by a diamond and the second is a circular scatter point. Additionally, the Lunar radius in the Y/Z-plane is shown as a red circle to rule out impact trajectories. Six initial path alignments in the y and z-components with roughly similar velocity directions are shown in the figure. Their locations on the Poincaré map are noted with black
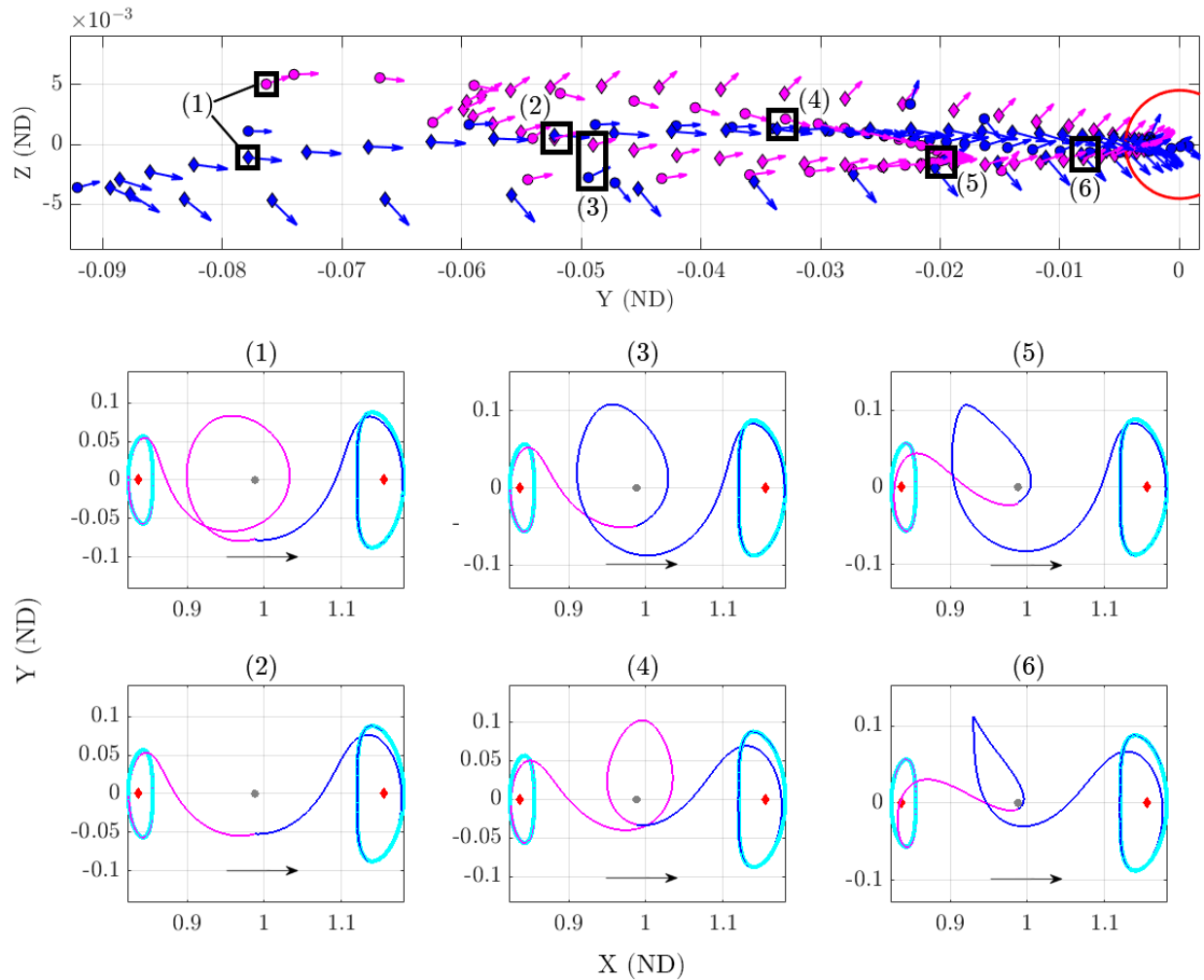
Figure 6.3: Poincaré Map at Surface of Section (top) and selected initial guess trajectories plotted

rectangles and are ordered corresponding to their distance from the Lunar surface. Candidate 1 has the largest position and velocity discontinuity from the set. Candidate 2 is the only zero-revolution trajectory likely making it the fastest in terms of flight time. However, a considerable directional discontinuity in the velocities exist. Candidates 3 and 4 were selected to show the difference in geometry if a zero or one-revolution guess was chosen for either manifold. Finally, candidates 5 and 6 show an evolution of the geometry from candidate 3. As the perilune radii decreased, it was observed that the loop pinches which is indicative of a slower apolune velocity in the loop. Candidate 6 has the smallest discontinuity in position and velocity and so this pair is used to form the initial guess for the transfer. The path is discretized with thrusting arcs at the
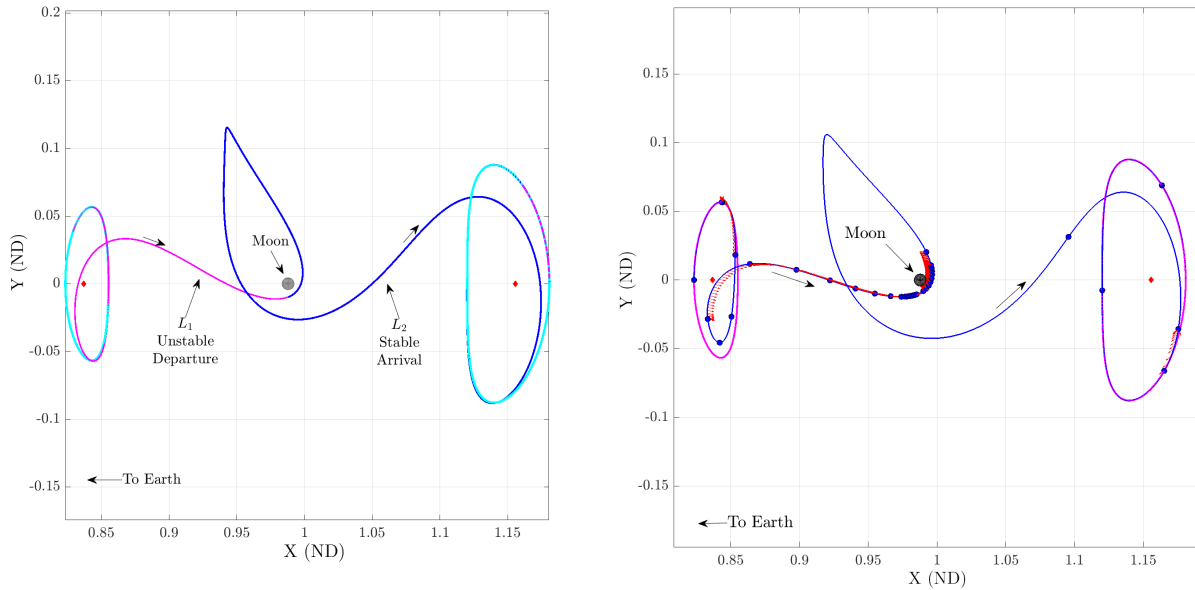
Figure 6.4: Initial guess from invariant manifolds (left), feasible transfer (right)

initial and terminal nodes to facilitate the departure and arrival trajectory from the periodic orbits. Additional control segments are placed at perilune along the end of the departure manifold and beginning of the arrival manifold. The discontinuous initial guess path is shown in the left subfigure in Figure 6.4, and the recovered continuous trajectory is shown on the right subfigure. It is evident that with the spacecraft's acceleration capability, a short thrusting segment at perilune isn't feasible to account for the energy difference at the discontinuity. Therefore, the feasible solution beings thrusting considerably in advance of the perilune encounter. We can optimize this case to yield a trajectory geometry that balances the advantages of a close perilune while considering the limited acceleration capabilities of the spacecraft.

Figure 6.5 contains the locally optimal trajectory for this case followed by the Jacobi constant change and control profile versus time. From this result, it is seen that the one-loop geometry is still retained in the optimized solution, but the perilune and thrusting segment locations are shifted considerably. The propellant mass savings of this solution versus the initial feasible solution is 1.6927 kg from the feasible solution requiring 2.7566 kg to the optimized solution requiring 1.0639 kg of propellant. The transfer time increased to 50.3655 days as opposed to 41.5613 days as a

consequence. The departure and arrival low thrust burns are primarily spatial, and the perilune burn direction evolves over the burn duration. The spatial components can be seen in the top subfigure. It's worth noting that the optimized trajectory is similar to initial guess candidate 3 from the Poincaré map in Figure 6.3. This candidate has predominantly spatial discontinuities, which are accounted for in the optimized solution.
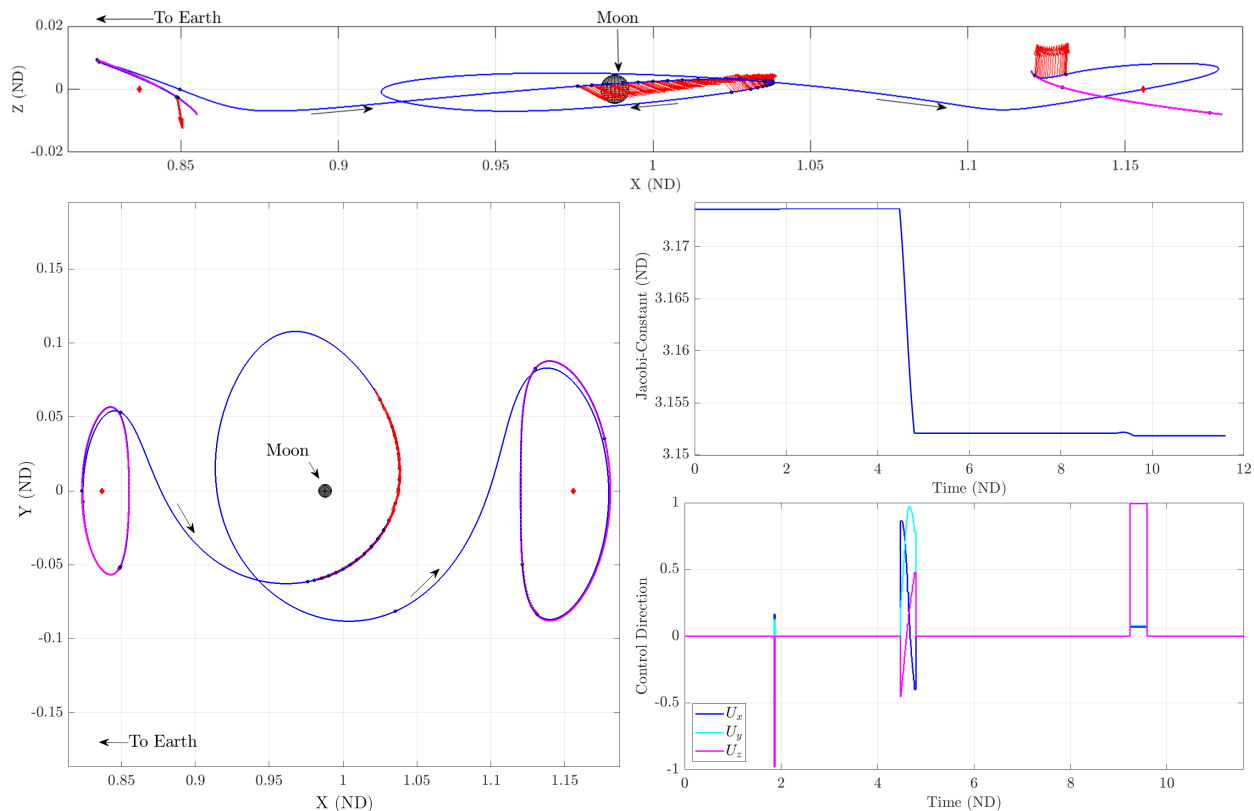
Figure 6.5: Initial transfer optimized transfer path, Jacobi constant, and control profile versus time

6.1.2   Continuation and Transfer Optimization

Now that a single case has been corrected and optimized, we can leverage continuation to find an initial set of feasible transfers. Natural parameter continuation is applied by iteratively modifying the initial and terminal states and using the previous solution as the initial guess path. With this formulation, an initial and terminal discontinuities are corrected using the multiple shooting scheme. It should be noted that using the full update in the shooting scheme may lead to divergent behavior

on certain cases which is indicative of increased sensitivity in the solution geometry. This problem is accounted for by identifying divergent behavior in the corrections process, prematurely terminating it, and retrying with a smaller update scaling factor. Figure 6.6 shows the evolution in the geometry

(a)   (b)
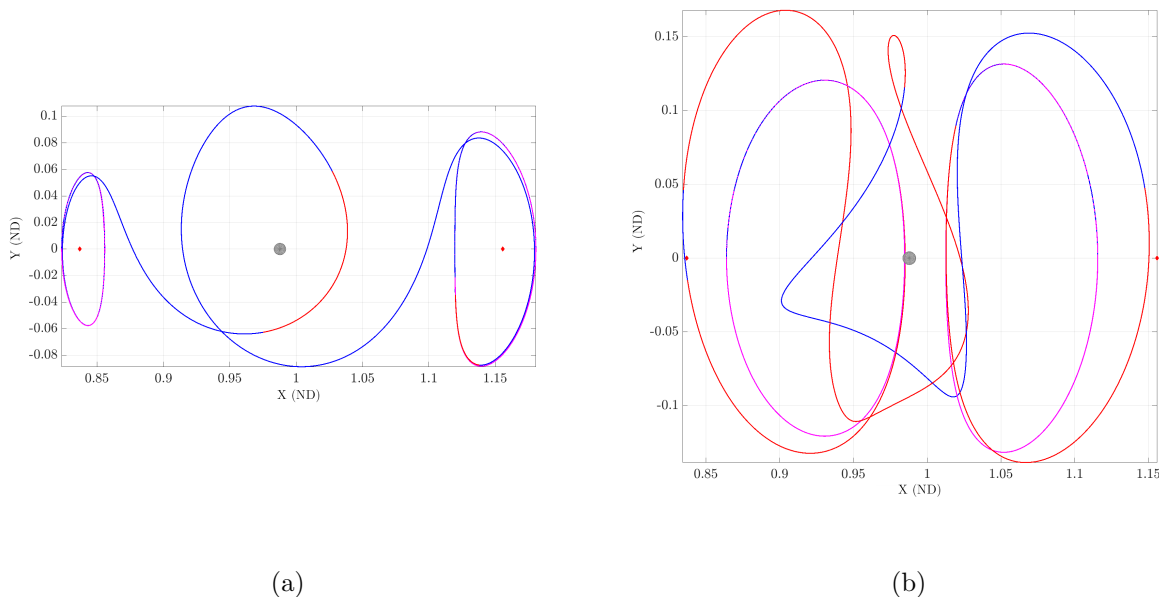
Figure 6.6: Evolution in the transfer geometry for increasingly inclined transfers.

across the initial and terminal transfers in the set. Magenta arcs are the periodic orbits, red arcs indicate thrusting, and blue arcs are coasting. The geometry begins with a revolution around the departing periodic orbit, followed by a loop about the Moon, before a revolution about the arrival periodic orbit. Figure 6.7 shows the set of transfers in a three-view where the moon is centered each of the subfigures.

6.1.3   Improving Transfer Set Using Point Case Optimizations

The existing set can now be updated to reduce the propellant cost. Computing optimal trajectories for the entire family of solutions is a time consuming process using the direct optimization method. Therefore, one or more point cases are optimized, and are then these used as initial guesses for the next pass in continuation to update the set of transfers. By utilizing the optimal transfers

(a) X/Y-plane   (b) X/Z-plane   (c) Y/Z-plane
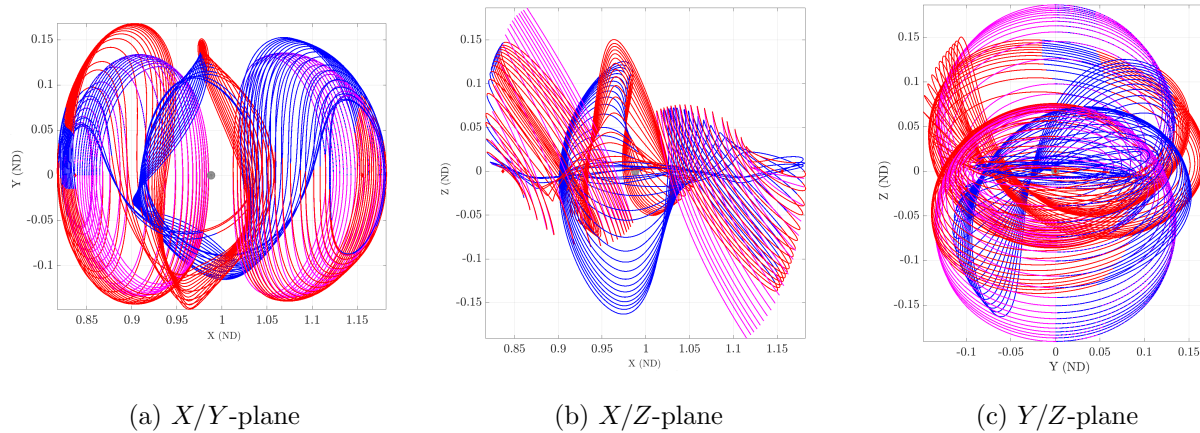
Figure 6.7: Initial set of transfers from the L_1 northern to the L_2 southern halo families

and applying continuation, we can significantly decrease the propellant consumption across the family of solutions, but it should be explicitly stated that only a selected number of locally optimal solutions exist in the set and the rest are feasible solutions with reduced costs.

Four selected optimizations along the family of solutions are shown in Figure 6.8. Subfigure (a) is the first transfer in the family with departing and arriving Jacobi constants of 3.1736 and 3.1518. An initial thrusting is a short duration burn lasting around 2 hours and is mostly in the out-of-plane component to initiate the departure. Unlike the initial guess trajectory, the perilune radius is increased such that the departure and arrival arcs are connected by control segments in the vicinity of the Moon. This maneuver is 35 hours in duration. A final thrusting arc of 39 hours corrects the transfer inclination and energy difference with respect to the arrival periodic orbit. Subfigure (b) connects periodic orbits of Jacobi constants 3.1523 and 3.1384. In this solution, it is seen that a similar single-loop transfer geometry to the existing solution is retained. The departure begins with majority of the thrusting in the out-of-plane component to significantly reduce the inclination and increase the energy to begin the transfer. The subsequent maneuvers are 56 and 220 hours long. A ballistic revolution around the Moon occurs before an out-of-plane, 85 hour low thrust maneuver is performed to rendezvous with the terminal periodic orbit state. In subfigure (c) an evolution in the trajectory geometry is observed which transfers between Jacobi constants
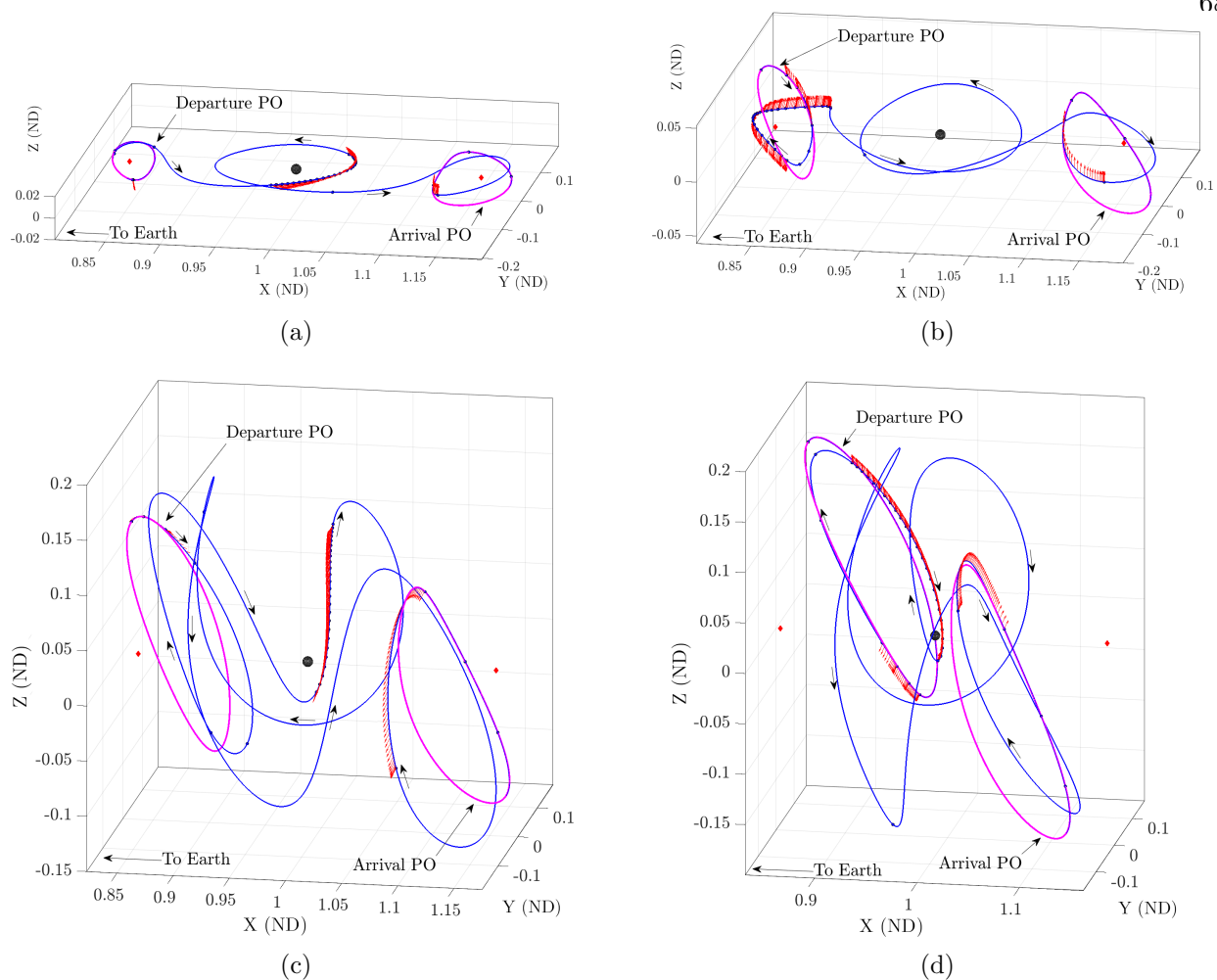
Figure 6.8: Optimized transfers in the set of solutions

3.0791 and 3.1015 which was noted in Figure 6.6. The transfer begins with a roughly 60 hour maneuver to depart the periodic orbit. A subsequent vertical loop reminiscent to the departure periodic orbit occurs which is followed by the closest perilune pass. A 45 hour burn is performed beginning near perilune and the trajectory loops back towards the vicinity of the departure periodic orbit. It crosses the vicinity of the Moon once again before the arrival burn lasting 102 hours is performed to arrive at the periodic orbit. Subfigure (d) is the terminal transfer in the family and has the lowest set of Jacobi constants of 2.9987 and 3.0277. These are the most inclined set of periodic orbits examined, but still retain a similar geometry to the case in subfigure (c). A 21 hour

burn initiates the departure followed by a loop similar to that from the intermediate case. Up to the perilune, the transfer requires a 69 hour burn. The transfer continues out to the L_2 region before returning back to the L_1 vicinity. This is followed up with another loop and a low thrust burn roughly along the arrival periodic orbit of 64 hours to complete the transfer. A summary of the optimization cases according to their label in Figure 6.8 are presented in Table 6.1. As the

		Transfer Time (days)	Final Mass (kg)	Propellant (kg)	Savings (kg)
Case (a)	Feasible	41.5613	497.2434	2.7566	-
	Optimal	50.3655	498.9361	1.0639	1.6927
Case (b)	Feasible	54.4161	491.9583	8.0417	-
	Optimal	53.9179	494.6536	5.3464	2.6953
Case (c)	Feasible	59.0808	489.2310	10.7690	-
	Optimal	58.6704	496.8909	3.1091	7.6599
Case (d)	Feasible	58.9819	488.7287	11.2713	-
	Optimal	56.4502	497.7670	2.2330	9.0383

Table 6.1: Optimized transfer results versus initial solution set

periodic orbit pairs in the family of transfers vary from the initial solution shown in case (a), the post optimized solution propellant savings are greater. This is to be expected as such initial and terminal periodic orbit pairs are significantly different than pairs closer to the where the initial optimal solution was computed.

Figure 6.9 summarizes the transfer sets created between the L_1 northern halo periodic orbit family and the L_2 southern halo periodic orbit family. Select cases are presented in this figure and the Jacobi constants of the departure/arrival pairs are listed on the x-axes. On the y-axis the propellant cost in kilograms is shown. Cyan points indicate the original set, from Figure 6.7, which are generated using the initial optimal solution for continuation. The magenta points are the updated set of feasible transfers that were recomputed from the point case optimizations shown as red scatter points. Continuation is applied starting from the optimal trajectories and extending evenly forwards and backwards in the transfer set. The updated set of solutions have lower propellant requirements due to the intermediate optimal cases providing better initial guesses within the family. It should be noted that only four optimal solutions exist in this data set, and so
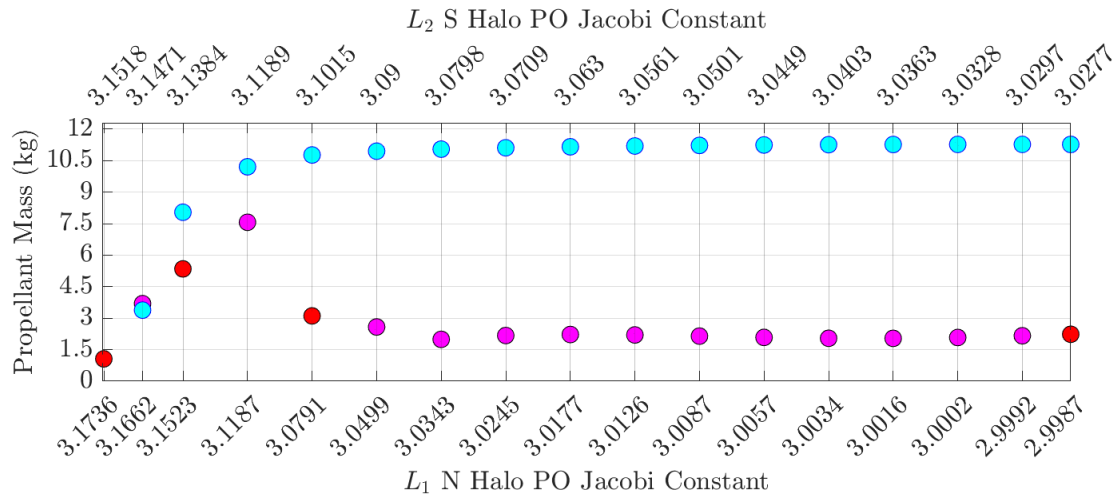
Figure 6.9: Transfer set before (cyan) and after (magenta) applying optimization to selected trajectories (red) and continuation

the improvement in the family of solutions should not be mistaken for a complete set of optimal transfers. This is evident in the third transfer presented in the figure where using the updated data set has a slightly higher cost for the transfer than the original. Additionally, the solutions of both sets are nearly identical in the vicinity of the original seed case as continuity is applied from the same case. Figure 6.10 is a three-view of the updated set. When comparing the family of

(a) X/Y-plane

(b) X/Z-plane

(c) Y/Z-plane
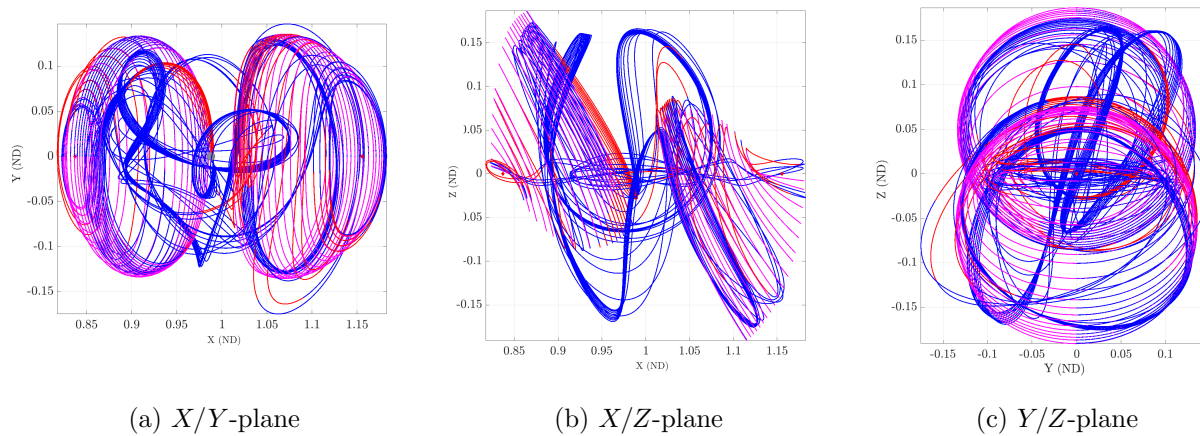
Figure 6.10: Updated set of transfers

solutions here with the original feasible set in Figure 6.7, it is evident that the geometry of these

transfers is considerably modified, but there are resembling features of the initial feasible solution in the updated set. Trajectories in the updated set depart the L_1 vicinity with a loop, followed by a close pass to the Moon. The trajectories continue to the L_2 region before returning back to the L_1 vicinity. Finally, the trajectories cross the Moon and then rendezvous with the terminal state along the arrival periodic orbits. Though, the orientation of the loops, perilune radii, and thrusting locations are significantly different than the original set of transfers.

This example demonstrates the ability to prototype sets of transfers between periodic orbits by first constructing a single transfer using the unstable departing and stable arriving manifolds. Then, this case is optimized, and continuation is used to generate an initial set of transfers. Select cases from the set are optimized where the the geometry evolution is most apparent. Then continuation was applied from these solutions to update the set to reduce the transfer propellant cost across the entire set of transfers.

6.2   NRHO to DRO Transfer

With the increased focus on returning humans to the Lunar surface, multiple spacecraft mission concepts are actively being studied to facilitate this goal. The Deep Space Gateway (DSG) is one of such spacecraft and theoretically will be able to sustain long term operations in a continuous Lunar orbit. The DSG is intended to leverage the stability of a particular subset of halo periodic orbits called the Near Rectilinear Halo Orbits (NRHO)[52] for reduced station keeping costs[9]. Disposal mission concepts for DSG, large science spacecraft, or limited propulsion bodies such as sample asteroids are being studied[25]. The Distant Retrograde Orbit (DRO) family offers long term stability which can help facilitate such missions. Capdevila and Howell in [7], Oshima in [33], and Wang et al. in [51] consider the NRHO to DRO transfer design problem using the CR3BP dynamical model. Additionally, McGuire et al. in [30] and McCarty et al. in [28] explore a similar NRHO to DRO transfer for large spacecraft structures similar in size and capability to DSG. For this example case, the L_2 southern NRHO and the DRO are considered from [7].
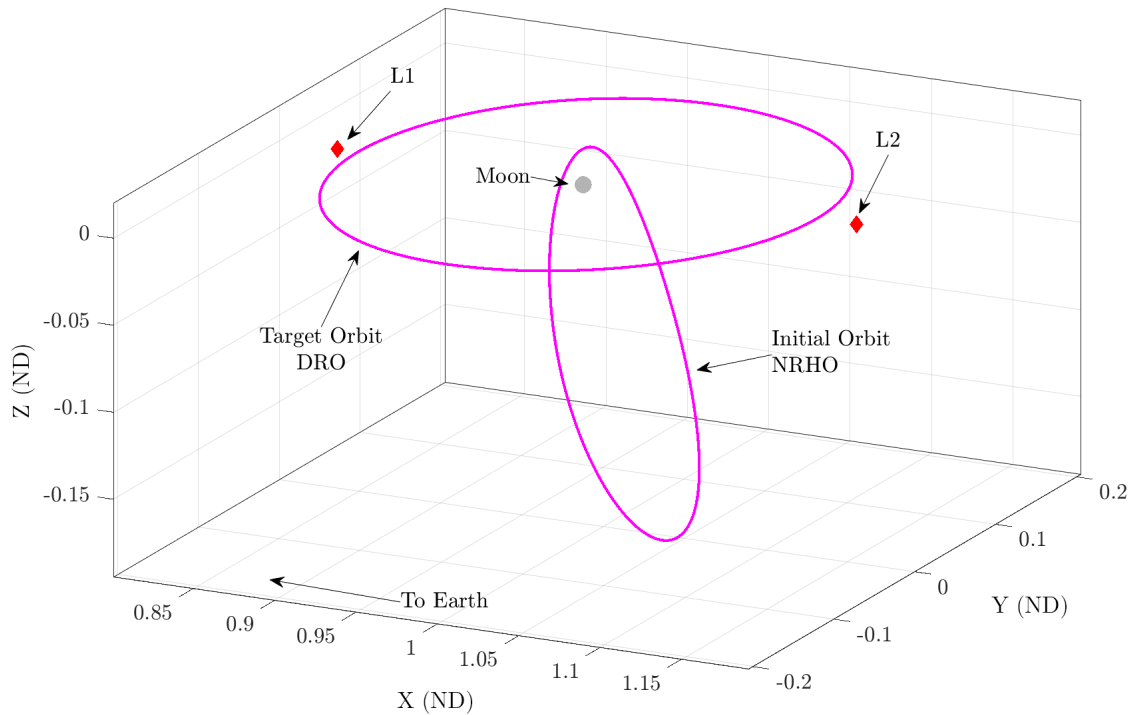
Figure 6.11: NRHO and DRO periodic orbits for transfer problem

Figure 6.11 visualizes the NRHO and the DRO the transfer is to be designed between. It is evident that the NRHO is significantly out-of-plane and posses a close perilune. The DRO is planar and has apparent retrograde motion (clockwise) with respect to the Moon. Table 6.2 lists the initial nondimensional state, dimensional orbit period in days, and the Jacobi constant for these periodic orbits which are referenced in [7].

	x	y	z	$\dot{x}$	$\dot{y}$	$\dot{z}$	T (days)	C
NRHO	1.0456	0	-0.19465	0	-0.14916	0	7.96	3.0277
DRO	0.84947	0	0	0	0.47939	0	10.04	2.9604

Table 6.2: NRHO and DRO periodic orbits (all units are nondimensional unless noted)

Two spacecraft models are considered for the transfer design; a small spacecraft with an initial mass of 500 kg and a larger spacecraft with an initial mass of 3000 kg. Both spacecraft are assumed to have a fixed maximum thrust output and specific impulse. Further, it is assumed that the engines are not throttleable. Table 6.3 summarizes the small and large spacecraft models properties.

		Small	Large
Initial Mass	(kg)	500.0	3000.0
Specific Impulse	(s)	2500.0	2000.0
Maximum Thrust	(N)	0.1	0.45

Table 6.3: Spacecraft models considered for the transfer design.

6.2.1   Initial Guess Construction

We begin the transfer design process by constructing the initial guess path for the spacecraft. Starting with the NRHO, we can assess the periodic orbit's stability index to determine if a set of invariant manifolds exist. The stability index is the sum of the eigen values of the monodromy matrix and for this particular NRHO is 1.6926. Applying techniques discussed in Chapter 4, it is determined that manifold structures exist for this periodic orbit. The DRO is a stable periodic orbit and thus manifolds are not considered for the arrival leg. An unstable departure manifold from

the NRHO is shown in Figure 6.12 in magenta consisting of 150 trajectories. A long propagation time, in excess of 18 nondimensional units, is required to see trajectories depart the vicinity of Moon (top subfigure). Because the intended transfer is designed to minimize propellant cost, it is beneficial to accept this longer flight time in exchange for potentially minimal control effort. The manifold eventually returns to the vicinity of the DRO, however a significant out of plane position and(or) velocity components exist in each trajectory making them unfavorable to directly connect to the DRO. Instead, the manifold is propagated to the negative x-axis crossing. This surface of section was taken as out of plane components could be corrected for at apolune. Two arcs are used to connect the manifold to the DRO via the $1:2$ (shown in blue) or $2:3$ (shown in cyan) planar resonant periodic orbit family. Members of these families are selected for their terminal vicinity to the DRO for positive y-velocity crossings in the L_1 vicinity. Two initial guess geometries for this transfer are implemented through this example to determine which path yields the lowest propellant mass fraction. A one-sided Poincaré directional surface of section along the negative x-axis is used to analyze candidate manifold and intermediate resonant orbits with minimal state discontinuities.

Figure 6.13 is a Poincaré map generated from this surface of section with the NRHO manifold (magenta), $1:2$ (blue), and $2:3$ (cyan) orbits plotted. The region of interest where position discontinuities are minimized are indicated by black boxes. All NRHO manifold points have some out-of-plane velocity component and candidates in the region of interest have negative velocity values meaning in additional time, they will cross the x/y-plane. This is of interest as the motion in the desired direction, and control arcs along these trajectories can correct for the out-of-plane motion. Within the regions of interest in the Poincaré map, two different NRHO manifolds and two resonant orbits are selected such that the terminal resonant orbit state is sufficiently close to the DRO. Better suited resonant candidates connecting to the NRHO exist for both cases but these trajectories have significantly closer perilunes than the DRO and generally proceed away from the vicinity of the Moon early on. Therefore it is desired to find a DRO that roughly approaches the same perilune as the DRO to minimize position discontinuities.
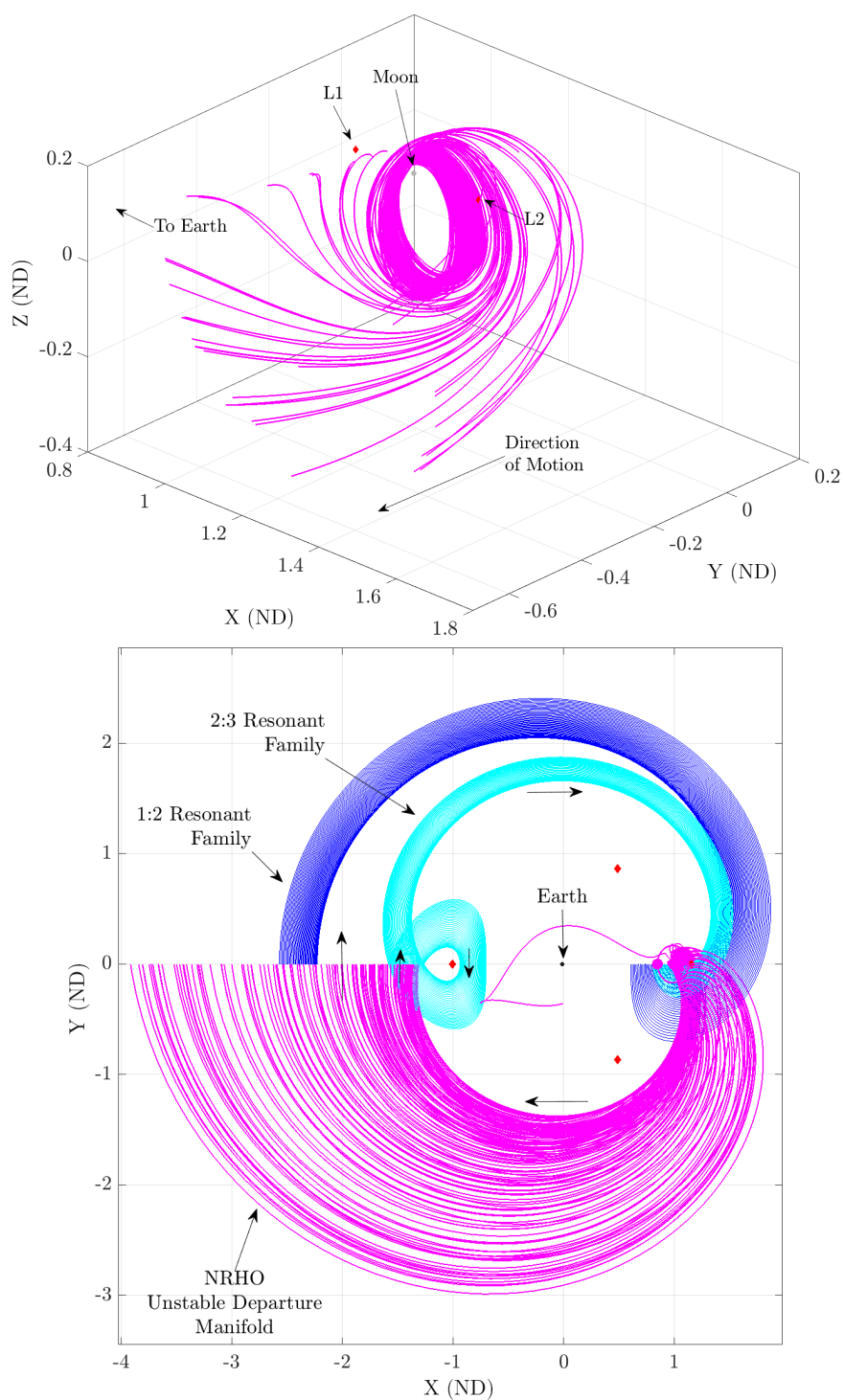
Figure 6.12: NRHO unstable departure manifold (magenta) and potential resonant connecting arcs (blue and cyan).
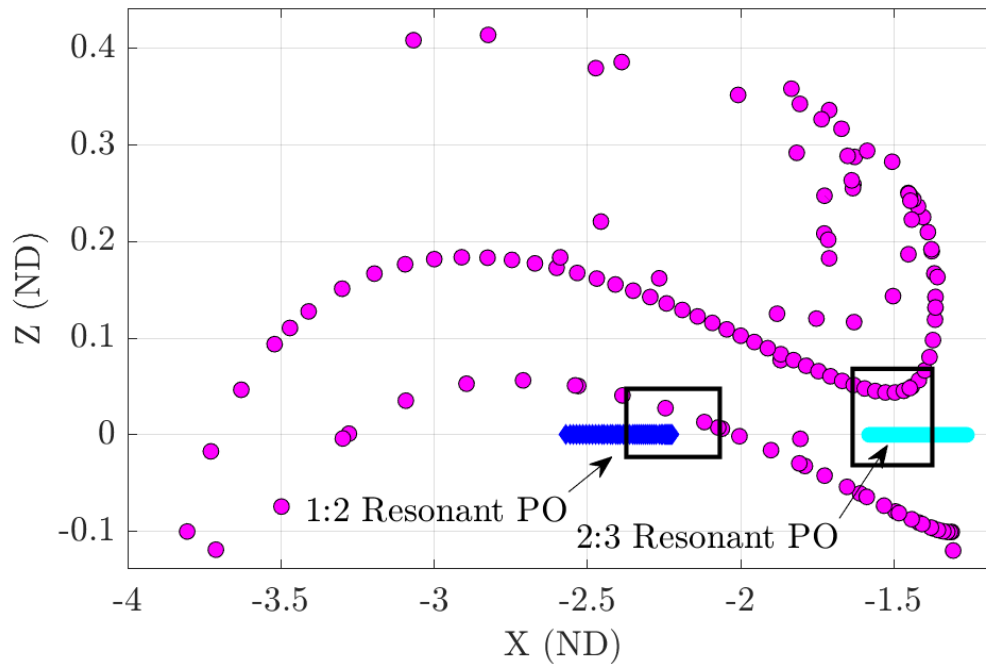
Figure 6.13: Poincaré map from the $y = 0$ surface of section. Regions of interest are boxed for potential transfers.

Figure 6.14 contains the two potential initial guess transfers from the NRHO to the DRO. Subfigures (a) and (b) are of the path using a $1 : 2$ resonant orbit intermediate arc in a two-link orbit chain. Subfigures (c) and (d) are of the same context but with the $2 : 3$ resonant orbit. For all the subplots, the cyan arcs are the specific resonant periodic orbits, the blue arc is the NRHO departure manifold trajectory, and the magenta orbits indicate the initial and terminal periodic orbits. Control segments are placed early on in the guess path such that the manifold departing motion is initiated. Recall that the departure manifolds have considerable out of plane components. Therefore, additional control is necessary to patch this arc with the planar resonant orbits and DRO. The $1 : 2$ resonant candidate has a Jacobi constant of 2.793789 and the $2 : 3$ has a Jacobi constant of 2.826857. These vary significantly from the arrival DRO and so control segments are placed in the terminal portion of the intermediate arc and along the DRO arc to create a spiraling motion. The initial guess control profile is constructed to account for the out-of-plane motion near apoapsis. For the DRO arrival, the control is initially assumed to be in the anti-velocity direction to increase

the Jacobi constant. To expedite the initial feasible solution convergence for both guesses, a base case of spacecraft properties was chosen that have significantly higher initial accelerations than the mission design models. This simplifies the process as a single feasible solution is iteratively stepped towards feasible solutions respective to the intended spacecraft models. The thrust, mass, and Isp selected are: 0.5N, 500kg, and 2000s respectively.
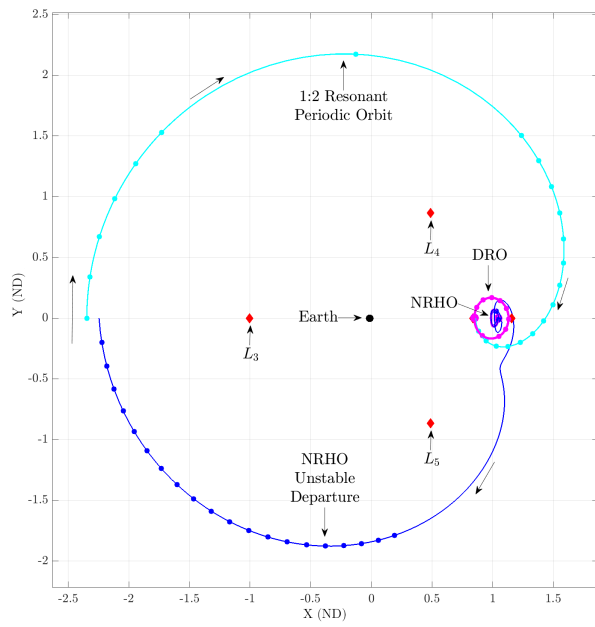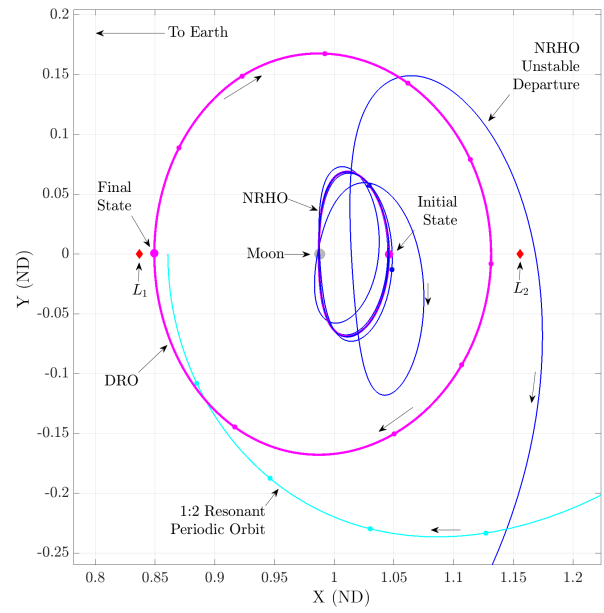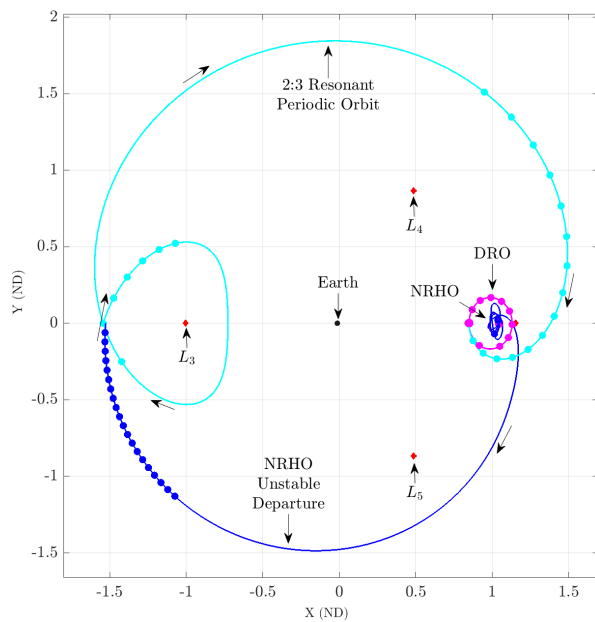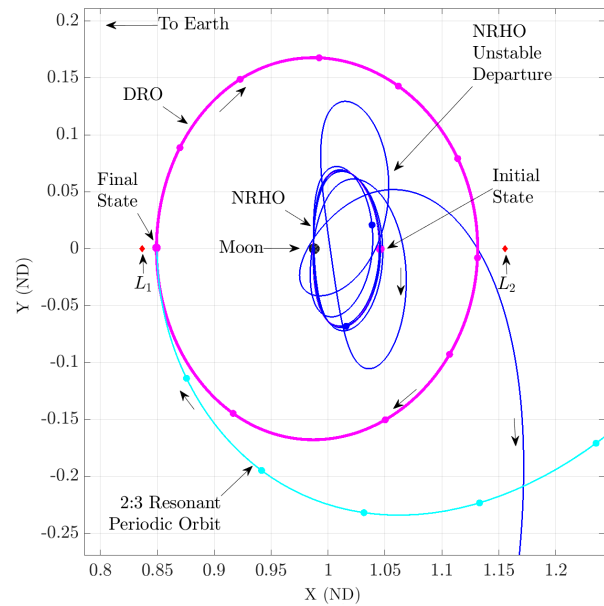
Figure 6.14: Initial guess with arc discretization for the NRHO to DRO transfer trajectory where subfigures (a) and (b) correspond to the 1 : 2 resonant arc guess and (c) and (d) correspond to the 2 : 3 resonant arc guess

6.2.2   Continuation of Spacecraft Parameters

Once the base case feasible solution is converged for both trajectory designs, we can employ natural parameter continuity in the spacecraft thrust and(or) mass to tailor the initial guess to the mission design constraints. Figure 6.15 plots the $1 : 2$ intermediate base case ($m_0 = 500$ kg) solution and additional feasible transfers varying the initial spacecraft mass up to 3000 kg. The maximum available thrust is fixed at 0.5N and the specific impulse is 2000s. Red arcs indicate thrusting and blue arcs are when the spacecraft is coasting. A similar geometry in the initial guess is seen across each of the solutions. Though, as the spacecraft acceleration capability decreases, the transfer flight times increase, thus pushing the incoming arc further away from Moon and thrusting for an increased time duration. Continuity is applied again from the $1 : 2$ intermediate base case.
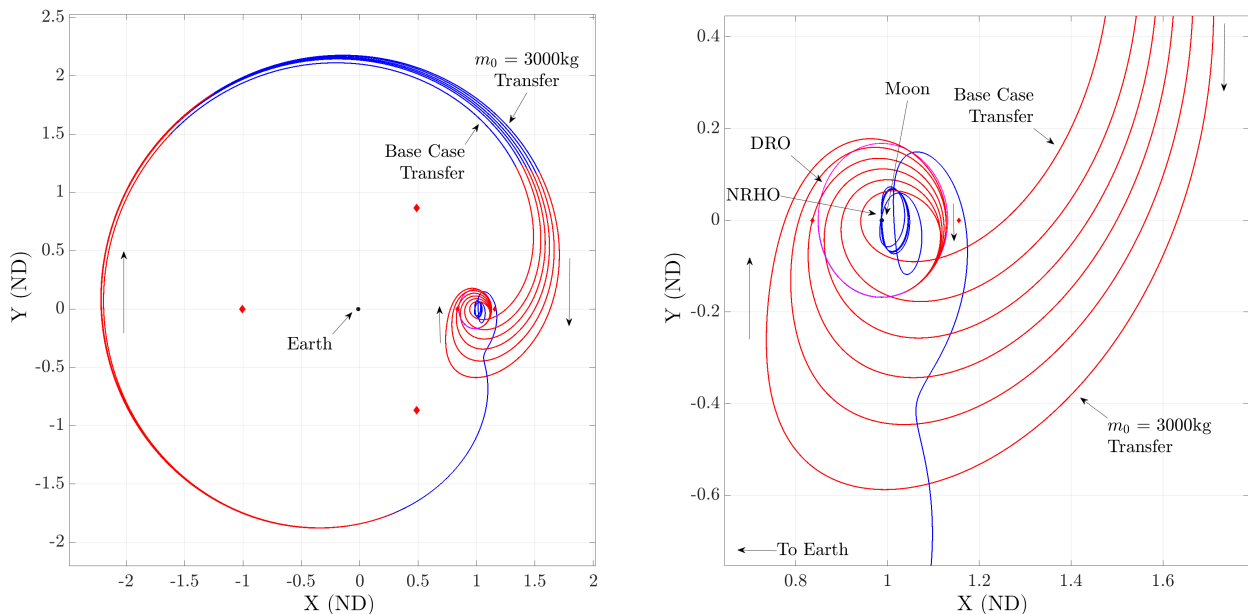
Figure 6.15: 1:2 resonant transfer continuation for varying initial mass (m_0) parameter.

In Figure 6.16 a similar solution geometry is observed as the mass and specific impulse are held constant to the base case for the small spacecraft parameters but the thrust is reduced to meet the mission design requirement from 0.5N to 0.1N. A total of four transfers between the NRHO and DRO are demonstrated. The following figures apply the same method of continuity to the $2 : 3$ intermediate arc initial guess. In Figure 6.17 the mass is increased, and in Figure 6.18 the
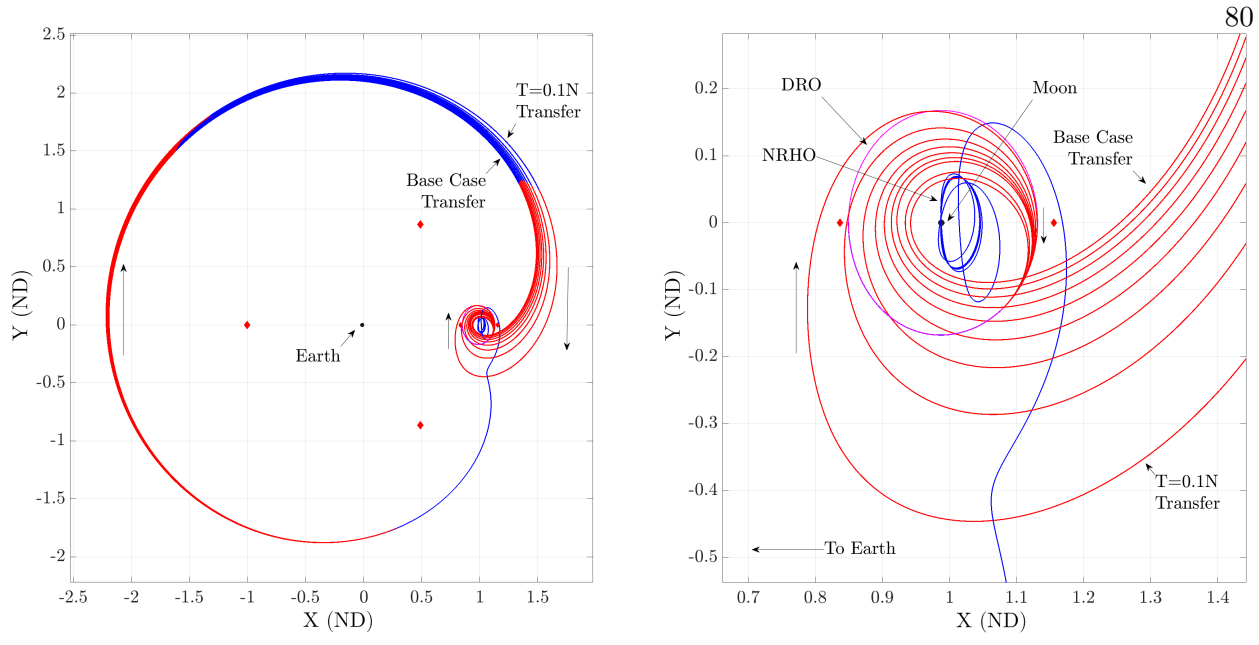
Figure 6.16: 1:2 resonant transfer continuation for varying max thrust (T) parameter.

thrust is decreased. In both cases it is evident that the initial $2:3$ planar resonant loop occurring around the L_3 is significantly altered in each of the feasible guesses. The feasible transfers with the
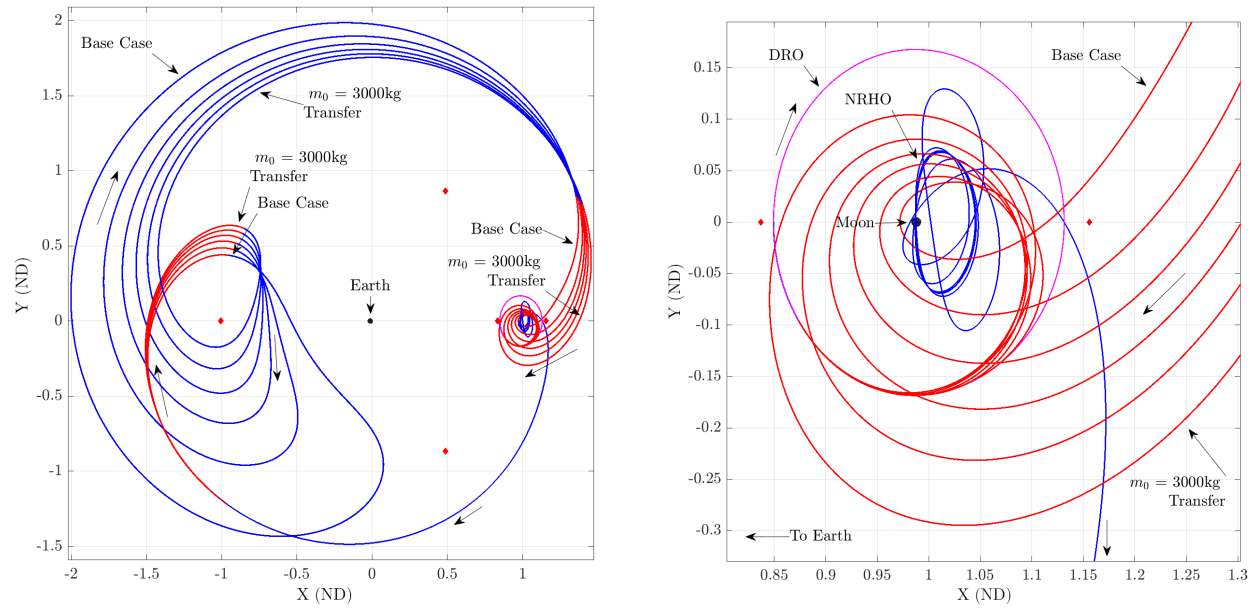
Figure 6.17: 2:3 resonant transfer continuation for varying initial mass (m_0) parameter.

least amount of spacecraft acceleration have the smallest loops about the L_3 as they're unable to

modify the geometry from the initial guess path as much as higher acceleration trajectories. As the acceleration increases, the loop motion becomes increasingly out-of-plane, which is then corrected at the arrival low thrust burn. These cases also exhibit close perilunes and have shorter transfer times of flight. A similar family of solutions is seen when reducing the thrust available, but these
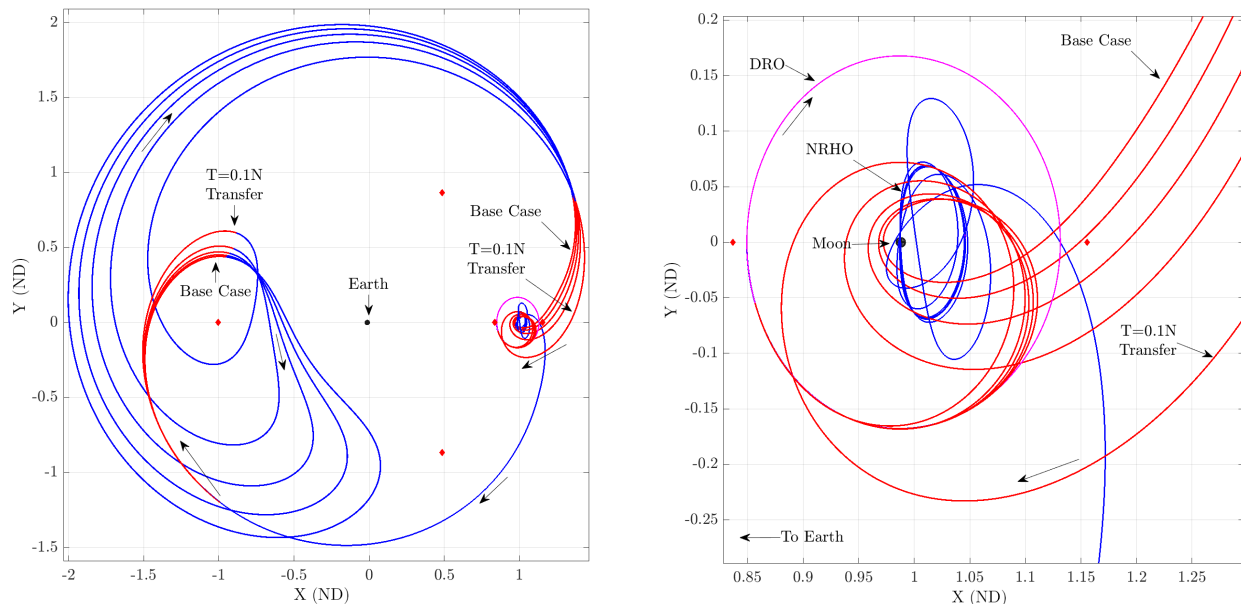
Figure 6.18: 2:3 resonant transfer continuation for varying max thrust (T) parameter.

are slightly modified in their loop geometry. More cases appear to transfer closer to the vicinity of the Moon prior to arrival than the mass variation family of solutions. From the families of feasible solutions, we can now take one or multiple to optimization to reduce the propellant mass fraction.

Through this transfer example, a total of four cases are carried to optimization. For distinction between cases, Table 6.4 summarizes the case names and conditions for each transfer.

Case Name	Spacecraft Type	Intermediate Periodic Orbit
1A	Small	$1:2$
1B	Large	$1:2$
2A	Small	$2:3$
2B	Large	$2:3$

Table 6.4: Transfer cases considered in the NRHO to DRO transfer design example

6.2.3   Transfer Optimization

Table 6.5 covers the feasible initial guess and post-optimization trajectory properties for case 1A and 1B. The feasible initial guess solutions have transfer times of 153 and 156.5 days. The propellant mass is 12.56 kg and 82.35 kg respectively which translate to a mass fraction with respect to the initial spacecraft mass around 2.6%. Post optimization, the propellant mass decreases to

Parameter	Units	$m_0 = 500$ kg		$m_0 = 3000$ kg	
		Initial Guess	Optimized	Initial Guess	Optimized
Transfer Time	(days)	152.989	155.3513	156.5424	155.366
Final Mass	(kg)	487.4348	493.4205	2917.6407	2946.3694
Prop. Mass	(kg)	12.5652	6.5795	82.3593	53.6306
Prop. Fraction	-	0.02513	0.013159	0.027453	0.017877
Prop. Reduction	(kg)	-	5.9857	-	28.7287

Table 6.5: Optimized transfer results versus feasible initial guess for case 1A and 1B

1.31% and 1.79% for the small and large spacecraft cases, and both have a similar transfer flight times of around 155.35 days. The propellant savings for both transfers are considerable at 5.99 kg and 28.73 kg which accounts for roughly a 1% increase in the payload mass delivered.

The optimized trajectories are shown in Figure 6.19 where subfigures (a) and (b) correspond to case 1A and (c) and (d) are for case 1B. Transfers depart the NRHO with a low thrust burn of 0.25 and 8.6 hours near perilune for the small and large spacecraft cases. Both exhibit similar geometries in the exterior region of the transfer where thrusting is performed near apoapsis. The small spacecraft case performs a low thrust burn for 6.4 days while the larger model has a 7.1 day maneuver. The thrust direction is generally in the the velocity direction of the trajectory as the spacecraft needs to decrease the Jacobi constant to continue along the resonant transfer path. The longest burn occurs at the end of the transfers and lasts roughly 11.8 days for case 1A and 19.5 days for case 1B. This burn continues through the loop around the Moon before rendezvousing with the DRO at the fixed terminal state. The trajectory geometry of the feasible transfer is generally retained post optimization, but control directions and thrusting durations are significantly altered to reduce the control cost.

The feasible initial guess and post-optimization for transfers 2A and 2B are presented in Table 6.6. The optimized transfers have flight times that are 173.3 and 174.6 days. Like the previous set of results, the post optimization propellant savings for case 2A and 2B are considerable. The

(a)

(b)

(c)

(d)
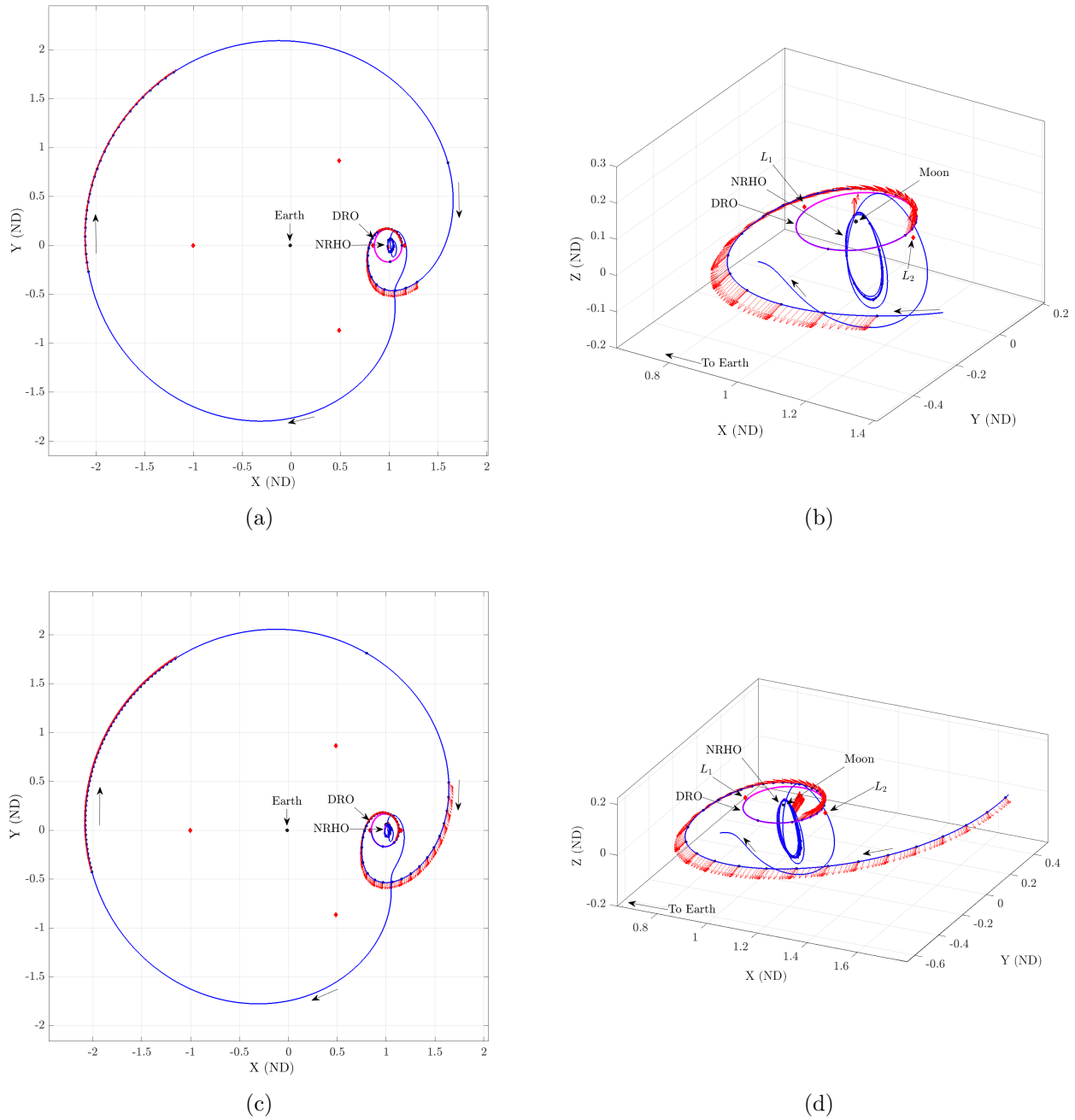
Figure 6.19: Optimized NRHO to DRO trajectories for case 1A (top) and case 1B (bottom)

cost reductions are 4.69 kg and 22.10 kg respectively. The transfers for these cases are presented

Parameter	Units	$m_0 = 500$ kg		$m_0 = 3000$ kg	
		Initial Guess	Optimized	Initial Guess	Optimized
Transfer Time	(days)	171.1978	173.3096	174.7609	174.5944
Final Mass	(kg)	488.9851	493.6738	2930.6043	2952.7034
Prop. Mass	(kg)	11.0149	6.3262	69.3957	47.2966
Prop. Fraction	-	0.02203	0.012652	0.023132	0.015766
Prop. Reduction	(kg)	-	4.6887	-	22.0991

Table 6.6: Optimized transfer results versus feasible initial guess for case 2A and 2B

in Figure 6.20. Like the previous set of solutions, a short duration burn is performed early into the trajectory to depart the vicinity of the Moon and continue towards the exterior region. For the small spacecraft model this burn is 6.90 hours and for large model it is 9.05 hours. In the exterior region the second burn is conducted for both trajectories lasting for 3.3 days and 4.5 days for cases 2A and 2B respectively. These burns are shorter than the equivalent maneuvers performed in the case 1 transfers. Both optimal solutions retain similar geometric features from the initial guess feasible solutions. The trajectory loop from the 2 : 3 resonant family is present in the optimal solutions, but the size and location of these features vary considerably. Thrusting arcs are moved before the loop portion in the trajectory and the durations are much shorter. The case 2 solutions present a considerable out-of-plane component with respect to the case 1 solutions and an example of this is seen in Figure 6.21. Consequently the arrival low thrust burns include a much greater out-of-plane component compared to the case 1 results. The case 2 maneuvers are 14.5 and 19 days long for the small and large spacecraft models respectively. The trajectories generated in case 2 share similarities to a NRHO to DRO transfer discussed in [38]. The spacecraft model used in the cited investigation has the same initial acceleration capability as case 2A, but with varying mass, thrust, and specific impulse values. The transfer has a final mass to initial mass ratio of 0.9870 which is comparable to case 2A which as a mass ratio of 0.9874. The transfer geometry is similar where the solution departs the NRHO through an unstable manifold and uses an intermediate 2 : 3 resonant arc to arrive at the DRO. The transfer uses two revolutions about the Moon before rendezvousing

with the terminal DRO state. The time of flight differs as it is 121.3350 days compared to case 2A's 171.1978 days. This is likely attributed to the departure time spent in the vicinity of the NRHO. Overall, the optimized transfer in case 2A shares similarities in geometry and final mass fraction

(a)

(b)

(c)

(d)
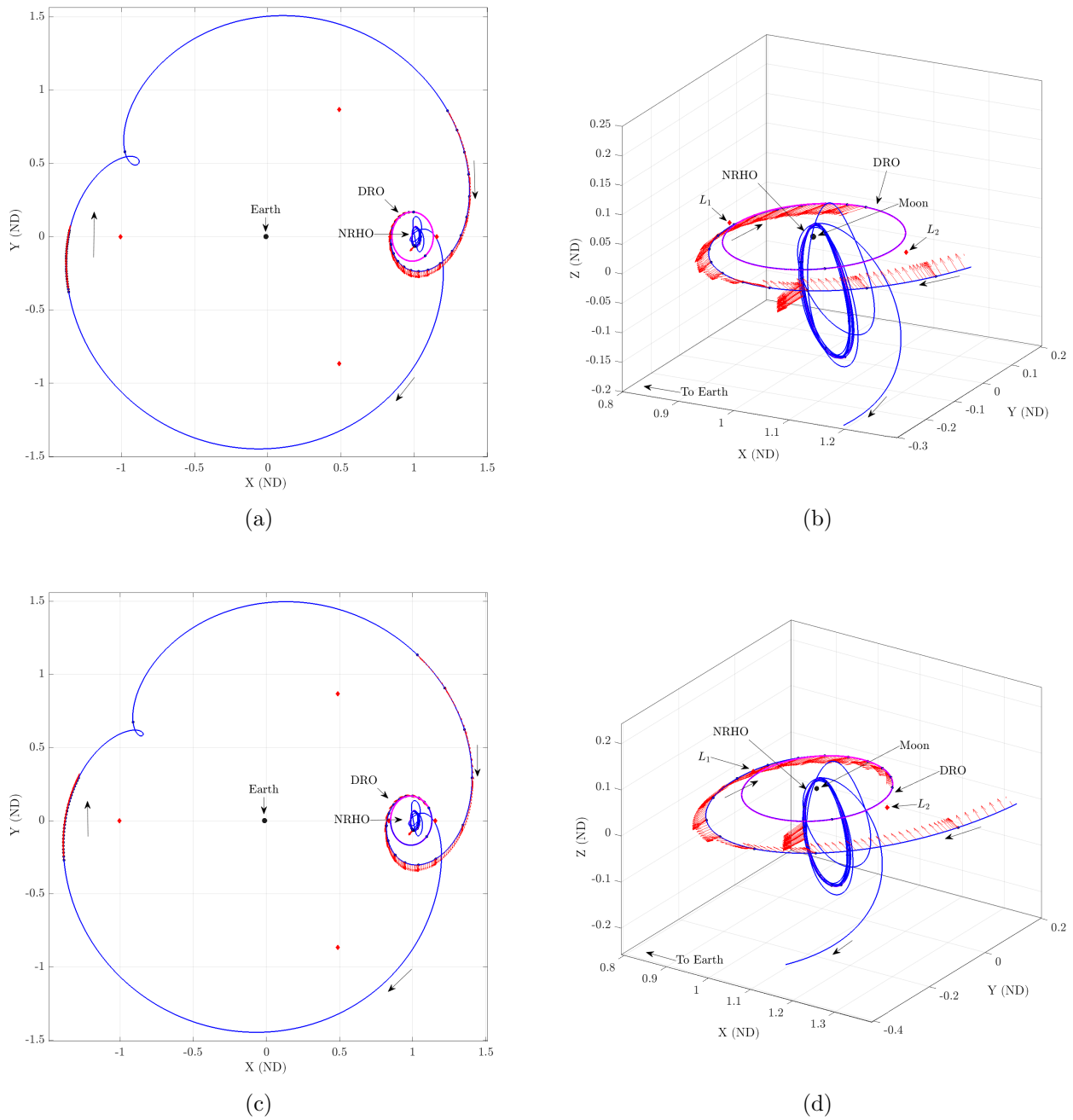
Figure 6.20: Optimized NRHO to DRO trajectories for case 2A (top) and case 2B (bottom)
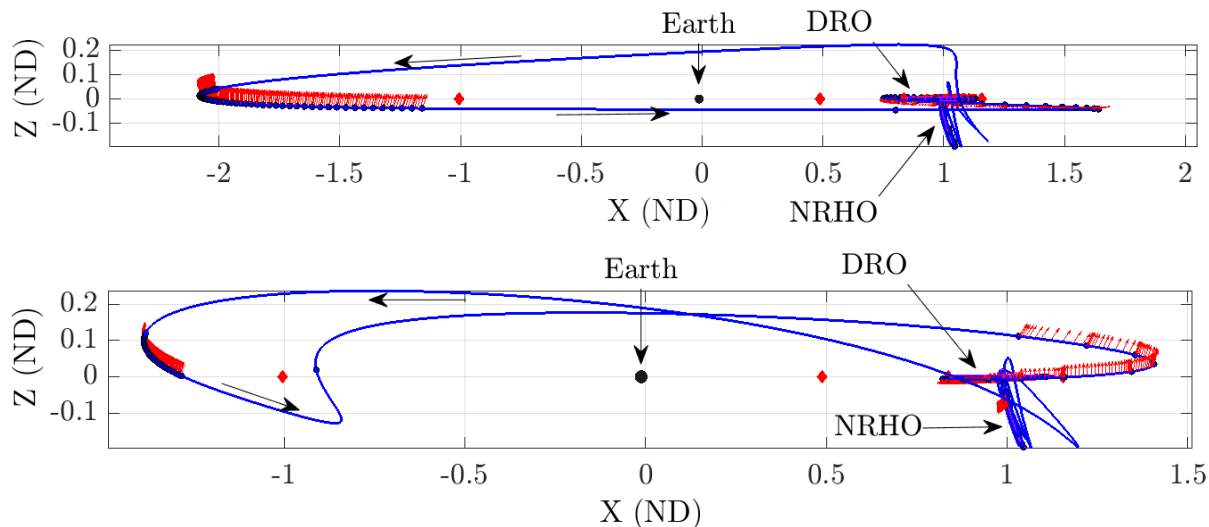
Figure 6.21: X/Z-plane view of case 1B (top) and case 2B (bottom)

with respect to a prior NRHO to DRO transfer design investigated in [38].

Two sets of initial guess paths were created for the two spacecraft to emphasize the dependency of the post-optimization transfer to the initial guess. The case 1A and 1B transfers have faster flight times at around 155 days while case 2A and 2B are around 174 days. For the small spacecraft model, it is seen that utilizing the longer flight time case, 2A, over 1A yields a propellant savings of 0.2533 kg. Similarly, for the larger spacecraft model, the propellant savings that come from the longer duration transfer are 6.334 kg. Figure 6.22 plots the accumulated thrusting duration measured in days versus the trajectory discretization number of segments. Each subfigure contains two plots indicated by the magenta and red colors. The magenta points form the initial feasible solution's thrust duration and the red points form the optimized solution. The blue points indicate coasting segments and thus do not increase in the y-axis. The optimization cost is directly related to the decrease in total thrust duration, which is shown as the gap between the terminal segments for each subplot. This is due to the constant thrust magnitude problem formulation, and it is also evident where the initial guess thrust durations for each trajectory differs from the optimized solution. Case 1B has roughly double the number of segment arcs as this solution was refined to asses the sensitivity of increasing the number of total segments. The trajectory does

(a) Case 1A

(b) Case 1B

(c) Case 2A

(d) Case 2B
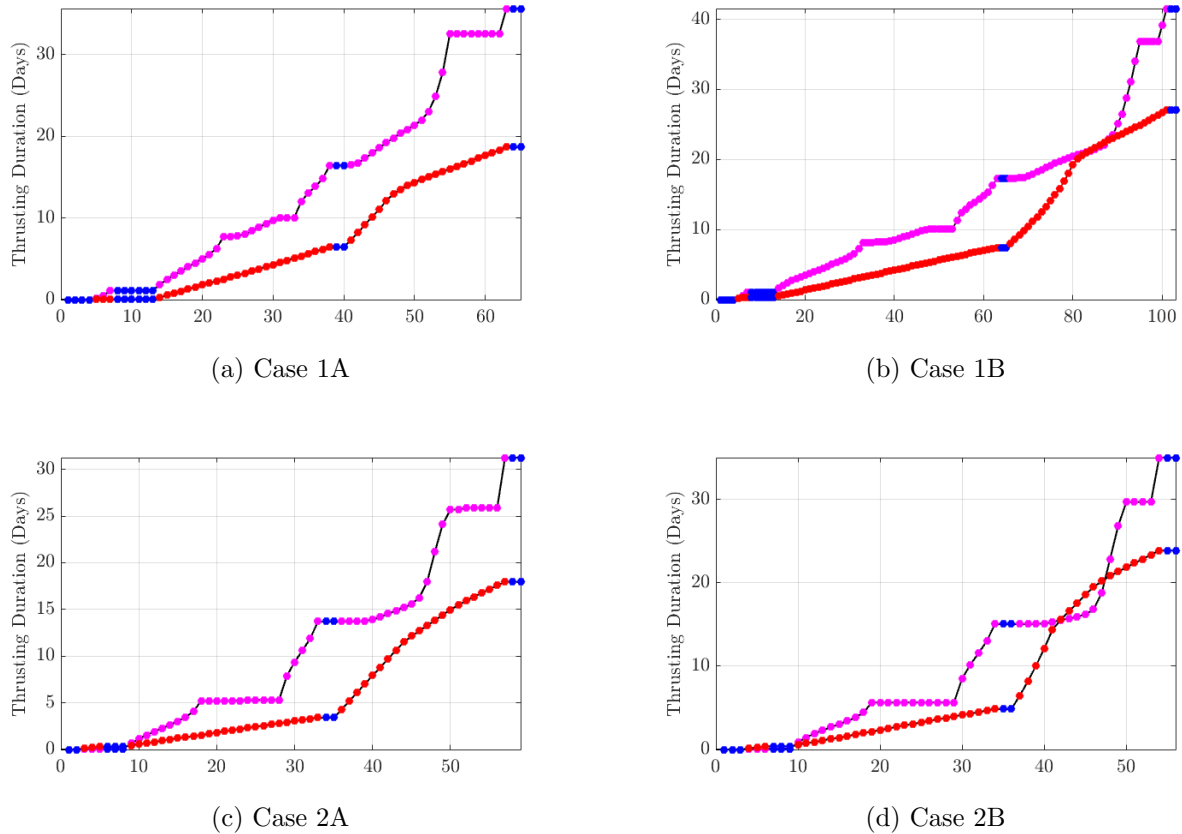
Figure 6.22: Accumulated thrusting duration (days) versus discretization segment count

not pass in close vicinity of the primary or secondary. A larger segment count could theoretically improve the solution as in this region, having a finer resolution in control direction can further utilize the sensitive dynamics to reduce overall control cost. However, for this case, no significant advantage was noticed for the aforementioned reason. Transfer cases 1B and 2B have considerably longer thrust arcs at the end of the transfers compared to cases 1A and 2A.

Figure 6.23 compares the feasible and optimal control profiles versus time for the small spacecraft. In all cases, the location of the three low thrust burns are distinct. The short duration one occurs early into the transfer, the exterior region burn occurs at around 25-30 ND time (roughly 108-130 days), and the arrival burn completes the transfer. The optimized control profile has significantly less variation in the unit directions compared to the initial feasible solutions. Additionally, smooth transitions are seen in direction.

The NRHO to DRO transfer design demonstrates the significance of initial guess path planning and its direct effect on feasible and optimal solutions. By leveraging the unstable departure manifold emanating from the NRHO, a low cost hyperbolic escape from the periodic orbit is possible. Two intermediate arcs are applied in different cases to patch the departing manifold to the arrival DRO using either the $1:2$ or $2:3$ Earth-Moon resonant periodic orbits. Both potential paths create different sets of possible transfers which in turn changes the locally optimal transfer trajectories. The transfers with longer flight times are seen to reduce the propellant consumption. These correspond to using the $2:3$ intermediate arc for the initial guess path.
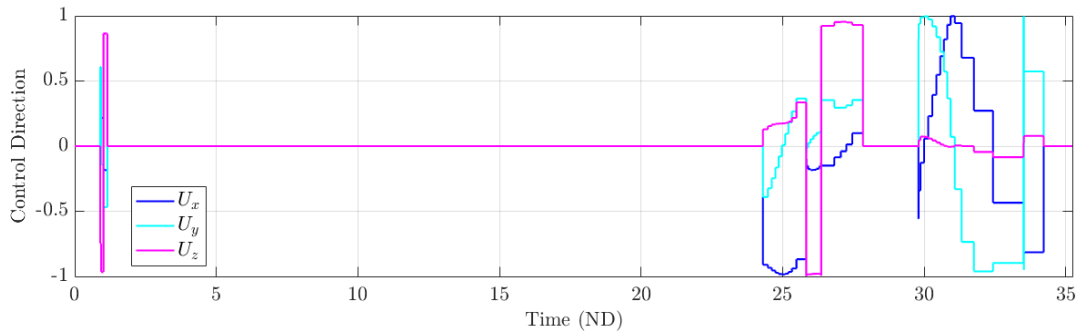
(a) Case 1A Feasible Control Profile
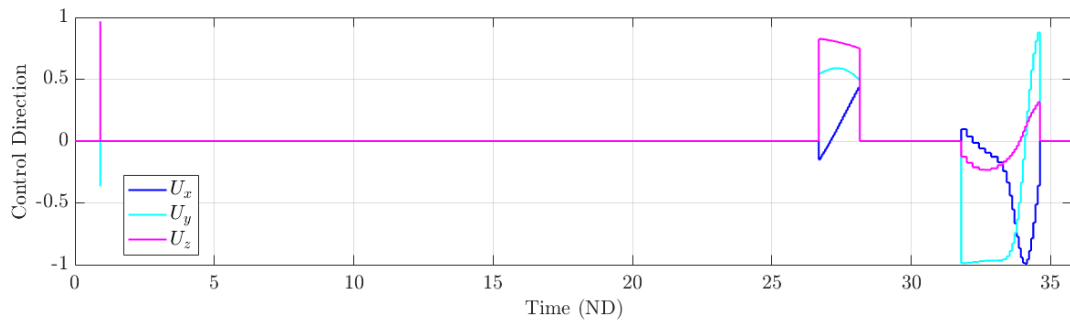
(b) Case 1A Optimized Control Profile
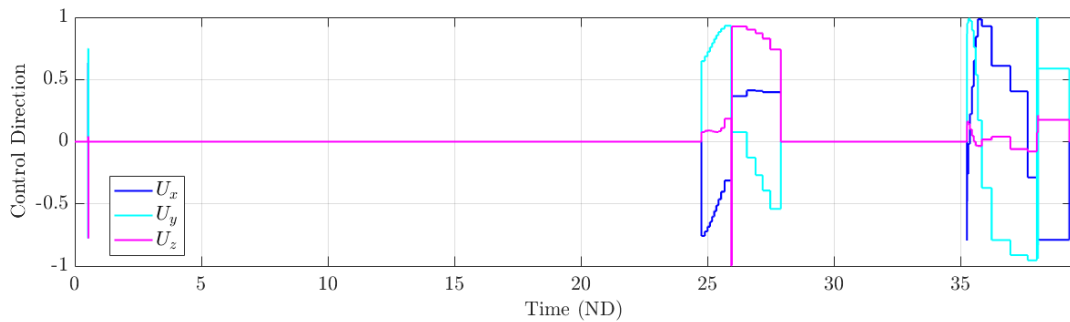
(c) Case 2A Feasible Control Profile
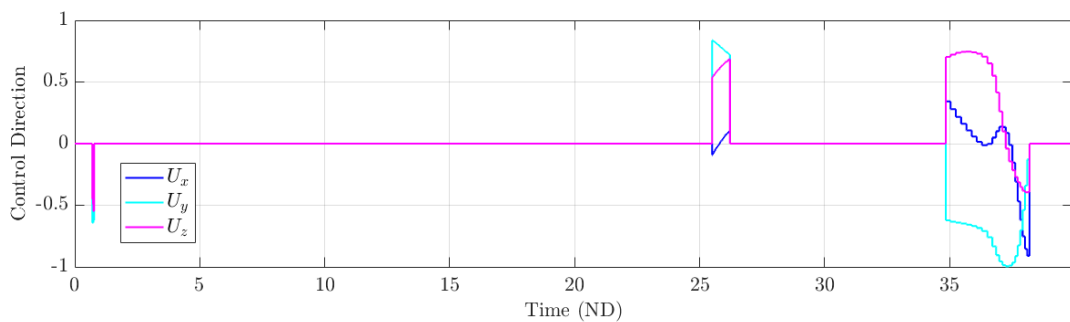
(d) Case 2A Optimized Control Profile

Figure 6.23: Case 1A and 2A control profile versus time for feasible initial guess and optimal transfers

Chapter 7

Conclusion

Methods to formulate low thrust feasible and optimal periodic orbit transfers are explored in this thesis. Dynamical structures and existing solutions in the CR3BP are leveraged successfully to create initial guess paths for transfers. Continuation and correction methods allow the formation of one or many feasible trajectories. Finally, direct optimization was utilized to find several fuel-optimal transfers between periodic orbits in the Earth-Moon system.

7.1   Summary

The thesis begins by establishing the natural and thrust-enabled dynamics of a massless particle under the influence of two circular restricted celestial bodies. The linear mapping of perturbations in time with the state transition matrix proves beneficial in correction and optimization routines. The single and multiple shooting methods allow for corrections of discontinuous initial guess trajectories. Dynamical properties of the CR3BP, including equilibrium points, periodic orbits, invariant manifolds, and orbit chaining are explored to utilize existing solutions for initial guess construction. Finally, continuation and optimization methods are applied to find sets of feasible and propellant-mass locally optimal solutions.

Two example cases are explored in this work which apply concepts of initial guess generation and continuation differently to design one or many transfers between periodic orbits. The first demonstration explored concepts of continuation to generate sets of feasible transfers between subsets of the L_1 northern and L_2 southern halo periodic orbits. A single initial guess was constructed

by patching the departing unstable and stable arriving manifolds from these periodic orbits. Then the corrections and optimization processes yielded the first transfer in the set. Natural parameter continuation was then applied to find an initial set of feasible transfers in the family and select cases were optimized. Continuation was applied from the point case optimizations to update the feasible set and reduce the propellant cost across the transfer family. The next example demonstrated the orbit chaining method applied to a transfer scenario between candidate Deep Space Gateway L_2 southern NRHO to a long term disposal DRO. Two spacecraft types and two initial guess paths were developed using continuation of the spacecraft's parameters and the orbit chaining method. Resonant intermediate periodic orbits connected the NRHO unstable departure manifold to the stable DRO. The optimized transfers retain features of the initial guess thus emphasizing the necessity to possibly prototype multiple initial guess paths.

By leveraging dynamical systems theory and numerical methods for correction and optimization, low thrust transfers between periodic orbits are possible in the CR3BP. Strategies to form these transfer paths are discussed and locally optimal solutions between periodic orbits in the Earth-Moon system are successfully computed.

7.2   Recommendations for Future Work

Through this research, a number of potential improvements and areas of interest were noted for follow on work. Additional transfer examples, investigation into different intermediate geometries, optimization methods, and visualization techniques for initial guess construction are all areas that can be expanded on to improve the low thrust transfer design process in the CR3BP. These areas are discussed below:

(i) As interest in cisluar exploration continues to grow, the need for mission designs between periodic orbits in the Earth-Moon system will also increase. This research focused on specific cases in a multitude of possible transfers for scientific, observation, communication, and human spaceflight activities. Leveraging stable periodic orbits or the relative stability of the L_4 and

L_5 points in the system can be beneficial for long term observation spacecraft. Transfers to and from these orbits can accommodate cislunar operations to and from the DSG Lunar outpost. Additionally space domain awareness type missions can benefit from transfers in this system.

(ii) Prototyping multiple initial guess trajectories should be considered for a more robust search space analysis. Zero or multiple revolution solutions exist which have design trade offs. Exploration into different initial guesses and their effect on the current and family of solutions is important to potentially find better transfers.

(iii) The orbit chaining examples in this thesis only consider planar periodic orbits as intermediate arcs. However spatial resonant periodic orbits exist in the system and may be useful candidates for the examples presented or other periodic orbit transfers. Additionally, stacking multiple same-family orbits can be helpful in modeling spiraling motion for large energy changes.

(iv) This thesis utilizes on direct optimization with the interior point algorithm and multiple shooting. As the complexity of the solution increases, discretization of the transfer arcs yield increasingly large decision vectors for optimization which in turn increases the compute time. For example, a transfer between two halo periodic orbits in the same family may require many revolutions depending on the spacecraft's acceleration capability. In this case, indirect optimization or collocation schemes[37] may offer benefits.

(v) Finally, reducing inefficiencies at each point in the design process is essential for increased search space exploration. Recommendations to streamline the process include creating interactive visualizations for rapid prototyping initial guess paths. A graphical tool, such as the Deep Space Trajectory Explorer (DSTE)[27], to search for orbit chaining sequences and arc durations would improve the efficiency in the path generation. Discretization with interactive methods can make prototyping many variations of a single transfer more convenient.

Bibliography

[1] National Aeronautics and Space Administration. The artemis accords principles for cooperation in the civil exploration and use of the moon, mars, comets, and asteroids for peaceful purposes. `https://www.nasa.gov/specials/artemis-accords/img/Artemis-Accords-signed-13Oct2020.pdf`, Accessed: 4-1-2023.

[2] National Aeronautics and Space Administration. Glenn contributions to deep space 1. `https://www.nasa.gov/centers/glenn/about/history/ds1.html`, Accessed: 3-29-2023.

[3] B.T. Barden. Using stable manifolds to generate transfers in the circular restricted problem of three bodies. Master's thesis, Purdue University, West Lafayette, IN, 12 1994.

[4] N. Bosanac. Leveraging Natural Dynamical Structures to Explore Multi-Body Systems. PhD thesis, Purdue University, West Lafayette, IN, 07 2016.

[5] James Burke. 1. line search methods. `https://sites.math.washington.edu/~burke/crs/408/notes/nlp/line.pdf`, Accessed: 4-13-2023.

[6] R.H. Byrd, M.E. Hribar, and J. Nocedal. An interior point algorithm for large-scale nonlinear programming. In SIAM Journal on Optimization, volume 9, pages 877–900, 1999.

[7] L.R. Capdevila and K. Howell. A transfer network linking earth, moon, and the triangular libration point regions in the earth-moon system. Advances in Space Research, 62, 2018.

[8] S. Chikine. Low-thrust trajectory optimization in the circular restricted three body problem. Master's thesis, University of Colorado at Boulder, Boulder, CO, 5 2019.

[9] J. Crusan, R. Smith, D. Craig, J. Caram, J. Guidi, M. Gates, J.. Krezel, and N. Herrmann. Deep space gateway concept: Extending human presence into cislunar space. In IEEE Aerospace Conference Proceedings, volume 2018-March, 2018.

[10] J.A. Dahlke, A.P. Wilmer, and R.A. Bettinger. Preliminary comparative assessment of l2 and l3 surveillance using select cislunar periodic orbits. In AAS/AIAA Astrodynamics Specialist Conference, Charlotte, NC, 8 2022.

[11] K.E. Davis. Locally optimal transfer trajectories between libration point orbits using invariant manifolds. PhD thesis, University of Colorado at Boulder, Boulder, CO, 01 2009.

[12] E.J. Doedel, D.J. Dichmann, J. Galán-Vioque, H.B. Keller, R.C. Paffenroth, and A. Vanderbauwhede. Elemental periodic orbits of the cr3bp: A brief selection of computational results. In Equadiffe, pages 163–168, 2003.

[13] I. Elliot, C. Sullivan, N. Bosanac, J.R. Stuart, and F. Alibay. Designing low-thrust trajectories for a smallsat mission to sun-earth l5. In Journal of Guidance, Control, and Dynamics, volume 43, 10 2020.

[14] G. Gómez, A. Jroba, J.E. Marsden, and C. Simó. Study of the transfer from the earth to a halo orbit around the equilibrium point l1. Technical report, ESOC Contract Report, Technical Report, 12 1991.

[15] G. Gómez, W.S. Koon, M. Lo, J.E. Marsden, J. Masdemont, and S.D. Ross. Invariant manifolds, the spatial three-body problem and space mission design. In Advances in Astronautical Sciences, volume 109, 8 2001.

[16] G. Gómez, W. S. Koon, M. W. Lo, J. E. Marsden, J. Masdemont, and S. D. Ross. Connecting orbits and invariant manifolds in the spatial restricted three-body problem. Nonlinearity, 17, 2004.

[17] A.F. Haapala. Trajectory Design in the Spatial Circular Restricted Three-Body Problem Exploiting Higher-Dimensional Poincare Maps. PhD thesis, Purdue University, West Lafayette, IN, 2014.

[18] K. Howell. Three-dimensional, periodic, "halo" orbits. Celestial Mechanics, 32, 1984.

[19] K. Howell, B. Barden, and M. Lo. Application of dynamical systems theory to trajectory design for a libration point mission. In The Journal of the Astronautical Sciences, volume 45, 1997.

[20] The MathWorks Inc. Constrained nonlinear optimization algorithms, 2022. `https://www.mathworks.com/help/optim/ug/constrained-nonlinear-optimization-algorithms.html`.

[21] The MathWorks Inc. Fmincon, 2022. `https://www.mathworks.com/help/optim/ug/fmincon.html`.

[22] R. Jehn, J. Schoenmaekers, D. García Yárnoz, and P. Ferri. Bepicolombo-a mission to mercury. In 21st International Symposium on Space Flight Dynamics (ISSFD), Toulouse, France, 3 2009.

[23] W.S. Koon, M.W. Lo, J.E. Marsden, and S.D. Ross. Dynamical Systems, The Three-Body Problem, and Space Mission Design. Marsden Books, 1 edition, 2006.

[24] H. Kuninaka, K. Nishiyama, Y. Shimizu, I. Funaki, H. Koizumi, S. Hosoda, and D. Nakata. Hayabusa asteroid explorer powered by ion engines on the way to earth. In 31st International Electric Propulsion Conference, Ann Arbor, MI, 1 2009.

[25] G. Lantoine. Efficient nrho to dro transfers in cislunar space. In Advances in the Astronautical Sciences, volume 162, 2018.

[26] J. Longuski, J. Guzmán, and J. Prussing. Optimal Control with Aerospace Applications. Springer Space Technology Library, 2014.

[27] B. McCarthy, J. Petersen, and D. Davis. Aas 23-166 ballistic lunar transfer design using the deep space trajectory explorer. In Advances in the Astronautical Sciences, 1 2023.

[28] S. McCarty, L. Burke, and M. McGuire. Analysis of cislunar transfers from a near rectilinear halo orbit with high power solar electric propulsion. In AAS/AIAA Astrodynamics Specialist Conference Snowbird, UT, 3 2018.

[29] S. McCarty and M. McGuire. Parallel monotonic basin hopping for low thrust trajectory optimization. In 2018 Space Flight Mechanics Meeting. American Institute of Aeronautics and Astronautics, 1 2018.

[30] M. McGuire, L. Burke, S. McCarty, K. Hack, R. Whitley, D. Davis, and C. Ocampo. Low thrust cis-lunar transfers using a 40 kw-class solar electric propulsion spacecraft. In Advances in the Astronautical Sciences, volume 162, 2018.

[31] D. Morante, M. Rivo, and M. Soler. A survey on low-thrust trajectory optimization approaches. In Aerospace, volume 8, 2021.

[32] Z.E. Musielak and B. Quarles. The three-body problem. In Reports on Progress in Physics, volume 77, page 065901. IOP Publishing, 6 2014.

[33] K. Oshima. Vertically stable and unstable manifolds of planar periodic orbits: Applications to spacecraft and asteroid trajectories. In Advances in the Astronautical Sciences, volume 168, 2019.

[34] J.S. Parker and R.L. Anderson. JPL Deep Space Communication and Navigation Series Low-Energy Lunar Trajectory Design. John Wiley and Sons, Hoboken, New Jersey, 2014.

[35] J.S. Parker, K.E. Davis, and G.H Born. Chaining periodic three-body orbits in the earth-moon system. In Acta Astronautica, volume 67, 8 2010.

[36] G.E. Philip, W. Murray, and M.A. Saunders. Snopt: An sqp algorithm for large-scale constrained optimization. SIAM J. Optimization, 12(4):979–1006, 2002.

[37] R. Pritchett, K. Howell, and D. Grebow. Low-thrust transfer design based on collocation techniques: Applications in the restricted three-body problem. In Advances in the Astronautical Sciences, volume 162, 2018.

[38] R. Pritchett, E. Zimovan, and K. Howell. Impulsive and low-thrust transfer design between stable and nearly-stable periodic orbits in the restricted problem. In 2018 Space Flight Mechanics Meeting, 3 2018.

[39] J. Prussing. Optimal Spacecraft Trajectories. Oxford University Press, 2018.

[40] M. Rayman, P. Varghese, D. Lehman, and L. Livesay. Results from the deep space 1 technology validation mission. Acta Astronautica, 47, 2000.

[41] R. Restrepo and R. Russell. Aas 17-695 patched periodic orbits: A systematic strategy for low energy transfer design. In AIAA/AAS Astrodynamics Specialist Conference, Stevenson, WA, 3 2017.

[42] R.L. Restrepo Gómez. Patched periodic orbits : a systematic strategy for low-energy trajectory and moon tour design. PhD thesis, The University of Texas at Austin, Austin, TX, 09 2018.

[43] D.L. Richardson. Halo orbit formulation for the isee-3 mission. In Journal of Guidance and Control, volume 3, pages 543–548, 1980.

[44] C. Russel and C. Raymond. <u>The Dawn Mission to Minor Planets 4 Vesta and 1 Ceres</u>. Springer, New York, NY, 2012.

[45] J.S. Snyder, D.M. Goebel, V. Chaplin, A.L. Ortega, I.G. Mikellides, F. Aghazadeh, I. Johnson, T. Kerl, and G. Lenguito. Electric propulsion for the psyche mission. In <u>36th International Electric Propulsion Conference</u>, 8 2019.

[46] V. Szebehely. <u>The Theory of Orbits The Restricted Problem of Three Bodies</u>. Academic Press, New Haven, CT, 1967.

[47] M. Vaquero and K. Howell. Leveraging resonant orbit manifolds to design transfers between libration point orbits in multi-body regimes. In <u>23rd AAS/AIAA Space Flight Mechanics Meeting</u>, 3 2013.

[48] M. Vaquero and K. Howell. Leveraging resonant-orbit manifolds to design transfers between libration-point orbits. <u>Journal of Guidance, Control, and Dynamics</u>, 37, 2014.

[49] M. Vaquero and J. Senet. Poincare: A multi-body, multi-system trajectory design tool. In <u>7th International Conference on Astrodynamics Tools and Techniques (ICATT)</u>, DLR Oberpfaffenhofen, 11 2018.

[50] M. Vaquero Escribano. Poincaré sections and resonant orbits in the restricted three-body problem. Master's thesis, Purdue University, West Lafayette, IN, 5 2010.

[51] Y. Wang, R. Zhang, C. Zhang, and H. Zhang. Transfers between nrhos and dros in the earth-moon system. <u>Acta Astronautica</u>, 186, 2021.

[52] J. Williams, D. Lee, R. Whitley, K. Bokelmann, D. Davis, and C. Berry. Targeting cislunar near rectilinear halo orbits for human space exploration. In <u>27th AAS/AIAA Space Flight Mechanics Meeting</u>, 3 2017.

[53] A. Wilmer, R.A. Bettinger, and B. Little. Cislunar periodic orbit constellation assessment for space domain awareness of l1 and l2 halo orbits. In <u>ASCEND 2021</u>.

[54] A. Wächter. <u>An Interior Point Algorithm for Large-Scale Nonlinear Optimization with Applications in Process Engineering</u>. PhD thesis, Carnegie Mellon University, Pittsburgh, PA, 2002.